Politecnico di Torino

Master's Degree in
Micro and Nanotechnologies for Integrated Systems

A.y. 2023-2024

Master's Degree Thesis

Electrodynamics of an High Luminosity LHC Superconducting Magnet

---

by Valentina Reynaud

Thesis Advisor
Prof. Dr. Claudio Ricciardi

Thesis Supervisor
Marvin Janitschke

October 23, 2024

Acknowledgments

I would like to start with a huge thank you to my amazing supervisor, Marvin Janitschke. I can't thank you enough for your trust, support, and guidance. You were always available for a chat or a question, and I'm incredibly grateful for the opportunity you gave me to work at CERN. It's been an exciting journey learning something new and pushing myself, and I appreciate all the time and energy you've invested in this thesis and in my work overall.

A big thanks also goes out to everyone in the TE-MPE-PE section at CERN for making the work environment so welcoming and friendly. I especially appreciate those who helped me get through the hottest weeks of summer with fans, offered me food or a kind word, and checked in on me during the last few weeks. Your support made all the difference.

Looking back on the past few months, I've loved every moment and am excited for what's ahead. I'm thankful for everyone I've met, whether recently or over the years. I appreciate the experiences we've shared and the adventures we've had, and I'm grateful for being part of your lives, even if just for a while.

A special shoutout goes to the Nanotech community. Nothing brings people closer than a master's degree where you're bounced around Europe like a flipper, relying only on your survival skills and sense of improvisation to get through. It's been a wild ride, and I couldn't be happier to have had you with me along the way. Expecially, a big thank you to my friend Marius, I enjoyed all the fun times we've had and I'm grateful you didn't manage to get us killed on that via ferrata, despite your best efforts.

Una parte del mio cuore appartiene alla mia famiglia acquisita: ognuna di voi è una persona speciale e unica, e sono infinitamente grata per la vostra presenza nella mia vita. Chiara, grazie per la tua dolcezza e le tue storie che ci regalano sorrisi. Cia, grazie per il tuo entusiasmo travolgente e i tuoi abbracci che sanno scaldare l'anima. Geppi, grazie per riempire ogni momento di risate con il tuo modo inimitabile di affrontare la vita. Vero, grazie per essere sempre la mia complice perfetta, la mia partner in crime in ogni avventura. Insieme, con le nostre risate, la nostra goffaggine e quel modo imprevedibile e spontaneo di affrontare ogni situazione, abbiamo reso ogni momento indimenticabile.

Grazie anche a tutte quelle che persone che, nonostante veda raramente e non senta tutti i giorni, sanno di casa e mi accolgono sempre a braccia aperte al mio ritorno. In particolare, grazie Gaia e Otta per essere al mio fianco da ormai tanti tanti anni e supportarmi sempre.

Infine, desidero ringraziare la mia famiglia. Grazie per essere stati una costante fonte di sostegno, per i valori che mi avete trasmesso, per avermi incoraggiata a perseguire i miei obiettivi e per avermi insegnato che il duro lavoro e il sacrificio vengono sempre ripagati. Ale, grazie per avermi mostrato come mettermi in gioco senza paura; Papà, grazie per avermi infuso la tenacia e il coraggio di lottare per i miei pensieri; Mamma, grazie per essere la mia roccia e sempre al mio fianco, ogni mio traguardo è anche il tuo.

Meyrin, October 23, 2024 Vi voglio bene, Valentina Reynaud

Abstract

Superconducting magnets are key components in particle accelerators, essential for the precise guidance and focusing of particle beams. However, these magnets are subjected to stresses, like radiation and mechanical disturbances, which can lead to faults such as short circuits in the coil windings. Identifying such faults in the magnets installed in the LHC is a major challenge. A valuable method to assess their electromagnetic properties and detecting potential problems is to analyse their complex impedance over a wide range of frequencies. This thesis contributes to the advancement of CERN's STEAM (Simulation of Transient Effects in Accelerator Magnets) framework by introducing a new tool specifically designed to simulate complex impedance in the frequency domain. While STEAM already supports the modeling of transient effects and magnet circuits, it has lacked a comprehensive solution for complex impedance simulations in the frequency domain. To address this gap, a new Python-based tool was developed, built on a physics-driven lumped element network model. This model integrates finite element modeling using COMSOL Multiphysics® with analytical techniques, taking into account key factors such as coupling losses and interactions between coil turns. This approach also facilitates the modeling of short circuits by incorporating resistances across the coil turns.

This thesis provides an overview of the development and functionality of this tool and presents its validation through impedance measurements of the Main Bending Recombination Dipole (MBRD), a magnet recently measured at CERN's SM18 facility. The validation process included simulations of both standard operating conditions and faulty scenarios with short circuits, demonstrating the tool's ability to capture the complex behavior of superconducting magnets. The results confirm the accuracy of the tool in predicting and analyzing magnet performance, including the effects of short circuits with varying resistance values and fault locations. In summary, this work improves the understanding of superconducting magnet impedance characteristics and introduces a reliable method for early detection of potential failures, thereby contributing to the ongoing safety and performance of the LHC's magnets.

Sommario

I magneti superconduttori sono componenti chiave degli acceleratori di particelle, essenziali per la guida e la focalizzazione precisa dei fasci di particelle. Tuttavia, questi magneti sono soggetti a sollecitazioni, come radiazioni e disturbi meccanici, che possono portare a guasti come cortocircuiti negli avvolgimenti delle bobine. L'identificazione di tali guasti nei magneti installati nell'LHC è una sfida importante. Un metodo valido per valutare le loro proprietà elettromagnetiche e individuare potenziali problemi è l'analisi della loro impedenza complessa su un'ampia gamma di frequenze.

Questa tesi contribuisce all'avanzamento del framework STEAM (Simulation of Transient Effects in Accelerator Magnets) del CERN introducendo un nuovo strumento specificamente progettato per simulare l'impedenza complessa nel dominio della frequenza. Sebbene STEAM supporti già la modellazione degli effetti transitori e dei circuiti dei magneti, mancava una soluzione completa per le simulazioni di impedenze complesse nel dominio della frequenza. Per colmare questa lacuna, è stato creato un nuovo strumento in Python che utilizza un modello circuitale basato su "lumped-element modeling" e su un approccio fisico. Questo modello integra la modellazione a elementi finiti di COMSOL Multiphysics® con tecniche analitiche, tenendo conto di fattori chiave come le perdite di potenza causate dalle correnti indotte negli elementi del magnete e le interazioni tra le spire. Inoltre, il modello permette di simulare i cortocircuiti introducendo resistenze tra le spire della bobina.

La tesi offre una panoramica dello sviluppo e delle funzionalità di questo strumento, e ne presenta la validazione tramite misure di impedenza del Main Bending Recombination Dipole (MBRD), un magnete recentemente testato presso la struttura SM18 del CERN. Il processo di validazione ha incluso simulazioni in condizioni operative standard e in scenari di guasto con cortocircuiti, dimostrando la capacità dello strumento di catturare il comportamento complesso dei magneti superconduttori. I risultati confermano l'accuratezza dello strumento nella previsione e analisi delle prestazioni del magnete, inclusi gli effetti dei cortocircuiti con diverse resistenze e posizioni di guasto.

In sintesi, questo lavoro migliora la comprensione delle caratteristiche di impedenza dei magneti superconduttori e propone un metodo affidabile per la rilevazione precoce di potenziali guasti, contribuendo così alla sicurezza e alle prestazioni dei magneti nell'LHC.

Résumé

Les aimants supraconducteurs sont des composants clés des accélérateurs de particules, essentiels pour le guidage et la focalisation précis des faisceaux de particules. Cependant, ces aimants sont soumis à des contraintes, telles que le rayonnement et les perturbations mécaniques, qui peuvent entraîner des défauts tels que des courts-circuits dans les enroulements des bobines. L'identification de ces défauts dans les aimants installés dans le LHC est un défi majeur. Une méthode précieuse pour évaluer leurs propriétés électromagnétiques et détecter les problèmes potentiels consiste à analyser leur impédance complexe sur une large gamme de fréquences.

Cette thèse contribue à l'avancement du cadre STEAM (Simulation des effets transitoires dans les aimants d'accélérateurs) du CERN en introduisant un nouvel outil spécialement conçu pour simuler l'impédance complexe dans le domaine des fréquences. Bien que STEAM prenne déjà en charge la modélisation des effets transitoires et des circuits d'aimants, il lui manquait une solution complète pour les simulations d'impédance complexe dans le domaine des fréquences. Pour combler cette lacune, un nouvel outil basé sur Python a été développé sur la base d'un modèle de réseau à éléments forfaitaires basé sur la physique. Ce modèle intègre la modélisation par éléments finis à l'aide de COMSOL Multiphysics® et des techniques analytiques, en tenant compte de facteurs clés tels que les pertes de couplage et les interactions entre les spires des bobines. Cette approche facilite également la modélisation des courts-circuits en incorporant les résistances entre les spires de la bobine.

Cette thèse donne un aperçu du développement et de la fonctionnalité de cet outil et présente sa validation par des mesures d'impédance du dipôle principal de recombinaison de flexion (MBRD), un aimant récemment mesuré à l'installation SM18 du CERN. Le processus de validation comprenait des simulations de conditions de fonctionnement standard et de scénarios défectueux avec des courts-circuits, démontrant la capacité de l'outil à saisir le comportement complexe des aimants supraconducteurs. Les résultats confirment la précision de l'outil dans la prédiction et l'analyse des performances de l'aimant, y compris les effets des courts-circuits avec des valeurs de résistance et des emplacements de défaut variables. En résumé, ce travail améliore la compréhension des caractéristiques d'impédance des aimants supraconducteurs et introduit une méthode fiable de détection précoce des défaillances potentielles, contribuant ainsi à la sécurité et aux performances des aimants du LHC.

Contents

Acknowledgments **I**

Abstract (English/Italiano/Français) **II**

List of Figures **VII**

List of Tables **X**

List of Acronyms **XI**

1 Introduction **1**
- 1.1 Context and Background . . . 1
- 1.2 Problem statement . . . 2
- 1.3 Project Overview . . . 3
- 1.4 Impact and Contributions to Nanotechnologies for ICTs . . . 4
- 1.5 Thesis outline . . . 5

2 Theoretical background **6**
- 2.1 Superconductivity . . . 6
- 2.2 Building blocks of Superconducting Magnets . . . 8
- 2.3 Coupling effects in superconducting magnets . . . 9
  - 2.3.1 Inter-Strand Coupling Losses . . . 10
  - 2.3.2 Inter-Filament Coupling Losses . . . 10
  - 2.3.3 Eddy currents in the copper sheath . . . 11
  - 2.3.4 Persistent currents . . . 12
- 2.4 The Main Bending Recombination Dipole . . . 13
- 2.5 Impedance Measurements of the MBRD . . . 16

3 Impedance Modeling and Automatic Model Generation **18**
- 3.1 Lumped elements modeling . . . 19
- 3.2 Model Overview . . . 20
  - 3.2.1 STEAM framework and Data Flow . . . 21
- 3.3 Network model . . . 22
  - 3.3.1 Mutual coupling between different effects . . . 23
  - 3.3.2 Equivalent lumped-element parameters . . . 24
- 3.4 FEM in COMSOL Multiphysics® . . . 25
  - 3.4.1 STEAM py-SIGMA tool . . . 25
- 3.5 MBRD Simulation workflow . . . 26
  - 3.5.1 Wedges . . . 28
  - 3.5.2 Cold Bore . . . 29
  - 3.5.3 Coil-Protection Sheets . . . 30

3.5.4 Aluminium Ring 30
3.6 Automated Model Generation 31
3.6.1 Tool Structure and Input Files 31
3.6.2 Library file generation 33

4 Validation of the Model with experimental Magnets Data **38**
4.1 Validation of the Simulated Impedance 38
4.2 Coupling Current Effects on Impedance 39
4.3 Mutual Coupling contribution 42
4.4 Parametric Sweep Study 44
4.4.1 RRR of the Wedges 45
4.4.2 Resistivity of the Aluminum Ring 45
4.4.3 Resistivity of the Coil Protection Sheets 47

5 Simulation of Failures and Analyses **49**
5.1 Analytical Impact of Short Circuit on the Network Model 49
5.1.1 Short circuits implementation in the TFM tool 52
5.2 Measurements Comparison 53
5.3 Analysis of the Short Circuits Impact on the Simulated Impedance 55

6 Conclusions and Future Work **57**
6.1 Summary of findings 57
6.2 Model limitations 58
6.3 Outlook 59

Bibliography **61**

List of Figures

2.1 When an electron moves through a crystal lattice, it attracts ions with its negative charge, causing a lattice deformation and emitting phonons. This generates a positively charged zone that attracts another electron, forming a Cooper pair [3]. 6

2.2 Critical surface of Nb-Ti, showing the J-B cross-section on a typical operational temperature of 1.9 K in grey [14]. 7

2.3 Comparison between the magnetization curve of type-I and type-II semiconductors [20]. 7

2.4 A Rutherford cable for the inner layer of the LHC dipoles, showing the Nb–Ti filaments in a few etched strands [23]. 8

2.5 MBRD magnet cross section showing different components [33] 14

2.6 Field map of the MBRD magnet simulated in COMSOL Multiphysics® [39] [40]. 15

2.7 Measurement system for the MBRD full magnet, which comprises different voltage taps (orange circles) for measuring the voltage across different turns. A short resistance is also included for the purpose of illustrating how two turns can be shorted. 17

3.1 Scheme of the electrical subsystem in a LEDET model [28]. 19

3.2 Measurement of a stand-alone dipole, the MBRD, at 1.9 K. 20

3.3 Block-scheme of the STEAM framework, including all the principal tools [50]. . 21

3.4 This diagram illustrates the data flow involved in creating an accurate impedance simulation using the TFM tool. 22

3.5 Lumped element network model representing two equivalent loops coupled to two turns of a magnet [10]. 23

3.6 Lumped element network model representing a persistent currents equivalent loop coupled to a magnet inductance [10]. 24

3.7 Block diagram showing the process of building a COMSOL Multiphysics® model using STEAM-pySIGMA. [39]. 25

3.8 Zoom of the the MBRD COMSOL Multiphysics® geometry built using the STEAM-pySIGMA tool [39]. The manually added Coil-Protection Sheets (blue), Cold-Bores (magenta), and Aluminum ring (gray) are highlighted. 26

3.9 Representation of the electrical circuit added in the MBRD COMSOL Multiphysics® models. 27

3.10 Power loss and induced current in the wedges for different RRR at 1.9 K 28

3.11 Power loss and induced current in the cold bores at 1.9 K 29

3.12 Power loss and induced current in the coil protection sheets at 1.9 K 30

3.13 Power loss and induced current in the aluminum ring at 1.9 K simulated for 20 different aluminum resistivity values between $6.83 * 10^{-09}$ Ω·m to $1 * 10^{-06}$ Ω·m 31

3.14 Diagram illustrating the various dataclasses included in TFM, grouped by purpose. 32
3.15 Example of an input YAML file for launching TFM analyses of a circuit with a MBRD magnet. 33
3.16 Example of the magnet circuit generated for the MBRD considering just one section per aperture. 35
3.17 Example of the magnet circuit generated for the MBRD by assigning all the turns of the first aperture to group 11 and by splitting the turns of the second aperture into four different groups. 35
3.18 Example of the ISCC coupling loop generated for the first aperture in a MBRD impedance simulation. 37

4.1 Simulation and measurement of the MBRD impedance modulus including all coupling losses for the single aperture and full and full magnet configurations, and their relative error. 39
4.2 Simulation and measurement of the MBRD impedance phase including all coupling losses for the single aperture and full and full magnet configurations, and their absolute error. 40
4.3 Simulation of the MBRD Impedance showcasing the contribution of the different coupling losses. Z_{all} [Ω] is the only simulated impedance that includes the mutual coupling between different effects. 41
4.4 Simulation of the Differential Inductance for the MBRD full magnet configuration. The curve marked as "All effects" is the only simulation that accounts for the mutual coupling between different effects 42
4.5 Simulation of the MBRD Power Losses for the MBRD full magnet simulation . . 43
4.6 MBRD full magnet simulation showing the impedance modulus of the magnet with different mutual coupling included. 45
4.7 MBRD full magnet simulation showing the different impedance for 190 value of RRR of the wedges, in the range 10-200. 46
4.8 MBRD full magnet simulation showing the different impedance for 400 values of the Aluminum ring resistivity, in the range between 10^{-6} Ω·m and 10^{-9} Ω·m 47
4.9 MBRD full magnet simulation showing the different impedance for 100 values of the coil protection sheets resistivity, in the range between 400 nΩ·m and 630 nΩ·m 48

5.1 Simplified schematic of n inductances in series of which one inductance L_S is shorted by a parallel resistance [59] 50
5.2 The field map shows the magnetic field configuration within the turns of an MBRD magnet coil, calculated using ROXIE [51], and the number of turns in the model. 51

5.3 Plot of the inductance matrix of the coil turns for one pole. The diagonal represents the self-inductance of the turns, while the off-diagonal represents the mutual inductance between the turns. The numbering of the turns commences with the index 0, corresponding to turn 1, and concludes with index 30, corresponding to turn 31 of the configuration in Figure 5.2 52
5.4 a) Impedance modulus for the MBRD magnet with a 1-aperture configuration. The black dotted curve represents the reference impedance without shorts, while the other curves show the impedance with a R_{Short}=0.01 Ω applied across different turns. b) Relative difference between the reference impedance and the impedance with short circuits. The color bar indicates the turn across which the short circuit was applied. 53
5.5 Relative difference in the impedance magnitude between measurements and simulations without and with a short circuit resistance across two specific turns of the magnet. The specified short resistances have been connected at warm across the voltage taps EE01-EE02 in Figure 2.7, corresponding to turns 30-31 in Figure 5.2 [64]. 54
5.6 Relative error between the impedance simulation with and without the connection of a short circuit resistance of 0.01 Ω across the individual turns of the magnet. The color bar represents the number of the short-circuited turn, following the configuration displayed in Figure 5.2 [64]. 55
5.7 Relative error between the impedance simulation with and without the connection of a short circuit resistance across the same turn. The simulations have been performed for several resitance values between R_{Short} = 1 nΩ and R_{Short} = 0.1 MΩ [64]. 56

List of Tables

2.1 Main parameters of the MBRD magnet [31] [32] [33]. 13
2.2 Main parameters of the MBRD magnet cable and strands used in the simulations [25] [35]. 14

3.1 Formulas for the calculation of the persistent currents and eddy currents coupling loops parameters [10]. 25
3.2 Time constant comparison between the TFM tool calculation and the COMSOL Multiphysics® simulations for each metallic effect [10]. 37

4.1 Mutual coupling between the magnet component loops, found in simulations of both the full magnet configuration and the single-aperture setup. 43

List of Acronyms

AlRing	Aluminum Ring
ATLAS	A Toroidal LHC ApparatuS
BSC	Bardeen-Cooper-Schrieffer
CB	Cold Bore
CERN	European Organization for Nuclear Research
CL	Conductor Losses
CMCS	Compact Muon Solenoid
CPS	Coil Protection Sheets
CSCL	Copper Sheath Coupling Losses
ELQA	ELectrical Quality Assurance
FEM	Finite Element Modeling
HL-LHC	High Luminosity LHC
IFCC	Inter Filament Coupling Currents
IFCL	Inter Filament Coupling Losses
INFN	National Institute for Nuclear Physics
ISCC	Inter Strand Coupling Currents
ISCL	Inter Strand Coupling Losses
LEDET	Lumped-Element Dynamic Electro-Thermal
LEM	Lumped Elements Models
LHC	Large Hadron Collider
MBRD	Main Bending Recombination Dipole
MDSS	Magnetic Drug Delivery System
MRI	Magnetic Resonance Imaging
nano-MRI	Nanoscale Magnetic Resonance Imaging
Nb-Ti	Niobium–titanium
PC	Persistent Currents
STEAM	Simulation of Transient Effects in Accelerator Magnets
TE-MPE-PE	Performance Assessment and Electrical Quality Assurance
TFM	Transfer Function Measurements
Roxie	Routine for the Optimization of magnet X-sections, Inverse field calculation and coil End design
YAML	Ain't Markup Language

Introduction

1.1 Context and Background

High-energy particle colliders, such as the Large Hadron Collider (LHC) at CERN, are crucial for experimental particle physics. In this accelerator, particles travel in opposite directions at almost the speed of light before they collide.
The LHC uses superconducting magnets to guide and focus particle beams along circular paths. Strong magnetic fields are required to maintain the circular trajectory and only cables constructed with superconducting materials can achieve this level of magnetic strength [1]. A large number of magnets are necessary to maintain the particle beam within the desired collider radius. The relationship between the beam energy E [J], the magnetic field B [T] of the dipoles in the arc, and the trajectory radius R [m] can be expressed as [2]:

$$E = 0.3 \times B \times R \quad [J] \tag{1.1}$$

It is therefore crucial to have magnets capable of producing a high magnetic field to minimize collider's radius while achieving the desired high energy [2].
When cooled to extremely low temperatures, superconducting materials exhibit zero electrical resistance and allow for high current densities while showing no power dissipation. Additionally, they exhibit the Meissner effect whereby the externally applied magnetic fields are expelled from the interior of the materials [3]. In order to maintain their superconductivity, the applied magnetic field, temperature, and current density must all be less than a related set of critical parameters [4]. Therefore, magnets in the LHC operate at cryogenic temperatures. The reliable operation of the superconducting magnets is crucial for accurately replicating physical phenomena in the LHC. Superconductors can sometimes experience a phenomenon called quench, a transition to the normal state of the superconductor in a part of the material, which forces the electromagnetic energy passing through the conductor to be converted predominantly into heat. If this transition is not handled properly, it can result in overheating, causing insulation degradation, conductor meltdown, short circuits due to the high voltage and structural failures due to thermal expansion stresses, leading to the destruction of the magnet at high currents [5]. There are several reasons for a magnet to fail [6]:

Mechanical forces: The most probable cause of failure is mechanical stress, which could potentially arise due to the high thermal gradients to which the cables of the superconductor are subjected during the operational process. Such conditions may result in the formation of microcracks and microfractures, which could lead to the movement of cables and subsequent failure of the superconducting magnets' behavior [7].

High voltages: The application of high voltages and fast ramping can result in the generation of significant electromagnetic forces. These may lead to the failure of insulation materials and the generation of short circuits.

Human operation: The operation of the LHC requires human intervention. However, if for example the magnet components are mishandled or the quench management procedures are not followed correctly, this can lead to failures in the performance of the magnet.

Deficient cooling The malfunctioning of the cryogenic system can lead to a localized increase in temperature beyond the level required to maintain the conductors in a superconducting state.

To ensure that the magnets operate safely in the collider, it is therefore crucial to continuously monitor and improve their performance, identifying and predicting the phenomena that could lead to a failure [8]. A magnet that requires replacement due to a failure typically results in repair times exceeding three months, along with significant costs.

1.2 Problem statement

Since the superconducting coils of the magnets cannot be accessed from the outside while installed in the LHC, it is particularly challenging to monitor and assess for failures and their precursors. Cooled helium flows in a closed circuit to maintain the system at cryogenic temperature and the magnets in a superconducting state [9]. In addition, the magnet has zero resistance in its superconducting state, which makes it difficult to identify early signs of resistance increase that indicates the beginning of a fault or quench. In the event of an impending failure, the process can occur rapidly, making it challenging to identify and prevent.

Particle accelerators' superconducting magnets are also exposed to a variety of stresses, radiation, and disturbances. These may cause non-conformities like inter-turn shorts, whose precursors can be extremely difficult to find once the magnets are installed in the LHC [10].

A promising way to analyze and determine the electro-magnetic properties of the magnets and identify any potential issues is to examine their impedance across a wide frequency range. Because superconducting magnets have parasitic effects and capacitance in their circuit, their electrical characteristics are not purely inductive. By looking at their impedance, it is possible to non-invasively detect changes in their superconductive state and identify losses and parasitic effects that may affect their ideal behavior [8].

Time Domain Reflectometry (TDR) is a technique that can be used to locate faults in electrical circuits, by detecting changes in impedance. It relies on the property of a signal that travels along a transmission line to be reflected when the line impedance changes. By sending a short, high-frequency electrical pulse through the system and by measuring the time gap between the incoming and reflected waves and the speed of propagation, it is possible to locate the fault. However, also this approach has limitations, including the need for TDR equipment, limited accuracy related to pulse width, the difficulty in recognizing the different types of faults and the lack of references to this technique for superconducting magnets [11].

Other methods have been proposed in the literature to address the problem of fault detection. One method is based on analysing the magnetic field generated in an aperture of the magnet by an injected high-voltage pulse: the presence of a defect affects the current distribution inside the coils, leading to a distortion of the expected magnetic field. By measuring the pseudo period, it is possible to detect internal coil shorts and ground insulation faults through the observation of any resulting field distortions [12]. However, this approach has limitations. To map the magnetic field, measurement probes need to be inserted into the bore of the magnets, which are inaccessible once installed in the LHC. Furthermore, it does not account for other disturbances, such as AC losses.

Other approaches use machine learning algorithms to detect outliers in the data. However, these methods lack a physics-based foundation and do not provide a comprehensive model to understand the electromagnetic behaviour of superconducting magnets. This makes it difficult to simulate and investigate potential failure scenarios and ensure repeatability [10].

1.3 Project Overview

At CERN, the Performance Assessment and Electrical Quality Assurance (TE-MPE-PE) section developed the STEAM (Simulation of Transient Effects in Accelerator Magnets) framework. This hierarchical co-simulation framework allows the simulation of transients effects in superconducting accelerator magnet circuits [13]. It contains a number of in-house tools that cover the physics and geometries of every magnet circuit, including details about cables, wires, and filaments. These tools allow the simulation of failures or specific events in the magnets, as well as transient simulations in the time and frequency domains.

However, an accurate and reliable tool designed specifically for simulating the complex impedance of magnets in the frequency domain was still missing. Such a tool should also support the simulation of non-conformities by incorporating short circuits into the model. Additionally, it must account for various effects that cause superconducting magnets to deviate from their ideal behavior. These effects include coupling losses, which occur in superconducting magnet elements due to the cables' sensitivity to changes in the magnetic field. This sensitivity induces currents that produce opposing fields, thereby affecting the impedance curve of the magnets [14].

The aim of this Master's thesis is to model, simulate and validate the behavior of superconducting magnets by studying the variation of their transfer function in the frequency domain. In particular, this report will present the results for one of the magnets that will be used in the High Luminosity Upgrade of the LHC: the Main Bending Recombination Dipole (MBRD). This magnet was recently measured as a prototype in the SM18 test magnet facility at CERN, meaning that a large amount of impedance measurements data has been collected. This includes different scenarios such as with and without shorts, allowing accurate and thorough validation of the simulations.

To accomplish this task, the STEAM framework needs to be extended by integrating a validated, physics-based approach to accurately analyse the electrical characteristics of magnets in both the time and frequency domains. This will involve modelling and simulating the magnet impedance under different conditions for all magnets already present in the STEAM framework.

It will employ a combined method that utilizes finite element modeling (FEM) with COMSOL Multiphysics® software and analytical modelling to incorporate various non-linear coupling

effects. The model will account for coupling losses to ensure accurate simulation results and to potentially identify any anomalies in magnet behaviour.
Recently, an equivalent lumped element network model for impedance simulations has been developed. It is a computationally inexpensive method that accurately reproduces the electrodynamic behaviour in both the time and frequency domains and will serve as the basis for this work [10]. Once validated, the model will be extended to other magnets.

1.4 Impact and Contributions to Nanotechnologies for ICTs

Superconductivity has applications in many areas of nanotechnology due to its ability to conduct electricity without dissipation. This is particularly important for developing energy-saving technologies, such as nanotechnology. Some examples of technologies using superconducting properties or superconducting magnets are listed below:

Medical applications Superconductivity is widely used in medical applications.
One example is the Nanoscale Magnetic Resonance Imaging (nano-MRI). MRI provides high-resolution tissue imaging by utilizing the electromagnetic response of tissue to a combination of magnetic and radio energy.
Nano-MRI aims at increasing the resolution of MRI from tens to micrometers down to the nano-scale. To achieve good imaging quality, the magnets used in the MRI systems need to generate a high magnetic field. This has led to the application of superconducting magnets in this field, promising to enable the construction of more compact and lower weight units capable of delivering a much stronger and homogeneous magnetic field that allows to achieve high resolution and contrast and minimizes image defects [15].
Another example of medical device that makes use of superconducting magnets is a Magnetic Drug Delivery System (MDSS).
The MDSS distributes high concentration medications to a targeted organ using a superconducting magnetic field, preventing them from spreading to undesirable tissues [16].
Quantum applications The Josephson junction is an example of a device used in quantum applications that makes use of superconductivity. It consists of a thin layer separating a superconductor from a metal or another superconductor. This type of junction, if the interlayer is thin enough, creates a tunnel current by using the superconducting property of the electrons to tunnel from one conductor to the other as long as there are full states in the first conductor and empty states in the second [17]. Josephson junctions are the fundamnetal building blocks used in quantum computing applications to construct qubits, the basic units of information in quantum computers [18].
Nano-sensors Nanowires are used to build sensors with enhanced sensitivity due to the much larger area to volume ratio [19]. They are nanostructures that exhibit quantum mechanical effects. However, scaling electronics down to the nanoscale can be challenging, and superconducting nanowires hold great promise in the field of nanosensors due to their exceptional conductive properties.

Specifically, the tool developed for this Master's thesis research will enable accurate impedance simulations to be performed on superconducting magnets. This will make it

possible to monitor the behaviour of the magnets and to anticipate and prevent any failure that may result from improper behavior, making it possible to understand the behaviour of the superconductors and superconducting systems over a wide range of frequencies.
The result is a validated tool that allows a quick and accurate diagnosis to potentially find measurement techniques for detecting failures.

1.5 Thesis outline

This thesis is organized to detail every stage of the master's thesis project, from the theoretical background to the model-building phases and the methods used to complete them, and finally to the results. An outline of this thesis's structure is provided below:

Chapter 2: Theoretical background This chapter provides a deeper understanding of superconductivity and superconducting magnets in LHC, offering all the necessary information to provide a general comprehension of the background and goals of the research. It also gives a detailed description of the MBRD magnet.

Chapter 3: Impedance Modelling and Automated Model Generation This chapter presents the lumped-element circuit model, establishing the theoretical groundwork for understanding the forthcoming practical work. It also outlines the simulation performed in Comsol for the MBRD and details the methodology for developing the tool that interfaces between Python and COMSOL Multiphysics®, enabling precise transfer function simulations within the STEAM framework.

Chapter 4: Validation of the Model with experimental Magnets Data By comparing the simulations with the measurements, this chapter displays the outcome of the tool whose development was presented in Chapter 3.

Chapter 5: Simulation of Failure and Analyses This chapter details the application of the tool for the detection of short circuits between turns of the magnet cable. It examines the impact of varying short-circuit resistance values on the deviation of the magnet's impedance curve. It also investigates the distinct effects of identical short-circuit resistance values when applied to different turns of the magnet.

Chapter 6: Conclusion and Future Work This chapter finally summarizes the findings and outlines the actions that will be taken to apply the model to all magnets whose data is included in the STEAM framework.

Theoretical background

2.1 Superconductivity

In any material, lattice vibrations dominate at high temperatures, reducing the free path for electrons due to electron-phonon collisions. However, as the temperature decreases, these vibrations are almost completely eliminated, resulting in a drastic decrease in the materials' resistivity [20]. In certain materials, this decrease in resistivity suddenly drops to zero below a certain temperature, known as the critical temperature. The Bardeen-Cooper-Schrieffer (BCS) theory explains this phenomenon through the formation of the so-called Cooper pair, an electron-electron interaction made possible by the accumulation of positive charge due to lattice distortion, overcoming the Coulomb repulsion between charges of the same sign. The paired particles act as bosons, condensing into a quantum state and traveling through the lattice without resistance, as can be seen in Figure 2.1 [20].

Superconducting magnets use conductors made from superconducting materials, which have no electrical resistance, enabling a higher current flow than normal wires. This results in the generation of a magnet with a strong field, since the strength of a magnetic field is proportional to the magnitude of the current flowing through it [21].

These materials maintain their superconducting state as long as they operate below the so-called "critical surface," spanned by the parameters critical field $\mathrm{B_c}$ [T], critical temperature $\mathrm{T_c}$ [K], and critical current density $\mathrm{J_c}$ [A/m]. If the magnetic field is increased while the current and temperature remain constant, the conductor becomes resistive at the critical field B_c. The same applies to temperature and current when $\mathrm{T_c}$ or $\mathrm{J_c}$ is reached. This creates a unique critical surface for each superconductor, outside of which a transition to the normal state, called quench, occurs.

The critical surface for a commonly used superconductor, Niobium–titanium (Nb-Ti), is shown in Figure 2.2 as example.

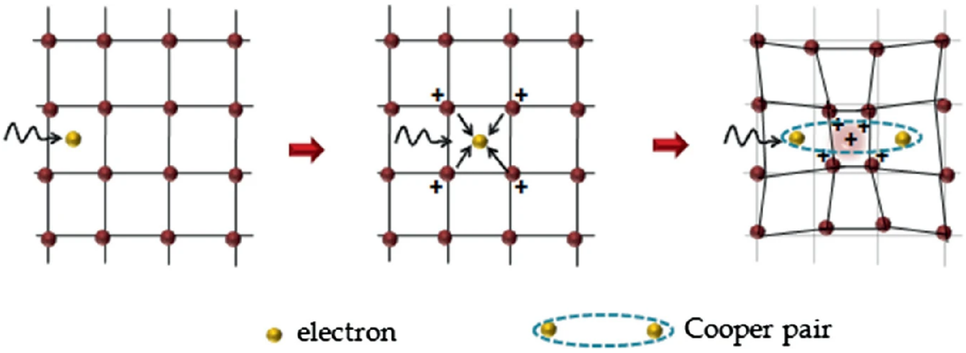

Figure 2.1: When an electron moves through a crystal lattice, it attracts ions with its negative charge, causing a lattice deformation and emitting phonons. This generates a positively charged zone that attracts another electron, forming a Cooper pair [3].

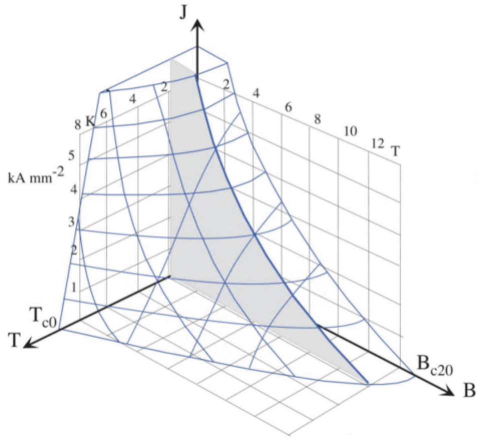

Figure 2.2: Critical surface of Nb-Ti, showing the J-B cross-section on a typical operational temperature of 1.9 K in grey [14].

Based on their reaction on an externally applied magnetic field, the superconductor are divided into two types, as can be seen in Figure 2.3 . Type-II superconductors are capable of reaching much higher magnetic fields than type-I superconductors, making them ideal for applications at the LHC. Typically composed of metal alloys or ceramics, they exhibit an intermediate phase during their transition from the superconducting to the normal state. In this in-between transition, their properties are mixed since they contain impurities that create zones which remain normally conducting. When the lower critical field B_{c1} [T] is exceeded, magnetic flux begins to penetrate the material through these zones, which act as pinning centres, allowing them to maintain their superconducting state and therefore withstand a higher magnetic field. Upon reaching the upper critical field B_{c2} [T], type-II superconductors fully transition to a normal state [14].

Any design involving superconducting materials take into account the stored energy. When a quench occurs, the high current in the suddenly resistive region causes rapid heating, leading to dissipation of energy in the form of heat. This quenching phenomenon will spread until all the material becomes non-superconducting, unless a sufficiently low temperature is applied to restore its superconducting properties [22].

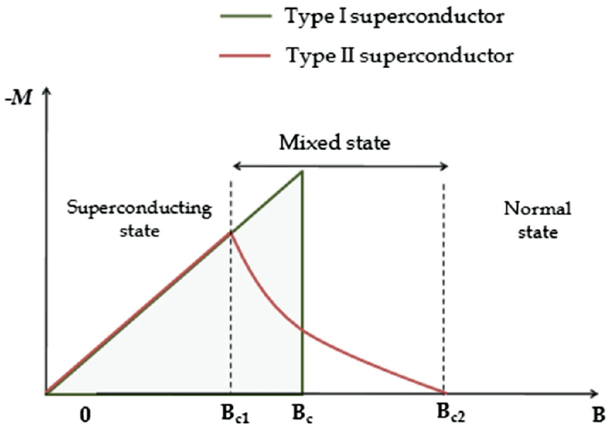

Figure 2.3: Comparison between the magnetization curve of type-I and type-II semiconductors [20].

2.2 Building blocks of Superconducting Magnets

Magnets should be capable of generating a high magnetic field with excellent field quality and thermal stability. Additionally, they must ensure high alignment and mechanical stability to maximize luminosity, thereby providing optimal conditions for particle collisions [2].
The main component of a superconducting cable is a strand, consisting of thousands of filaments of superconducting material, made of a diameter of a few micrometers.
In most of the currently installed magnets at CERN, the material used is Nb-Ti, which has a critical temperature of approximately 9.2 K and allows building magnets capable of generating a magnetic field of 8.3 T in the main dipole. The filaments are then embedded in a copper matrix, to stabilize the conductor. The electrical resistance of copper is lower than that of Nb-Ti in normal state; this means that if a quench occurs, the current will preferably flow through the copper, reducing the Joule heating in the coils and therefore providing some protection [11]. In the case of a local temperature increase, the current density could exceed the critical value. Any excess would be transferred to the copper, thereby preventing a sudden transition to the resistive state by sharing the current between the superconductor and the copper matrix. This phenomenon is referred to as current sharing.
When this current sharing phenomenon occurs, the temperature of the copper also increases due to the current flow. To prevent the quench from happening, adequate cooling is necessary. The residual resistivity ratio (RRR) reflects the characteristics of the copper matrix used and can be expressed as:

$$RRR = \frac{\rho_{293\,\mathrm{K}}}{\rho_{4\,\mathrm{K}}} \quad [-] \tag{2.1}$$

where $\rho_{293\,\mathrm{K}}$ $[\Omega \cdot \mathrm{m}]$ is the resistance at ambient temperature while $\rho_{4\,\mathrm{K}}$ $[\Omega \cdot \mathrm{m}]$ at cryogenic temperature. The RRR range for Nb-Ti cables is 50–300; the greater the RRR, the lower the impurities in the copper.

The filaments are twisted by a certain length, called the filament twist pitch $\mathrm{L_f}$ [m], in order to reduce inter-filament coupling losses. In fact, when there is a change in the external magnetic field, some currents are induced in the superconducting part of the cable filaments,

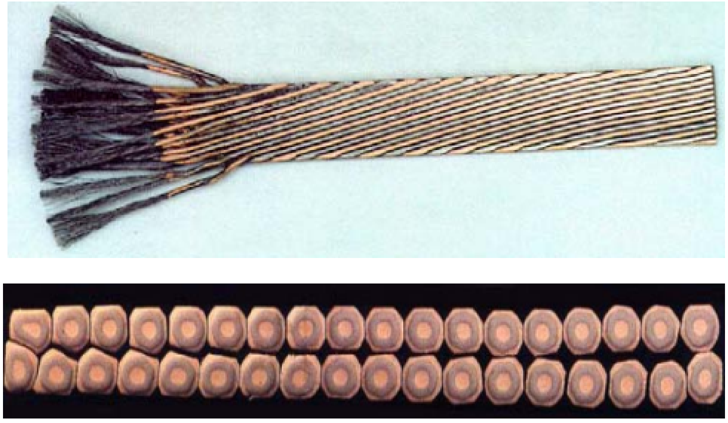

Figure 2.4: A Rutherford cable for the inner layer of the LHC dipoles, showing the Nb–Ti filaments in a few etched strands [23].

creating a field opposite to the external one. These currents cross through the copper matrix of the conductor and generate losses that affect the impedance of the magnet.

Also the strands are then twisted together to form the so-called Rutherford cable, which is a two-layered structure with the strands stacked one on top of the other, thereby achieving a good mechanical stability, a thin structure and reduced losses due to transposition of the strands [24]. As illustrated in Figure 2.4, the strands in a Rutherford cable are twisted by a specific pitch and with a precise alignment, which serves to reduce voids in the cable and to minimise the coupling between different strands. The twist length of the strands is defined by the parameter $\mathrm{L_s}$ [m].

The Rutherford cable is then wound into coils, which are a series of wire loops wound in a specific geometry that allow a magnetic field to be created when an electric current flows through them. During the winding process, copper wedges are placed between the blocks of the cables to fine-tune the magnetic field produced by the coils. They also serve as spacers in order to improve current distribution [24].

To contain mechanical forces, it is crucial to minimise the friction and movement of the coils, which is the primary cause of an unexpected quench. The collars made of stainless steel, which prevent any movement and balance out the pressures brought on by the electromagnetic force during operation, hold the coils in place [11].

The collars are finally inserted into an iron yoke whose role is to achieve the desired quality factor, which is a measure of the strength and quality of the magnetic field. The structure that results is then surrounded by a shrinking cylinder made of stainless steel which provides rigidity and support to the entire magnet [25].

2.3 Coupling effects in superconducting magnets

A time-varying current $\dot{\mathrm{I}}_{\mathrm{Mag}}$ [A/s] flows through the coils of the conductor, creating a time-varying magnetic field $\dot{\mathrm{B}}_{\mathrm{a}}$ [T/s] inside the magnet. According to Faraday's law, a voltage is induced in a conductor loop when subjected to a time-varying flux. In fact, this change in the external magnetic field generates a specific current density $\mathrm{J_{ec}}$ [A/m^2] which results in an equivalent total induced current $\mathrm{I_{ec}}$ [A]. As a result, time-varying currents are generated in all conductive elements of the magnet, such as the iron yoke, aluminum ring, coils, beam shields, etc. These currents generate an opposing magnetic field $\dot{\mathrm{B}}_{\mathrm{a}}$ [T/m] to contrast this field change, causing ohmic losses and field distortions [26].

These currents are called eddy currents and decay with a characteristic time constant τ_{ec} [s], which can be defined by the following relationship, valid only in the volume in which the current flows [10]:

$$\dot{B}_{\mathrm{ec}} = -\tau_{\mathrm{ec}} \dot{B}_{\mathrm{tot}} \quad [\mathrm{T}] \tag{2.2}$$

where $\dot{\mathrm{B}}_{\mathrm{tot}}$ [T/m] is the total magnetic field given by the sum of the internal and external magnetic fields.

Eddy currents flow in a closed path through resistive elements and therefore cause losses. These currents are distinguished by the type of material, the area they cross through, the length of the loop in which they flow, and their characteristic time constant [27].

2.3.1 Inter-Strand Coupling Losses

The inter-strand coupling currents (ISCC) are eddy currents produced in cables with uninsulated strands, both at room temperature and at low temperatures. They flow along the length of a strand and pass through the cross-contact resistances between different strands, forming a loop and causing ohmic losses, called inter-strand coupling losses (ISCL).

Their magnitude depends on the contact resistance, which in turn depends on a variety of factors including the matrix material, the size of the contact surface, the applied pressure, and the degree of strand oxidation [27]. Their magnitude exponentially decays with a specific time constant. The inter-strand power loss, induced current, and time constant can be calculated using the analytical formulas, depending on the geometry of the cable and the variation of the magnetic field perpendicular to its broad face $\frac{\mathrm{dB}_\perp}{\mathrm{dT}}$ [T/s].

One geometrical parameter used in this calculation is β_{ISCL}, which is the contact length of the cross-contact resistance between different strands [28]:

$$\beta_{\text{ISCL}} = \frac{1}{120}\frac{L_{\text{P}}}{R_{\text{c}}} n_{\text{s}}(n_{\text{S}}-1)\frac{w_{\text{Bare}}}{h_{\text{Bare}}} \quad \left[\frac{m}{\Omega}\right] \tag{2.3}$$

where $\mathrm{L_P}$ [m] is the cable-twist pitch, $\mathrm{R_c}$ [Ω] is the cross-contact resistance between different strands, n_S [-] is the number of strands in the cable and $\mathrm{w_{Bare}}$ [m] and $\mathrm{h_{Bare}}$ [m] are the width and the height of the cable, respectively.

By using Equation 2.3 is possible to easily find the power loss, induced current and time constant as [10] [28] [27]:

$$P_{\text{ISCL}} = l_{\text{mag}}\beta_{\text{ISCL}} w_{\text{Bare}} h_{\text{Bare}} \left(\frac{dB_\perp}{dt}\right)^2 \quad [W] \tag{2.4}$$

$$I_{\text{ISCL}} = \beta_{\text{ISCL}} h_{\text{Bare}} \frac{dB_\perp}{dt} \quad [A] \tag{2.5}$$

$$\tau_{\text{ISCL}} = \mu_0 \beta_{\text{ISCL}} \quad [s] \tag{2.6}$$

where $\mathrm{l_{mag}}$ [m] is the length of the cable and $\mu_0 = 4\pi \times 10^{-7}\,\mathrm{T\cdot m\cdot A^{-1}}$ is the vacuum magnetic permeability. The value of the inter-strand time constant ranges between 0.1 s to 10 s [27].

2.3.2 Inter-Filament Coupling Losses

The inter-filament coupling currents (IFCC) are specific types of eddy currents that flow within the strands along the filaments, ultimately forming a loop by traversing the copper matrix after half a filament twist pitch. Since they cross a resistive part of the cable, they result in ohmic losses called inter-filament coupling losses (IFCL) [10].

The contact resistance length parameter can be defined as [10] [28] [27]:

$$\beta_{\text{IFCL}} = \left(\frac{L_{\text{f}}}{2\pi}\right)^2 \frac{1}{\rho_{\text{eff}}} \quad \left[\frac{m}{\Omega}\right] \tag{2.7}$$

where L_{f} is the filament strand pitch and ρ_{eff} [$\Omega\cdot$m] is the effective resistivity. The ρ_{eff} is a modified version of the strands' copper resistivity ρ_{Cu} [$\Omega\cdot$m], adjusted to account for the fraction of superconducting material in the filaments f_{SC} [-] and is defined as [11]:

$$\rho_{\text{eff}} = \rho_{\text{Cu}} \frac{1 - f_{\text{SC}}}{1 + f_{\text{SC}}} \quad [\Omega \cdot \text{m}] \tag{2.8}$$

The inter-filament power loss and induced current depend also on the magnetic field change $\frac{\text{dB}}{\text{dt}}$ [T/m] and the strand diameter d_s [m]. The IFCC magnitude decays exponentially with a characteristic time constant whose value ranges between 0.01 s to 0.1 s [27]. These parameters can be found using Equation 2.7 [10] [28] [27] as:

$$\begin{aligned} P_{\text{IFCL}} &= \frac{\pi}{4} d_{\text{s}}^2 l_{mag} \beta_{\text{IFCL}} \left(\frac{dB}{dt} \right)^2 \quad [\text{W}] && (2.9) \\ I_{\text{ISCL}} &= \beta_{\text{IFCL}} d_{\text{s}} \frac{dB}{dt} \quad [\text{A}] && (2.10) \\ \tau_{\text{IFCL}} &= \frac{\mu_0}{2} \beta_{\text{IFCL}} \quad [\text{s}] && (2.11) \end{aligned}$$

2.3.3 Eddy currents in the copper sheath

The presence of copper in the strands gives rise to the induction of eddy currents, which flow through the resistive material. This results in losses within the copper sheath that surrounds the filaments embedded in the copper matrix. This phenomenon is known as copper sheath coupling losses (CSCL). These losses can be calculated differently based on two different frequency regimes, which can be defined by the skin depth δ [m], the frequency-dependent penetration depth of an electromagnetic field into the conductor [29]. This parameter can be calculated as [10]:

$$\delta = \sqrt{\frac{2\rho_{\text{CMCL}}}{\omega \mu_0}} \quad [m] \tag{2.12}$$

where the angular frequency is defined as $\omega = 2\pi f \left[\frac{1}{s}\right]$.

The power loss and induced current in the copper matrix can therefore be calculated differently for the low-frequency and high-frequency regimes. At low frequencies, the effect of the eddy currents is very low and the thickness of the copper sheath is smaller than the skin depth [10]:

$$\delta \geq \left(1 - \frac{1}{\epsilon}\right)(r_{\text{s,o}} - r_{\text{s,i}}) \tag{2.13}$$

with $r_{s,o}$ [m] and $r_{s,i}$ [m] being the outer and inner radius of the strands, respectively. The inner radius corresponds to the radius of the filamentary region.

At high frequencies instead, the skin depth is less than the conductor thickness.

The induced current and power loss can be calculated analytically in both regimes, also depending on the outer diameter of the copper matrix of the strand, the effective copper resistivity and the magnetic field variation.

At low frequencies, the magnetic field change $\frac{\text{dB}}{\text{dt}}$ [T/m] is proportional to an additional term, which is the field attenuation factor. This is due to the fact that at low frequencies the developed eddy current cannot significantly oppose the field change, as a result of the

copper resistivity. In contrast, at high frequencies, the eddy currents in the outer copper sheath progressively attenuate the magnetic field, thereby reducing its penetration in the inner strand radius. As a result, the magnetic field variation at high frequencies $\frac{\mathrm{dB}^*}{\mathrm{dt}}$ [T/m] is independent of the attenuation factor [10].
The power loss and induced current in the copper sheath, can be found as [10][28] [27]:

$$P_{\mathrm{CSCL}} = \begin{cases} d_{\mathrm{s,o}}^4 \dfrac{\pi}{4\rho_{\mathrm{Cu}}} \left(\dfrac{dB}{dt}\right)^2, & \text{if } \delta \geq \left(1 - \dfrac{1}{\epsilon}\right)(r_{\mathrm{s,o}} - r_{\mathrm{s,i}}) \\ \\ \delta^3 \dfrac{\pi d_{\mathrm{s,o}}}{\rho_{\mathrm{Cu}}} \left(\dfrac{dB^*}{dt}\right)^2, & \text{if } \delta < \left(1 - \dfrac{1}{\epsilon}\right)(r_{\mathrm{s,o}} - r_{\mathrm{s,i}}) \end{cases} \quad [\mathrm{W}] \tag{2.14}$$

$$I_{\mathrm{CSCL}} = \begin{cases} \dfrac{d_{\mathrm{s,o}}^3}{3\rho_{\mathrm{Cu}}} \left(\dfrac{dB}{dt}\right), & \text{if } \delta \geq \left(1 - \dfrac{1}{\epsilon}\right)(r_{\mathrm{s,o}} - r_{\mathrm{s,i}}) \\ \\ \dfrac{\delta d_{\mathrm{s,o}}^2}{2\rho_{\mathrm{Cu}}} \left[1 - \exp\left(-\dfrac{d_{\mathrm{s,o}}}{\delta}\right)\right] \dfrac{dB}{dt}, & \text{if } \delta < \left(1 - \dfrac{1}{\epsilon}\right)(r_{\mathrm{s,o}} - r_{\mathrm{s,i}}) \end{cases} \quad [\mathrm{A}] \tag{2.15}$$

The time constant usually ranges between 0.1 ms and 1 ms [10] and can be calculated as in Equation 2.16, taking into account the copper matrix resistivity and its outer radius [10] [28] [27]:

$$\tau_{\mathrm{CMC}L} = \frac{\mu_0}{8} \frac{r_{\mathrm{s,o}}^2}{\rho_{\mathrm{Cu}}} \quad [\mathrm{s}] \tag{2.16}$$

2.3.4 Persistent currents

When an external magnetic field is applied to the superconductors, the Meissner effect causes a current to flow instantaneously, creating a magnetic field that opposes the external field. Even if the external magnetic field is removed, this current will continue to flow in an infinite loop as there is no resistance, resulting in currents called persistent currents (PC). These currents flow in the superconducting filaments in the wires, which have no resistance and don't have a time constant since they develop instantaneously. The magnitude of the PC depends on the geometry and size of the filaments, the applied field and its hysteresis, and the critical current of the superconducting material [30]. Their induced current and power loss can be calculated as [10] [28] [27]:

$$I_{\mathrm{ec,PC}} = M(T, B, M_{t-1}) * d_{\mathrm{s}} \quad [A] \tag{2.17}$$

where $M(T,B,M_{t-1})$ $\left[\frac{A}{m}\right]$ is the average homogenized magnetization in the volume of a strand. These currents can still affect the magnets impedance beacuse of the generation of losses when they encounter resistive defects in the superconductor [10] [28] [27]:

$$P_{\mathrm{loss}} = \int_V \mathbf{M} \frac{d\mathbf{B}}{dt} dV = \mu_0 \int_V \mathbf{M} \left(\frac{d\mathbf{H}}{dt} + \frac{d\mathbf{M}}{dt}\right) dV \quad [W] \tag{2.18}$$

where **H** [A/m] is the magnetic field strength of the superconductor, **M** [A/m] is the magnetization and V [m^3] is the volume of the superconducting region in the cables.

2.4 The Main Bending Recombination Dipole

The MBRD, also known as D2, is a magnet developed by the Genova Laboratory of the National Institute for Nuclear Physics (INFN) in collaboration with CERN. It will be a part of the High-Luminosity upgrade of the LHC and is designed to bring beams into the same path before and after the interaction point of the CMS and ATLAS experiments [31].
The High-Luminosity LHC (HL-LHC) is a project initiated to enhance the collider's performance. It aims to boost the potential for new discoveries by significantly increasing the amount of collisions through an upgrade of the luminosity of the collider, which is a measure of the number of potential collisions over a given period of time. One of the courses of action to achieve this result consists of installing magnets capable of generating a greater magnetic field in the proximity of the particle interaction area [34], including the MBRD.
The MBRD is a dipole magnet with a length of 7.78 m and a nominal inductance of about 30 mH. It has two asymmetrical apertures with same polarity, each with a diameter of 105 mm and a beam separation of 188 mm. The magnet generates in both aperture a magnetic peak field of 4.5 T. It is a cosine-theta dipole, meaning that the current used to generate the magnetic field follows a cosine function and varies with the θ angle. It operates with a nominal current of 12330 A, which corresponds to the current in the standard 14 TeV LHC configuration. However, 13357 A is the ultimate current that ensures operation at 15 TeV.
In Table 2.1 the main parameters for the MBRD dipole are shown [32].
The cable used is a Nb-Ti superconducting Rutherford cable and is identical to the one used for the outer layer of the LHC main dipole. The main parameters for the strands and the cable are listed in Table 2.2.

Table 2.1: Main parameters of the MBRD magnet [31] [32] [33].

Characteristic	**Value**
Bore magnetic field	4.50 T
Peak field in the conductors	5.26 T
Magnet length	7.78 m
Operating temperature	1.9 K
Total number of turns	124
Aperture diameter	105 mm
Beam separation	188 mm
Capacitance to ground	250 nF
Nominal inductance at nominal current	30.42 mH
Nominal inductance at low current	37.2 mH
Nominal current	12.34 kA
Ultimate current	13.26 kA
Stored energy	2.28 MJ
Maximum current density	443 A/mm²

Table 2.2: Main parameters of the MBRD magnet cable and strands used in the simulations [25] [35].

Characteristic	Value
Number of strands per turn	36
Total number of strands	8928
Bare cable width	15.1 mm
Bare cable height	1.476 mm
RRR	200
Cross-contact resistance	50 μmΩ
Ratio between Cu and not Cu	1.95
Strands outer diameter	0.825 mm
Strands core diameter	0.33 mm
Diameter of the filamentary matrix	0.66 mm
Filament twist pitch	0.015 m
Filament diameter	6 μm

In order to support the luminosity upgrade, the MBRD has been developed with larger apertures compared to the corresponding magnets in the LHC, making it suitable to increase the nominal field to 4.5 T [36]. To achieve the desired result, some unconventional design choices have been made in order to circumvent the potential issues that could arise due to the increased magnetic field. As can be seen in Figure 2.5 the magnet is made of [37]:

The two specular apertures Composed of asymmetric coils divided in five blocks and creating a total of 31 turns.

The collars Serve to contain the coils and to reduce the stress applied on the contained structure. Only one collar type was constructed, so the poles are separated pieces.

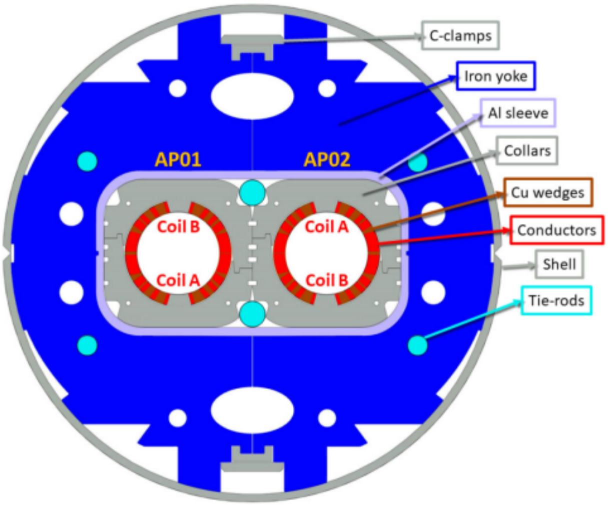

Figure 2.5: MBRD magnet cross section showing different components [33]

The aluminum-alloy sleeve Made of laminated aluminum, the aluminum ring has the role of managing the repulsive strength between the two apertures due to the Lorentz force, holding together the internal structure of the magnet [38].

The coil protection sheets Made of stainless steel, they are placed between the outer insulation layer of the coils and the collars to prevent damage caused by contact between the two surfaces. They also help to reduce conductor failures [25].

The six stainless steel tie-rods Passing through the iron yoke holes and in between the collared collars, are used to control the longitudinal stress.

The iron yoke Composed of two halves hold together through steel clamps.

The cold bore Made of stainless-steel, the cold-bore has the function of separating the coils from the internal vacuum region.

The wedges Made of copper, they serve as separation between the different blocks of coils in order to reach the ideal field quality and to improve current distribution.

The magnetic cross-talk between the apertures would have been a significant concern in the case of a symmetric coil design, as the magnetic field would have been subject to summation. This is why the MBRD has been designed with asymmetrical coils and no iron between the apertures, reducing the saturation effects on the field quality.
The sleeve material is an aluminium alloy of the 6000 series, which serves as a substitute for an excessive insertion of other iron. This was determined to be the optimal solution due to the precise iron quantity required to maintain optimal field quality. The iron yoke has an almost rectangular shape with rounded corners to limit multiple variations as the magnetic field increases. Only the collars have a structural role, while the iron yoke serves as a magnetic component [36]. With the help of these design choices, the necessary magnetic field can be produced. A field map within the magnet is presented in Figure 2.6, which has been simulated in COMSOL Multiphysics® using a model generated by STEAM py-SIGMA[39][40].

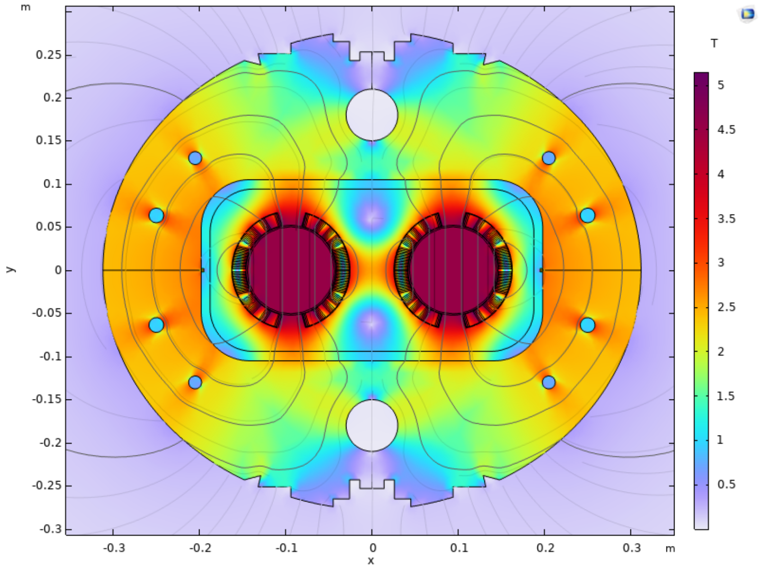

Figure 2.6: Field map of the MBRD magnet simulated in COMSOL Multiphysics® [39] [40].

2.5 Impedance Measurements of the MBRD

Impedance measurements in the frequency or time domain can be used to identify and distinguish the impact of losses caused by different types of coupling currents. The presence of currents flowing in superconducting magnets results in a deviation from the ideal value of the impedance. The analysis of impedance enables the prediction of the electrodynamic response and the observation of alterations in the impedance curve over time, which can facilitate the detection of potential malfunctions.

At CERN's superconducting magnet test facility, also known as SM18, every magnet is tested at cryogenic temperature in realistic conditions as well as at room temperature. The facility contains both vertical and horizontal testbenches, allowing for prototype testing of magnets up to a maximum length of 16 m (on horizontal testbenches) or 4 m (on vertical testbenches). These testbenches are equipped with cryostats capable of reaching a temperature of 1.9 K and delivering up to 30 kA of current [41].

The Electrical Quality Assurance (ELQA) at CERN has developed a system able to test and validate the superconducting circuits of LHC. A typical superconducting magnet circuit comprises superconducting coils, superconducting bus bars, current leads (that provide the transition between the superconducting and normal conducting parts of the circuit), warm cables leading to the power converter, and voltage pickups placed mostly on the cold part of the circuit. These pickups are used by quench protection systems and for diagnostics.

Among the different types of measurements that can be performed, there is the Transfer Function Measurement (TFM), in which the circuit under test is powered with AC current and the impedance is measured for different frequencies in the range from 1 Hz to 100 kHz[42].

A prototype of the Main Bending Recombination Dipole magnet has recently been tested in the SM18 facility using the ELQA measurement system. This testing allowed for numerous measurements to be taken under different conditions, both at room temperature and cryogenic temperature. Furthermore, measurements were performed which included the insertion of shorts between different turns, made possible by the presence of multiple voltage taps. The data collected provides a comprehensive set of impedance measurements at different temperatures and conditions, enabling the validation of the model presented in this master's thesis for MBRD.

The measurement setup used for the MBRD measurements is shown in Figure 2.7. It consists of an AC voltage source,V_{AC} [V], capable of providing up to 10 V, which generates a sinusoidal excitation current, I_{Ex} [A].

An isolation amplifier is used to mitigate the effects of noise and to insulate the circuit from ground. This guarantees that all available current can be directed into the magnet circuit and fully recovered. The design includes a reference resistor, $R_{ref} = 25\ \Omega$, and the magnet circuit itself, which consists of four coils. The Main Bending and Recombination Dipole is indeed a dipole magnet, meaning that each of its two apertures contains two coils.

Current is injected into the outer turn of the upper coil of the first aperture and collected by the outer turn of the lower coil of the second aperture. It flows through the turns of each coil, following the arrows in the diagram, before exiting the magnet. The voltage across the magnet can be measured at several voltage taps (shown as orange circles in the diagram)

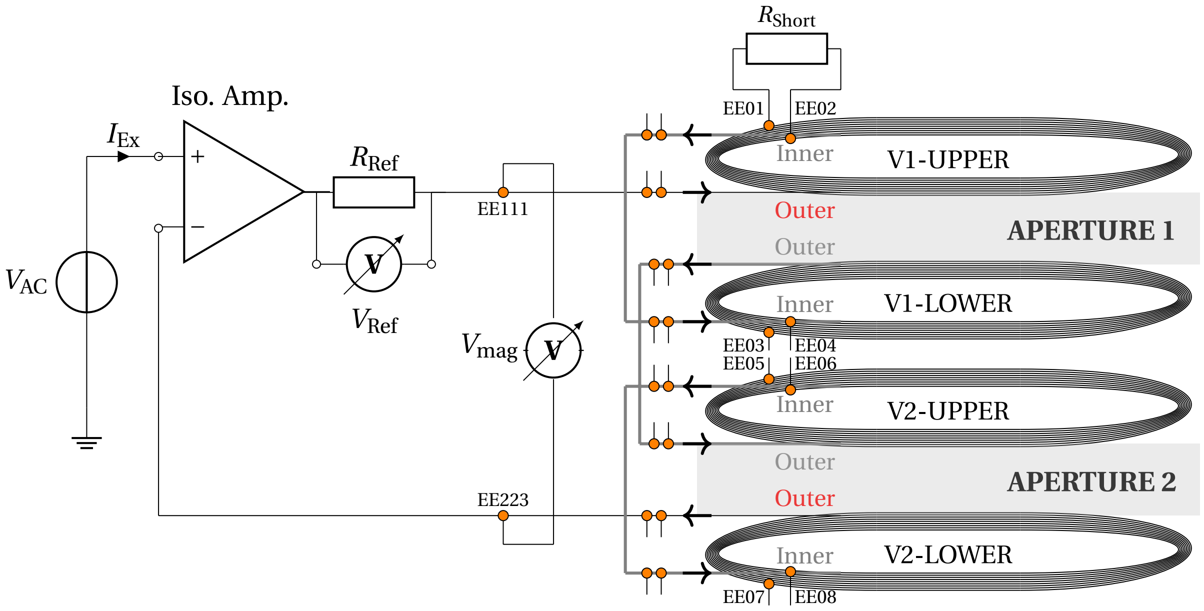

Figure 2.7: Measurement system for the MBRD full magnet, which comprises different voltage taps (orange circles) for measuring the voltage across different turns. A short resistance is also included for the purpose of illustrating how two turns can be shorted.

using a gain phase analyzer in order to account for both its real and imaginary parts.
It is possible to measure the voltage across the whole magnet using voltage taps EE111 and EE223, as shown in Figure 2.7, or across individual turns of the same coil or different coils. The measured voltage is then used to calculate the complex impedance of the magnet using the following formula:

$$\mathbf{Z}_{\text{mag}} = \frac{\mathbf{V}_{\text{mag}}}{\mathbf{V}_{\text{Ref}}} R_{\text{Ref}} \quad [\Omega] \tag{2.19}$$

where V_{Ref} [V] is the voltage measured with a gain phase analyzer across the reference resistor and V_{mag} [V] is the voltage measured across the specified voltage taps.
In addition, the voltage taps can be used to simulate short circuits across different turns by connecting an external resistor of the desired value, as shown in Figure 2.7. This allows measurements to be made under different conditions.

Impedance Modeling and Automatic Model Generation

The task of accurately simulating the electromagnetic transients of superconducting magnets is extremely challenging due to the many non-linear effects that affect their behavior, such as AC losses, and their multi-scale nature [43]. Network modeling has proven to be a computationally inexpensive technique for simulating the behavior of superconducting circuits in the frequency domain.

However, while some models based on network modeling exist in literature, they either lack physical interpretability [44], cannot easily simulate faults [45], or fail to consider non-linear electromagnetic effects [46] since they cannot relate the non-linear effects to the corresponding elements in the network. To address these challenges, it was therefore necessary to develop a two-dimensional lumped-element model to accurately reproduce superconducting magnet impedances and investigate failures [10].

This model can easily incorporate various dynamic effects, such as inter-filament and inter-strands coupling currents, and eddy currents in the copper sheaths and metallic components of the magnets. It has been validated at different temperatures by comparison with transfer function measurements of the complex impedance at different frequencies for the LHC's main dipole and the magnets installed in the tunnel. The network parameters for this physically driven lumped element are calculated using analytical equations or data extracted from specific pre-simulated Finite Element Models [10].

The main objective of this Master's thesis project is to develop and validate a model for investigating failures in superconducting magnets by accurately simulating the complex impedance of any accelerator magnet using the STEAM framework. This involves performing finite element simulations on conductive magnet components that suffer from losses due to eddy currents, which are challenging to model using analytical formulas due to complex geometries and field distribution.

A tool will be created within the STEAM framework to integrate essential data from these FEM simulations, evaluate additional coupling losses through analytical formulas and systematically collect and process all relevant data from various elements in the network model. Subsequently, the network will be constructed and saved in a .lib file for simulation in Xyce. Xyce [47] is a simulation software designed for large-scale parallel computing. It is capable of efficiently handling complex circuit simulations by distributing tasks across multiple processors. In the context of this thesis, Xyce will be used to extract the voltage and current in various locations of the network model allowing for the evaluation of the impedance.

This approach will enable the precise frequency-domain simulation of the complex impedance for each accelerator magnet.

This chapter outlines the theoretical basis for the tool, the FEM simulation methods using COMSOL Multiphysics® and the development of the tool within the STEAM framework.

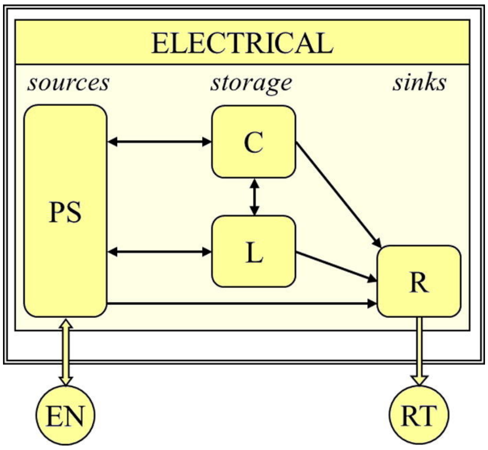

Figure 3.1: Scheme of the electrical subsystem in a LEDET model [28].

3.1 Lumped elements modeling

Discrete element modelling is an accurate method for modelling physical systems. It allows the representation of a potentially infinite dimensional state space to be reduced to a finite number of idealised components connected by a known topology. This approach allows the use of mesh representation in various domains such as electrical, mechanical, thermal and others. The topology of the Lumped Element Models (LEM) makes it possible to establish links between the various parameters, ensuring good agreement with the physics on which the model is based [48].

The modeling and simulation of electromagnetic transients in superconducting magnets is challenging because of the many effects that must be taken into account. The lumped element model provides an effective way to reproduce the behaviour using a limited number of differential-algebraic equations. The Lumped-Element Dynamic Electro-Thermal (LEDET) model developed at CERN [28] provides an efficient way to accurately represent an electrical subsystem. As shown in Figure 3.1, in the electrical domain, energy is generated by the power source PS [W], while capacitors C [F] and inductors L [H] act as storage elements and resistors R [Ω] as dissipative elements. The electrical network (EN) acts as the energy input, while the room temperature (RT) environment acts as the energy output [28].

It is therefore possible to reduce the study of electromagnetic transisents in superconducting magnets to several electrical subsystems coupled to each other. This approach makes it possible to preserve the physical properties of the system while reducing the complexity of the problem by minimising the number of elements and equations required to solve it.

In the context of lumped elements modeling, a superconducting magnet can be initially seen as a circuit composed of an inductance, a resistance in series, and a capacitance to ground. The inductance represents the magnet coils that generate the electromagnetic field. The resistance refers to the resistive part of the superconducting magnet that could be present at cryogenic temperatures if a part of the magnet suddenly transitions to a normal state. Lastly, the capacitance denotes the stored energy due to the electromagnetic interaction of the magnet elements, mostly to ground.

By measuring the total impedance of this circuit, it is possible to observe the contribution of

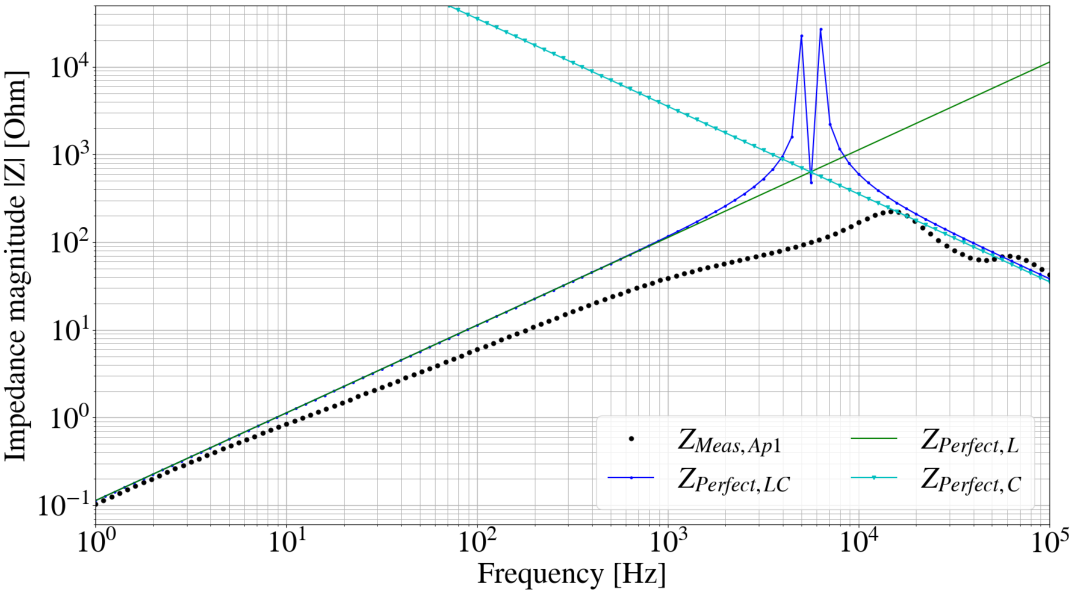

Figure 3.2: Measurement of a stand-alone dipole, the MBRD, at 1.9 K.

each component:

$$Z_{\mathrm{Mag}} = Z_{\mathrm{R}} + Z_{\mathrm{L}} + Z_{\mathrm{C}} = R + j\omega C + \frac{1}{j\omega L} \quad [\Omega] \tag{3.1}$$

As written in Equation 3.1, the resistance contribution is noticeable only as an offset value at low frequencies. For magnets in a superconducting state, the resistance should be zero. The inductance contribution instead increases linearly with the frequency, and the capacitance contribution decreases linearly with the frequency.

The ideal impedance curve, $Z_{\mathrm{Perfect,LC}}$ [Ω], shown in Figure 3.2, has an initial slope determined by the inductance value, a resonance peak near the intersection, and a decreasing slope determined by the capacitance value. However, the measured impedance differs significantly from the ideal curve due to non-linear effects in the magnet.

For frequencies up to 10 kHz, the main factor causing deviation from the ideal value is the coupling losses that are generated in the magnet components and affect the overall magnet behavior. After the resonance peak, the main contribution comes from the frequency-dependent parameters of the capacitance [49].

This difference highlights the importance of having a validated model to accurately simulate the impedance of a superconducting magnet through the impedance, in order to validate its behavior and to simulate non-conformities.

3.2 Model Overview

In order to accurately simulate the impedance of superconducting magnets, it was necessary to develop a specialised tool that could streamline the entire process. This tool was designed to automate the collection of various magnet data, create a comprehensive network model, and perform lumped equivalent element calculations based on parameters derived

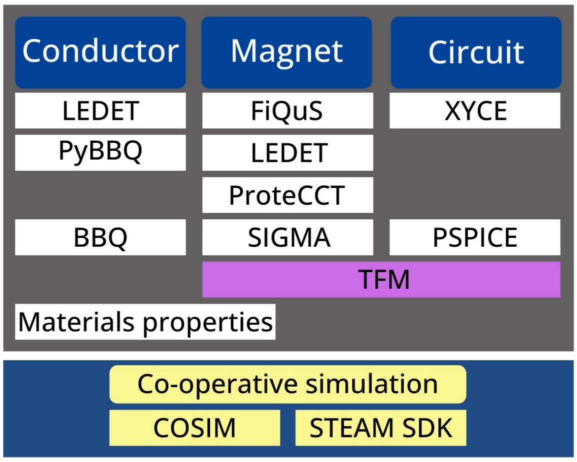

Figure 3.3: Block-scheme of the STEAM framework, including all the principal tools [50].

from either the COMSOL Multiphysics® simulations or analytical equations.

The new simulation tool, designated as TFM (Transfer Function Measurement), enables the precise impedance simulation of superconducting magnets and superconducting magnet circuits within the frequency domain. This tool addresses various lossy effects that can affect the impedance behavior of such systems.

A critical aspect of the development of this tool was its integration into the STEAM framework, which already contains a wealth of magnet-related data and sophisticated simulation capabilities. By embedding the tool within STEAM, the process of simulating superconducting magnet impedance became much more efficient and user-friendly. This integration not only leveraged existing data, but also ensured a smoother and more straightforward simulation workflow, minimising manual input and reducing the potential for error. As a result, the tool enables more accurate and reliable analysis of superconducting magnet performance.

3.2.1 STEAM framework and Data Flow

The STEAM framework consists of a heterogeneous set of tools, as illustrated in Figure 3.3, designed to interact seamlessly with each other, written in either Python, Java or C. This allows users to choose the most appropriate tool for the task at hand.

A notable feature of the STEAM framework is its unified approach to element definitions, where all tools within the framework are based on a single, consistent definition for each element. This implementation choice eliminates the need to define elements in multiple places, thereby reducing the likelihood of inconsistencies and errors between different tools. To further maintain consistency across the different tools, the input files that need to be provided to the STEAM tools are mostly YAML (Ain't Markup Language) files, which are text documents formatted using a human-readable data serialization standard, ensuring simplicity and readability [50].

The integration of the TFM tool, developed in this master's thesis, into the STEAM framework is illustrated in Figure 3.4. The figure shows how the tool interacts with other components in the framework, as well as the inputs, outputs, and processes required to efficiently produce accurate impedance simulations.

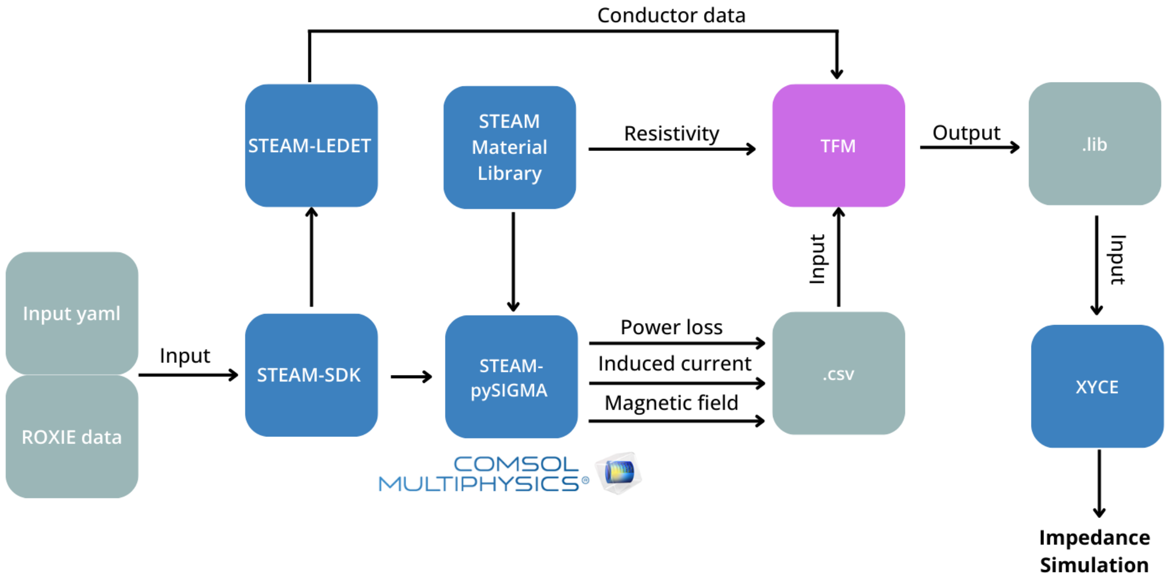

Figure 3.4: This diagram illustrates the data flow involved in creating an accurate impedance simulation using the TFM tool.

A number of key components of the STEAM framework were used in the development of the new simulation tool, including the STEAM SDK, LEDET, the STEAM material library, XYCE and SIGMA. These tools were instrumental in facilitating the development of the tool at various stages, including the collection of key physical and electromagnetic parameters of the magnets and cables, the management of material data and the simulation of circuits.
As shown in Figure 3.4, STEAM-SDK uses the magnet data and ROXIE data from input yaml files to generate output files that are fed into STEAM-pySIGMA and STEAM-LEDET. The ROXIE program package, which stands for "Routine for the Optimization of magnet X-sections, Inverse field calculation and coil End design," was created at CERN with the goal of optimizing the design of superconducting magnets. It has several features, including the ability to design superconducting coils, optimize fields, calculate the field in iron without meshing the coils, and make it easier to interface between ROXIE and CAD tools [51].
To proceed with the impedance simulation through the TFM tool, three fundamental types of input are required: conductor data from STEAM-LEDET, resistivity values for the magnet components' materials provided by the STEAM material library, and output files simulated in the COMSOL Multiphysics® models created using STEAM-pySIGMA.
The following sections will explain in detail the basic principles of the network model underlying the tool, in section 3.3; the process of the FEM simulations in COMSOL Multiphysics®, in section 3.4; and the foundation of the TFM tool development, including its data structure and library file generation, in section 3.6.

3.3 Network model

In the proposed network model, superconducting magnets can be represented by the circuit described in 3.1, comprising inductances and resistances connected in series, along with stray capacitances to ground. The inductance is the magnet main inductance L_{mag} [H],

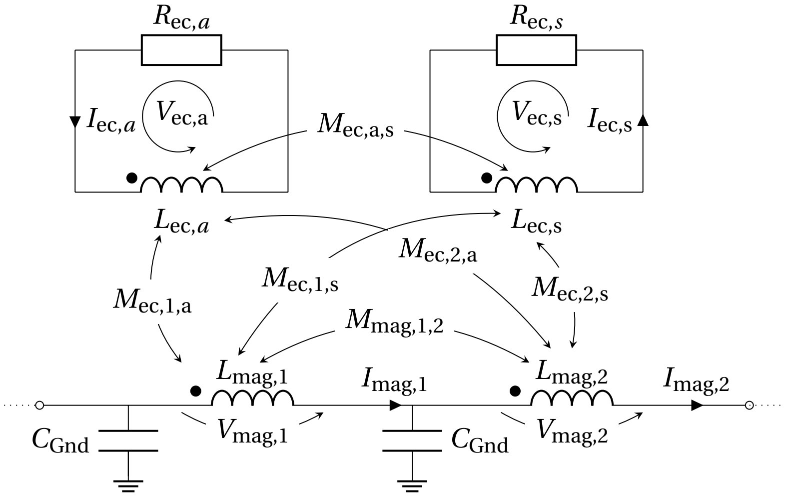

Figure 3.5: Lumped element network model representing two equivalent loops coupled to two turns of a magnet [10].

which can be either stand-alone or divided into multiple components, for example, according to the number of turns or apertures [10]. Several non-linear effects affect the magnets ideal behaviour and hence their impedance. One way to model these effects efficiently is to represent each of these effects by a coupling loop. This allows to have a model that is manageable without being too complex, with a convenient number of elements, equations and parameters.

Since they represent the non-linear effects present in each part of the superconducting cables, these loops are coupled to each inductance of the magnetic circuit and they are also coupled to each other through specific mutual inductances $\mathrm{M_{ec}}$ [H].

As can be seen in the example of Figure 3.5 for a network model composed of two turns coupled to two coupling loops, these closed loops are composed of an energy storage element, the inductance $\mathrm{L_{ec}}$ [H], a dissipative element $\mathrm{R_{ec}}$ [Ω] and a specific current $\mathrm{I_{ec}}$ [A]. This approach allows multiple effects to be taken into account efficiently, such as inter-filament and inter-strands coupling currents, eddy currents in the copper matrix, eddy currents in magnetic components such as the wedges, cold bore, aluminum ring and coil protection sheets. The power loss $\mathrm{P_{ec}}$ [W] and the induced current I_{ec} in each lossy volume and the time constant τ_{ec} [s] of the different effects are required in order to calculate the equivalent lumped-element parameters of the coupling loops [52]. They can either be found using specific finite element models, as in the case of cold bores, wedges, aluminum rings, and coil protection sheets, or they can be calculated analytically, as in the case of inter-filament and inter-strand coupling currents and the eddy current in the copper sheaths.

3.3.1 Mutual coupling between different effects

The various coupling loops are interconnected as a consequence of the contribution of the magnetic field generated by each loop to the overall magnetic field. A modification of the external magnetic field induces a corresponding alteration in the magnetic field generated in response by each domain, thereby influencing the impact of coupling losses on the magnet's

impedance. It is thus imperative to incorporate a mutual coupling inductance term, designated as $\mathrm{M}_{\mathrm{ec,a,s}}$ [H] in Figure 3.5, for each pair of coupling loops within the network model. To evaluate this coupling, the mutual inductance of the physical coupled loop and the mutual inductance of the network uncoupled loop with the addition of $\mathrm{M}_{\mathrm{ec,a,s}}$, must be compared. The mutual inductance of the coupled loop $\mathrm{M}_{\mathrm{ec,1,a}}$ [H] is calculated by accounting for the magnetic field produced by the other loop as a result of its time-varying current $\dot{I}^{*}_{\mathrm{ec,s}}$ [A].
In the case of effects acting in the same volume, such as the IFCL and CSCL, it is possible to use the field attenuation factor $\alpha^{*}_{\mathrm{IFCL}}$ [-] parameter when analytically calculating their mutual inductance in order to account for the appropriate contributions. In order to achieve this with effects acting in different domains, it is instead necessary to evaluate the overall magnetic field including the contribution of the magnetic field generated by the other effect [10]:

$$M_{\mathrm{ec,a,s}} = \frac{1}{\dot{I}_{ec,s} M^{*}_{\mathrm{ec,1,a}}} \left[\dot{I}_{\mathrm{Mag}}\big((M_{\mathrm{ec,1,a}})^2 - (M^{*}_{\mathrm{ec,1,a}})^2\big) + R_{\mathrm{ec,a}}(M_{\mathrm{ec,1,a}} I_{\mathrm{ec,a}} - M^{*}_{\mathrm{ec,1,a}} I^{*}_{\mathrm{ec,a}}) \right] \quad [H] \tag{3.2}$$

where the current flowing in the physically coupled loop is represented by $\mathrm{I}_{\mathrm{ec,a}}$ [A], while the mutual inductance of the uncoupled loop and the current flowing through it are represented by $M^{*}_{\mathrm{ec,1,a}}$ [H] and $\mathrm{I}^{*}_{\mathrm{ec,a}}$ [A], respectively.
The incorporation of mutual inductances into the network model offers a realistic representation of the impact of each effect on the magnet behavior.

3.3.2 Equivalent lumped-element parameters

Since the eddy currents and the other coupling effects are represented by different types of mutual coupling loops, they have different equivalent parameters that need to be calculated differently. The eddy currents depend on the power loss, the induced current and the time constant in the lossy material in which they are generated.
The persistent currents is the only effect which, due to its special characteristics, is an exception to the network model presented in Figure 3.5 and therefore has to be modelled with special loops. In fact, they develop instantaneously when there is a change in the external

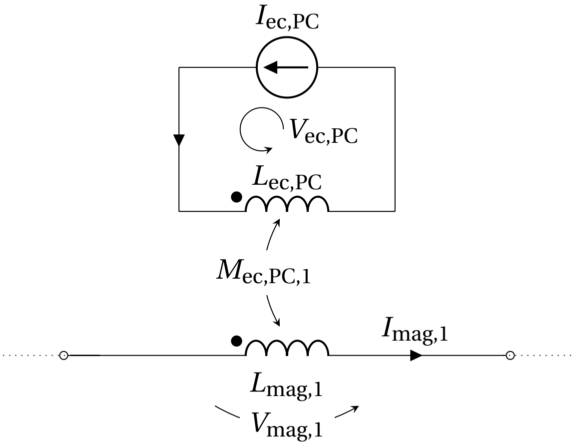

Figure 3.6: Lumped element network model representing a persistent currents equivalent loop coupled to a magnet inductance [10].

Table 3.1: Formulas for the calculation of the persistent currents and eddy currents coupling loops parameters [10].

Eddy currents parameters		**Persistent currents parameters**	
$R_{\mathrm{ec}} = \frac{P_{\mathrm{ec}}}{I_{\mathrm{ec}}^2}$	[Ω]	$I_{\mathrm{ec,PC}} = M(T,B,M_{t-1}) \cdot d_{\mathrm{s}}$	[A]
$L_{\mathrm{ec}} = \tau_{\mathrm{ec}} R_{\mathrm{ec}}$	[H]	$L_{\mathrm{ec,PC}} = \mu_0 \frac{\pi}{4} l_{\mathrm{mag}}$	[H]
$M_{\mathrm{ec}} = \begin{cases} \frac{\dot{I}_{\mathrm{ec}} L_{\mathrm{ec}} + R_{\mathrm{ec,a}} I_{\mathrm{ec}}}{\dot{I}_{\mathrm{mag}}} & \forall\ \mathrm{t}\ \text{s.t.} \dot{I}_{\mathrm{mag}} \neq 0 \\ 0 & \text{otherwise} \end{cases}$	[H]	$M_{\mathrm{ec,PC}} = \mu_0 \frac{\pi}{4} d_{\mathrm{s}} l_{\mathrm{mag}} f_{\mathrm{h}} \alpha_{\mathrm{CMCL}}$	[H]

magnetic field, so they do not have a time constant. They also flow through the superconducting parts of the cable, so they have no resistance.
Due to these reasons, the persistent currents can be represented as in Figure 3.6, using a ideal current generator $\mathrm{I}_{\mathrm{ec,PC}}$ [A] and an inductance $\mathrm{L}_{\mathrm{ec,PC}}$ [H] [10].The persistent currents parameters instead depend on the magnetisation level, the effective magnetic field after attenuation by inter-strand coupling currents and eddy currents in the copper matrix, and geometrical parameters, as can be seen in Table 3.1. f_{H} [T/A] is the magnetic transfer function coefficient that accounts for the field attenuation caused by the inter-strand coupling currents and can be found as [10]:

$$f_H = \sqrt{f_{\mathrm{x}}^2 + f_{\mathrm{y}}^2} \quad \left[\frac{T}{A}\right] \tag{3.3}$$

where f_{x} [T/A] and f_{y} [T/A] represent the ratio between the generated field in the x and y direction of the strands respectively per unit of nominal transport current [10].

3.4 FEM in COMSOL Multiphysics®

3.4.1 STEAM py-SIGMA tool

In order to create a finite element model of a superconducting magnet, the STEAM team at CERN created STEAM-SIGMA, a Java-based tool that creates accelerator magnet models in COMSOL Multiphysics®. Specifically, STEAM-pySIGMA, a Python wrapper of STEAM-

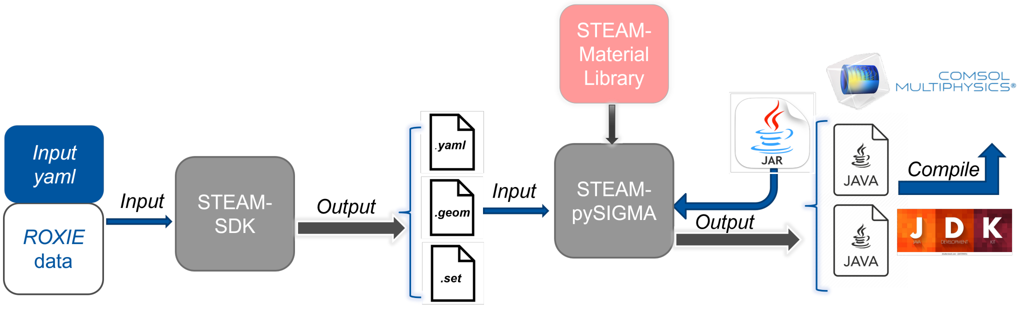

Figure 3.7: Block diagram showing the process of building a COMSOL Multiphysics® model using STEAM-pySIGMA. [39].

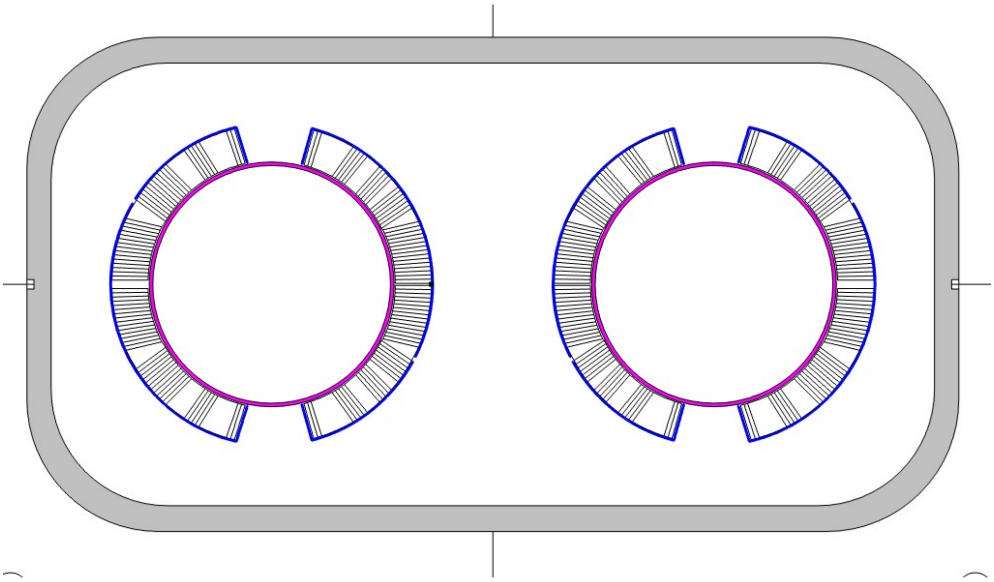

Figure 3.8: Zoom of the the MBRD COMSOL Multiphysics® geometry built using the STEAM-pySIGMA tool [39]. The manually added Coil-Protection Sheets (blue), Cold-Bores (magenta), and Aluminum ring (gray) are highlighted.

SIGMA that enables Python language interaction with the tool, was employed for this project [39]. This tool is a part of the STEAM-SDK [53] which is in charge of giving pySIGMA all the input files and magnet data required to construct the COMSOL Multiphysics® model. This process involves using the STEAM material-library functions [54] to calculate the key material properties like resistivity, and thermal conductivity
By using the STEAM-SIGMA tool, it is then possible to generate COMSOL Multiphysics® models with defined and meshed geometry that features the materials corresponding to each element [55].

3.5 MBRD Simulation workflow

To accurately determine the equivalent lumped element parameters for the loops representing the eddy current flow in the magnet elements - including the wedges, cold bore, aluminium ring and coil protection sheet - individual COMSOL Multiphysics ® models were created for each component. This approach ensured accurate and detailed analysis of each element.
The MBRD model was created using the py-SIGMA tool, which facilitates the creation of comprehensive COMSOL Multiphysics® models. This model included the coil geometry, iron yoke, collars and wedges as basic components. Once the initial model was established, additional elements such as the cold bore, aluminium ring and coil protection sheets were incorporated as shown in Figure 3.8. The aluminium ring and the coil protection sheets were designed based on the geometric parameters provided in [56] and [57] respectively. The cold bore was modeled with an outer radius of 0.0052 m and a thickness of 0.00015 m.
The workflow used to create and simulate each model element followed a consistent methodology described in the following sections:

Setting Magnetic and Electric Modules In order to simulate the magnet impedance and compute the power loss and the induced current in each domain, an electrical circuit module was incorporated into the COMSOL Multiphysics models ®.
The circuit, illustrated in Figure 3.9, was chosen in order to match the measurement setup in Figure 2.7. It includes an AC current source with a peak of 1 A, a series resistance R_{Ref} of 25 Ω, the magnet element represented with the U vs. I block, a second resistance of 1 pΩ in a recirculating loop, and two capacitances to ground of 125 nF each, and a resistance to ground R3 of 100 GΩ. The resistance R_{Ref} serves as a reference for the extraction of the input current I_{Ref} [A] flowing in the magnet element. In contrast, the resistance R3 has a very high value to ensure that the current flows in the feedback loop.
Additionally, in each COMSOL Multiphysics ® model, a magnetic module was defined with an out-of-plane thickness of 1 m and an induced AC current of 1 A in the coils. In order to couple the magnetic and electric domains, it was necessary to ensure that the voltage reference for the magnet in the COMSOL Multiphysics® model (using the U vs. I module) matched the voltage defined for the coils in the magnetic module. The lossy element was defined as a passive conductor within the magnet domain, allowing observation of the induced current resulting from the time-varying magnetic field produced by the AC current in the coils.

Impedance Simulation To simulate the magnet impedance, a frequency study with 121 logarithmically spaced frequency values between 1 Hz and 100 kHz was conducted. The entire circuit module was included in this frequency simulation, and impedance was calculated as the ratio of the voltage across the magnet element to the current through resistance R_{Ref}, as in Equation 2.19. By plotting the impedance for models that include various passive conductors, it is possible to observe how eddy current losses in different magnetic elements affect the overall magnet impedance.

Power Loss and Induced Current Simulation A similar frequency sweep was performed to simulate the power dissipation and induced current caused by the time-varying magnetic field generated by the current in the coil. However, in this frequency sweep the capacitors were not part of the circuit. The induced current was determined by integrating the current resulting from the magnetic field simulation in the lossy element and the power dissipation

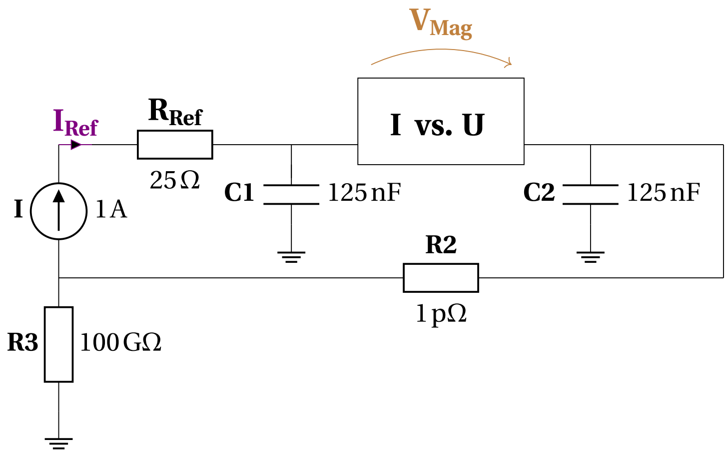

Figure 3.9: Representation of the electrical circuit added in the MBRD COMSOL Multiphysics® models.

was calculated by integrating the power in the volume of the lossy element.

Time constant Simulation A transient simulation was conducted to verify the time constant of each effect. In this instance, the electric circuit was deactivated and instead of utilizing the AC current source, an alternative current generator was defined. A current ramp was defined as $i_{\text{scr}} = 1 * t * \omega$ [A], where t [s] is the time sweep defined in the simulation. The time constant can be identified in correspondence with the first bump of the induced current and power loss curves, before stabilizing at a constant value. This phenomenon occurs due to the shielding effect of the induced current, which opposes the applied field change.
An estimation of the time constant can be obtained by calculating the time at which the induced current in the lossy element reaches its steady state, around $\left(1-\frac{1}{e}\right)$ of its full value. Each coupling effect introduces a deviation from the ideal impedance curve, which manifests as a bump at the frequency corresponding to $f \propto \frac{1}{\tau}$. This represents the frequency at which the time constant, τ, exerts a considerable influence on the system's response, resulting in a transient increase in impedance before reaching a stable state. By analysing these bumps, one can determine the specific time constants associated with different effects.

Magnetic field generated by each lossy element Furthermore, the eddy currents flowing inside the lossy elements generate a magnetic field that affects the other losses by modifying the total magnetic field acting in each magnet's element. In order to incorporate this mutual coupling effect into the simulation, the magnetic field was extracted from the frequency simulation in which no capacitance was present in the circuit. To this end, a coordinate file containing all the x and y coordinates of the strands in the magnet, extracted from ROXIE, was applied to the COMSOL Multiphysics ® models.
The resulting magnetic field values from the simulation were then calculated at each of these positions and exported to be included in the simulations in the TFM tool.

3.5.1 Wedges

The superconducting magnet's wedges are composed of copper, with their resistivity defined using the copper resistivity function from the STEAM material library [54]. In order to accurately simulate the behavior of the wedges, each wedge domain was modeled as an independent passive conductor. This approach guarantees that no current flows between

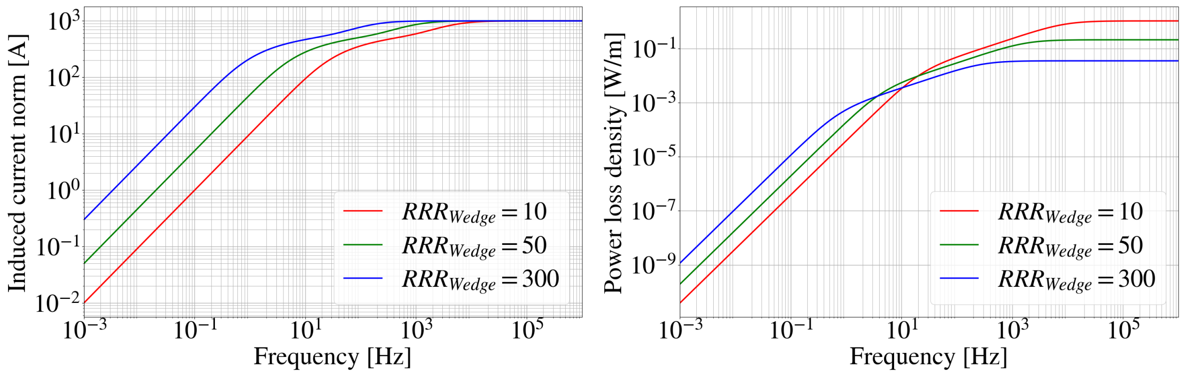

Figure 3.10: Power loss and induced current in the wedges for different RRR at 1.9 K

different wedges, as they are electrically isolated from one another.

A significant challenge in simulating the wedges is determining the RRR. The RRR is a measure of the purity of the copper, with a higher RRR indicating higher conductivity, particularly at cryogenic temperatures. This increased conductivity consequently results in the generation of larger induced currents within the wedges. The RRR also exerts a direct influence on the time constant of the system, which constitutes a crucial factor in determining the frequency at which eddy current losses in the wedges begin to significantly impact the impedance curve of the magnet. To understand how different RRR values impact power loss and the associated time constant, a frequency sweep was performed for three representative RRR values: 10, 50, and 300. These values typically represent the range of potential RRRs in practical scenarios. As illustrated in Figure 3.10, at higher frequencies, there is an inverse relationship between power dissipation in the wedges and resistance.

In particular, an high resistance (lower RRR) is associated with diminished power dissipation. This phenomenon can be attributed to the fact that a higher RRR gives rise to an higher time constant, which, in turn, corresponds to a larger skin depth. The larger skin depth implies that the induced currents penetrate deeper into the material, effectively reducing the volume of the conductor that is actively carrying current at higher frequencies. Consequently, the effective volume where power dissipation occurs decreases, resulting in reduced power loss.

3.5.2 Cold Bore

The cold bores are made of stainless steel and their resistivity is defined using the corresponding resistivity function from the STEAM material library, which corresponds to $\rho_{SS} = 680\text{n}\Omega \cdot \text{m}$ at 1.9 K [54]. There are two symmetrical cold bores, one per aperture, which do not interfere with each other. Looking at the power loss and induced current curves in Figure 3.11, it can be seen that the time constant occurs in the vicinity of the first bump in the curves, which is around 10 kHz.

From the time domain simulation it was indeed found that the time constant associated with the losses in the cold bore is 124 μs, corresponding to a frequency of around 8 kHz.

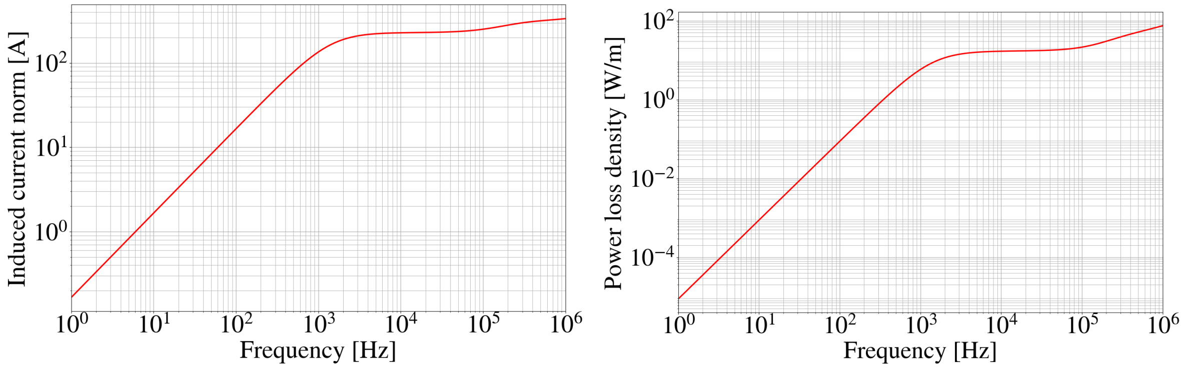

Figure 3.11: Power loss and induced current in the cold bores at 1.9 K

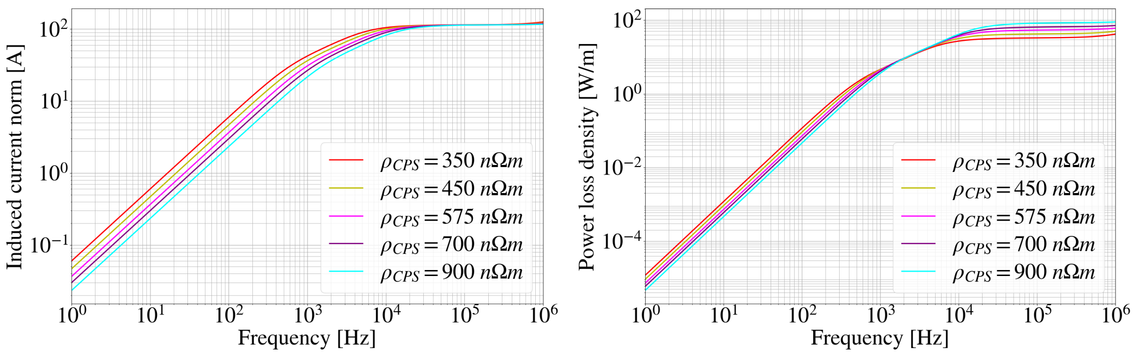

Figure 3.12: Power loss and induced current in the coil protection sheets at 1.9 K

3.5.3 Coil-Protection Sheets

The coil-protection sheets exhibit a more intricate geometry and are composed of stainless steel, whose resistivity is derived from the STEAM material library as in 3.5.2 [54]. The aforementioned sheets are situated in close proximity to the coils, as illustrated in Figure 3.8. The sheets are 0.4 mm thick and are positioned at a distance of only 0.3 mm from the end of the coil diameter. Furthermore, the design incorporates a space on the middle plane on either side of the aperture, rather than uniting them entirely. From one aperture to the other, they are mirrored.

As can be seen in Figure 3.12, the impact of the losses in the Coil Protection Sheets becomes evident in the impedance curve around 2 kHz because the found time constant, for its nominal resistivity of $\rho_{SS} = 680\text{n}\Omega \cdot m$, is around 0.427 ms.

3.5.4 Aluminium Ring

The aluminum ring is the sole component capable of spanning both apertures. The width of the ring is 10.95 mm. It has a rectangular shape with rounded corners, with dimensions of 398 mm for the longer side and 211 mm for the shorter side. The ring is constructed from laminated aluminium, which results in a different resistivity compared to standard aluminium. Despite the resistivity of the laminated aluminum being known, it is challenging to accurately scale and represent it in a two-dimensional model. In [58], it is written that the conductivity in the z direction in a laminated material can be approximated as follows: The value of the conductivity of the original not laminated material, represented by the variable σ [S/m], can be approximated by the following equation:

$$\sigma_z = \frac{1}{n^2} \cdot \sigma \quad [S/m] \tag{3.4}$$

where n [-] is the number of laminations.

As indicated in [37] the aluminum sleeves are 100 mm thick, necessitating the use of 78 laminated sleeves to achieve full coverage of the 7.8 m length of the magnet. The resistivity of aluminum at 1.9K is approximately $10^{-12}\ \Omega \cdot \text{m}$, although this can vary depending on the purity of the aluminum. However, this approximated resistivity value, found using Equation 3.4 using n=78, proved to be incorrect. Indeed, when simulating the effect of the eddy currents

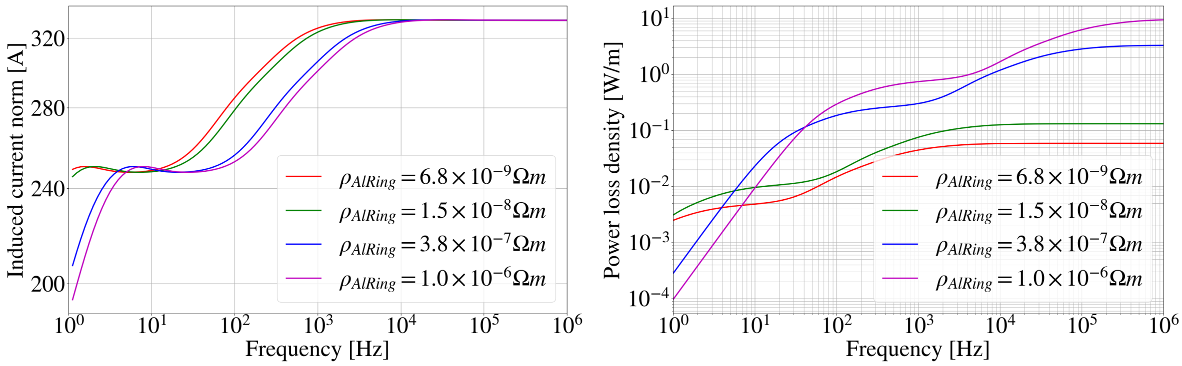

Figure 3.13: Power loss and induced current in the aluminum ring at 1.9 K simulated for 20 different aluminum resistivity values between $6.83 * 10^{-09}$ Ω·m to $1 * 10^{-06}$ Ω·m

flowing in the aluminum ring on the magnet impedance, the simulation results did not align with the measurements. The impedance simulation using the calculated resistivity value resulted in losses that were insufficient to accurately represent the eddy current effects on the magnet's impedance.

To address this issue, a range of feasible resistivity values for the laminated aluminum was identified, spanning from $6.83 \cdot 10^{-09}$ Ω·m to $1 \cdot 10^{-06}$ Ω·m. This range was determined by modelling the aluminum ring in a three-dimensional simulation using COMSOL Multiphysics®, analyzing the current paths, and then scaling the resistivity from the three-dimensional model to obtain a corresponding scaling value for the two-dimensional model. This approach allowed the selection of an appropriate range, which enabled the identification of a resistivity value that accurately reflected the losses generated by the aluminium ring.

A simulation of the power loss and induced current for 20 different aluminum resistivities within the specified range, as illustrated in Figure 3.13, revealed that an increase in the resistivity of the aluminum results in a reduction in the time constant, thereby enhancing the impact of the aluminum sleeves at higher frequencies.

3.6 Automated Model Generation

3.6.1 Tool Structure and Input Files

The developed tool was created to address various lossy effects that can affect the impedance behaviour of superconducting magnets. TFM is structured around different data classes, each representing a specific lossy effect. These data classes contain attributes that correspond to the equivalent parameters of the circuit loop representing that particular effect within the network model.

The process begins with the definition and storage of all relevant magnet and cable parameters in the dedicated data classes shown in Figure 3.14. These parameters are essential for the analytical calculation of the effects of different coupling currents. Once the parameters are set, the tool calculates the lumped element parameters for the various coupling effects either through specific analytical formulas or by retrieving data from pre-simulated COMSOL Multiphysics® tables, such as induced currents and power dissipation in the lossy domains.

The "Options" dataclass is used to manage various settings for the simulation. It contains several flags, each named after a specific effect that can be included in the simulation. When a flag is set to True, it indicates that the corresponding effect is incorporated in the simulation. If a flag is set to False, that effect will be excluded. This enables the simulation to be tailored by toggling the different effects on and off through these flags.

The TFM tool is particularly valuable for simulating the electromagnetic behaviour of complex systems because it allows the creation of different circuit networks based on the specific turns and effects that are needed to be simulated.

In order to utilise the tool, it is necessary to insert TFM as a key in the circuit input YAML file, as illustrated in Figure 3.15, and then conduct a circuit analysis. In this circuit file, a netlist must be provided that specifies the type of elements, their name, the node to which they are connected and their value.

The circuit configuration used to simulate the MBRD impedance is analogous to that depicted in Figure 3.9. The circuit comprises a resistance of 100 GΩ in series with an AC voltage source with a DC value of 10 V. Furthermore, a reference resistance, R_{ref}, with a value of 25 Ω, and a magnet element are included. In the case of the magnet element, four nodes are specified, indicating the locations where the inductance representing the two apertures should be placed. In this instance, the initial aperture is situated between EE_Ap1_In and EE_AP_MID, while the subsequent aperture is located between EE_AP_MID and EE_AP2_OUT. The nodes to which $V_{tap,\,cir}$ is connected permit the determination of whether the entire magnet is to be powered or just one of the two apertures.

The magnet element is defined as a parameterized component, which is not natively recognized by Xyce. Therefore, its definition must be provided in a specific library file, which TFM automatically generates with each tool invocation. This file is then imported into Xyce to retrieve the component's characteristics.

The input YAML file also allows customization of various simulation parameters. It is possible to include the desired effects by setting their corresponding flags to True, or to adjust the simulation temperature and frequency, modify the injected current, and alter certain geometric values, such as the radius r_{CB} [m] and thickness t_{CB} [m] of the cold bore. Additionally,

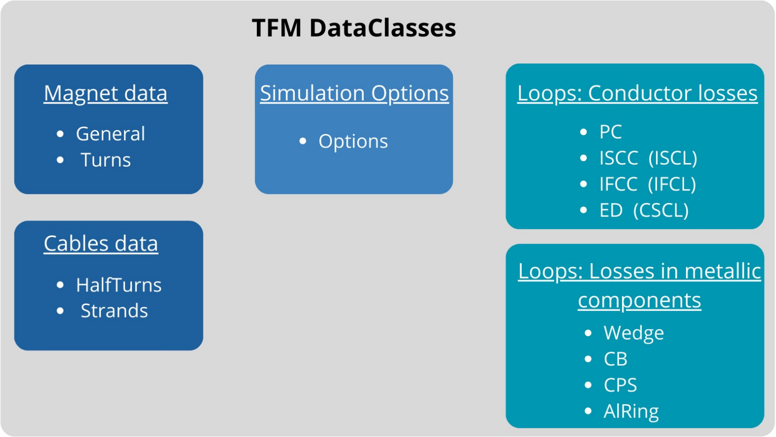

Figure 3.14: Diagram illustrating the various dataclasses included in TFM, grouped by purpose.

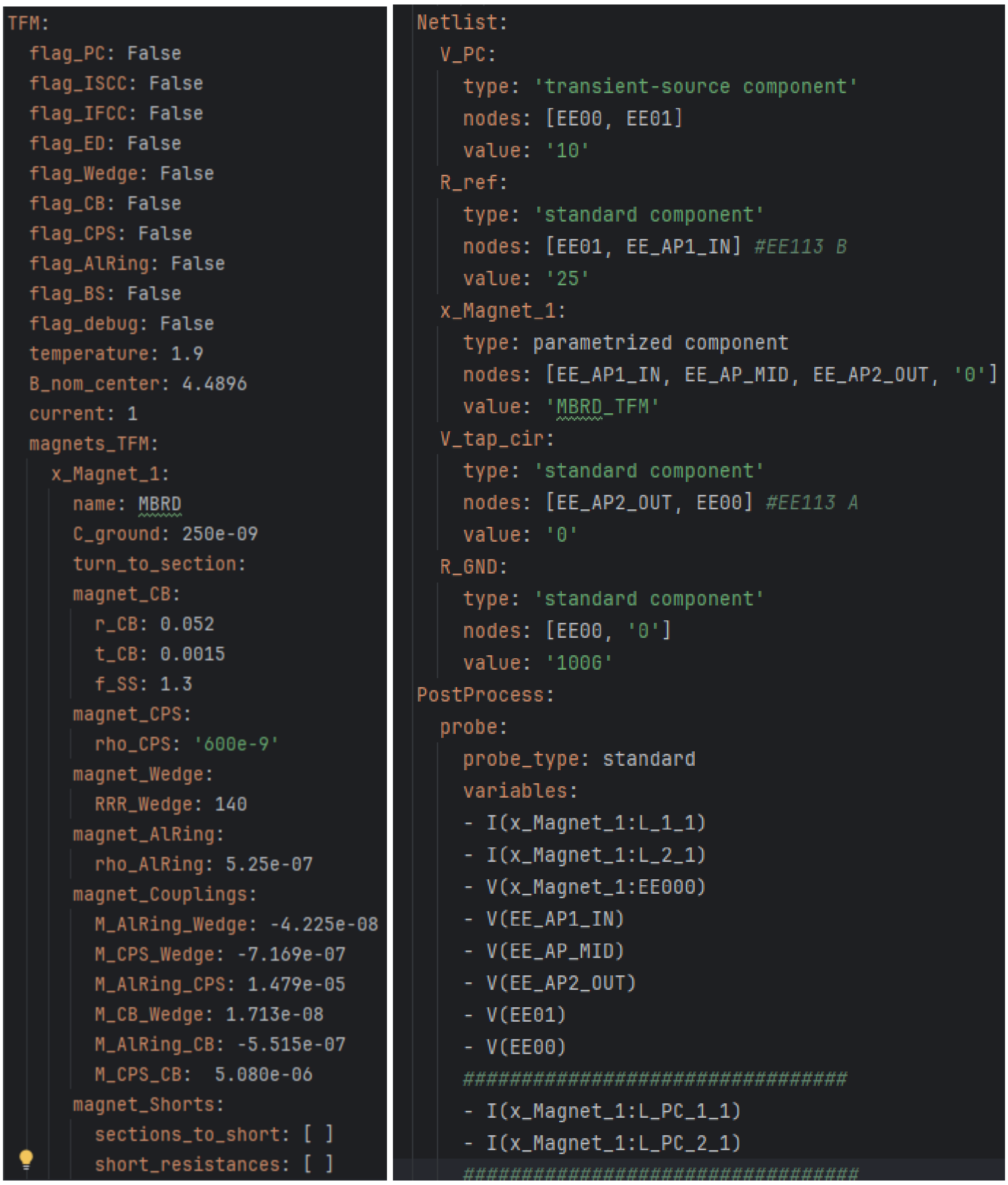

```yaml
TFM:
  flag_PC: False
  flag_ISCC: False
  flag_IFCC: False
  flag_ED: False
  flag_Wedge: False
  flag_CB: False
  flag_CPS: False
  flag_AlRing: False
  flag_BS: False
  flag_debug: False
  temperature: 1.9
  B_nom_center: 4.4896
  current: 1
  magnets_TFM:
    x_Magnet_1:
      name: MBRD
      C_ground: 250e-09
      turn_to_section:
      magnet_CB:
        r_CB: 0.052
        t_CB: 0.0015
        f_SS: 1.3
      magnet_CPS:
        rho_CPS: '600e-9'
      magnet_Wedge:
        RRR_Wedge: 140
      magnet_AlRing:
        rho_AlRing: 5.25e-07
      magnet_Couplings:
        M_AlRing_Wedge: -4.225e-08
        M_CPS_Wedge: -7.169e-07
        M_AlRing_CPS: 1.479e-05
        M_CB_Wedge: 1.713e-08
        M_AlRing_CB: -5.515e-07
        M_CPS_CB:  5.080e-06
      magnet_Shorts:
        sections_to_short: [ ]
        short_resistances: [ ]
```

```yaml
Netlist:
  V_PC:
    type: 'transient-source component'
    nodes: [EE00, EE01]
    value: '10'
  R_ref:
    type: 'standard component'
    nodes: [EE01, EE_AP1_IN] #EE113 B
    value: '25'
  x_Magnet_1:
    type: parametrized component
    nodes: [EE_AP1_IN, EE_AP_MID, EE_AP2_OUT, '0']
    value: 'MBRD_TFM'
  V_tap_cir:
    type: 'standard component'
    nodes: [EE_AP2_OUT, EE00] #EE113 A
    value: '0'
  R_GND:
    type: 'standard component'
    nodes: [EE00, '0']
    value: '100G'
PostProcess:
  probe:
    probe_type: standard
    variables:
    - I(x_Magnet_1:L_1_1)
    - I(x_Magnet_1:L_2_1)
    - V(x_Magnet_1:EE000)
    - V(EE_AP1_IN)
    - V(EE_AP_MID)
    - V(EE_AP2_OUT)
    - V(EE01)
    - V(EE00)
    #################################
    - I(x_Magnet_1:L_PC_1_1)
    - I(x_Magnet_1:L_PC_2_1)
    ##################################
```

Figure 3.15: Example of an input YAML file for launching TFM analyses of a circuit with a MBRD magnet.

is possible to change the resistivity of different materials and set the RRR of the Wedges. For example, as shown in Figure 3.15, setting the resistivity of the coil protection sheets ρ_{CPS} $[\Omega m]$ to 'SS' indicates that the resistivity used is that of stainless steel from the material library. It is also possible to adjust the Mutual coupling inductance values between the loops of different effects, by modifying the keys under "magnet_Couplings".

3.6.2 Library file generation

Library file generation is a key feature of the TFM tool. This process is carried out automatically by the tool based on the characteristics of the magnet and the effects to be simulated. In superconducting magnets, each strand within the magnet's cable contributes to the overall inductance. Ideally, for the most accurate simulation, each strand should be modelled as a separate sub-circuit in the network model. Each of these sub-circuits would then be coupled to various other sub-circuits in the network to accurately represent the electromagnetic interactions within the magnet. However, modelling each strand individually would result in an extremely large number of parameters, creating a model that is both highly complex and computationally expensive to solve.

To deal with this complexity, the TFM tool provides a more practical approach. Instead of modelling each individual circuit, the tool groups the circuits into a smaller number of subcircuits. The number of sub-circuits corresponds to the number of apertures, turns or coil groups within the magnet and can be defined by a key in the input yaml file parameter, "turn_to_section" as a list long as the number of turns with as value the sub-circuit to which that particular turn corresponds, which is called a section. By grouping the windings and coupling them appropriately, the TFM tool can provide insight into the behavior of the magnet without the need for an impractically large and time-consuming model.

This section is divided into three parts to explain the generation of the magnet circuit, the generation of the conductor losses loops and the loops associated with eddy current losses in the metallic components of the magnet. Each part provides an insight into how the tool constructs these elements to accurately simulate various effects.

Magnet network model When modeling the magnet circuit, two types of network can be generated depending on the wanted type of simulation. By default, if the "turn_to_section" key is left empty, the tool will generate a magnet circuit with as many sections as the number of apertures of the magnet. Each section consists of an inductance and a voltage tap. The inductance value represents the total inductance contributed by all strands within the aperture. Additionally, three capacitances are included in the circuit: one before the first subcircuit, one between the two apertures, and one after the second aperture. The sum of these capacitances equals the total capacitance to ground for the magnet.

For example, in the case of the MBRD magnet, which has two apertures, the resulting circuit can be seen in Figure 3.16. Two additional voltage taps are placed at the beginning and end of the magnet circuit to allow easy access to the input and output currents during XYCE simulations. All component nodes are automatically named by the tool, ensuring that an infinite number of subcircuits can be generated without any issue.

With this type of network circuit it is possible to simulate the voltage across the whole magnet or just the aperture.

If the goal of the simulation is to analyze the impedance of individual turns or groups of turns, it is possible to specify the number of groups each turn belongs to using the appropriate key in the input YAML file. In this scenario, the tool generates multiple sub-circuits for each aperture, with each sub-circuit containing the corresponding inductance and voltage taps. The rest of the circuit remains unchanged. The inductance of each group is calculated based on the number of turns within that sub-circuit, as the tool tracks the subdivision of turns throughout the process. An example of this configuration is shown in Figure 3.17.

Conductor losses coupling loops In order to create the coupling loops for the conductor loss effects, the same sectioning approach that was used for the magnet circuit is followed. However, an additional factor must be taken into account. Since the equivalent lumped

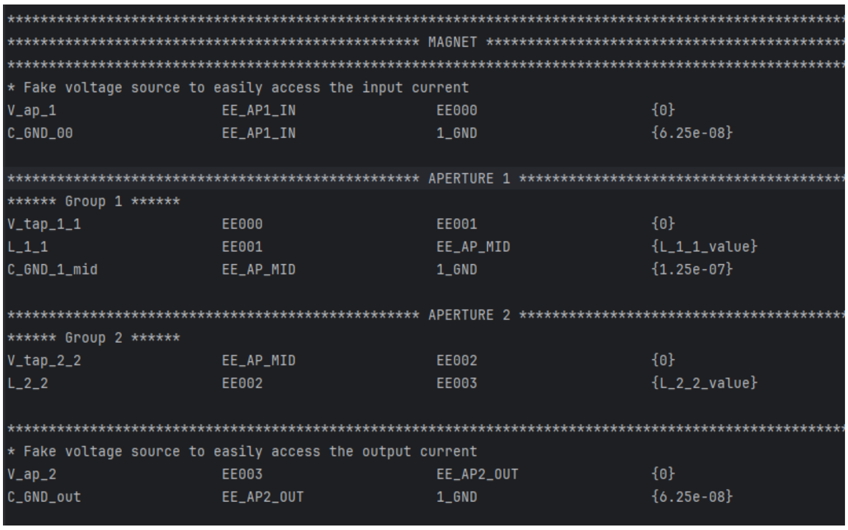

```
*****************************************************************************************************
************************************************** MAGNET *******************************************
*****************************************************************************************************
* Fake voltage source to easily access the input current
V_ap_1                    EE_AP1_IN                 EE000                     {0}
C_GND_00                  EE_AP1_IN                 1_GND                     {6.25e-08}

************************************************** APERTURE 1 ***************************************
****** Group 1 ******
V_tap_1_1                 EE000                     EE001                     {0}
L_1_1                     EE001                     EE_AP_MID                 {L_1_1_value}
C_GND_1_mid               EE_AP_MID                 1_GND                     {1.25e-07}

************************************************** APERTURE 2 ***************************************
****** Group 2 ******
V_tap_2_2                 EE_AP_MID                 EE002                     {0}
L_2_2                     EE002                     EE003                     {L_2_2_value}

*****************************************************************************************************
* Fake voltage source to easily access the output current
V_ap_2                    EE003                     EE_AP2_OUT                {0}
C_GND_out                 EE_AP2_OUT                1_GND                     {6.25e-08}
```

Figure 3.16: Example of the magnet circuit generated for the MBRD considering just one section per aperture.

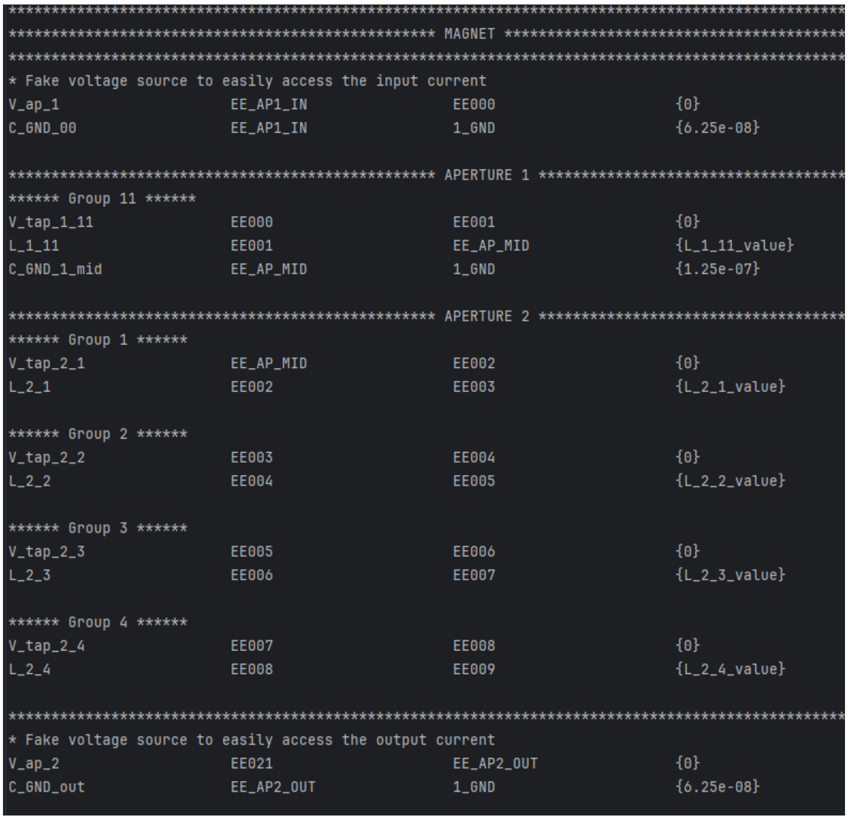

```
**************************************************************************************************
************************************************** MAGNET ****************************************
**************************************************************************************************
* Fake voltage source to easily access the input current
V_ap_1                    EE_AP1_IN                 EE000                     {0}
C_GND_00                  EE_AP1_IN                 1_GND                     {6.25e-08}

************************************************** APERTURE 1 ************************************
****** Group 11 ******
V_tap_1_11                EE000                     EE001                     {0}
L_1_11                    EE001                     EE_AP_MID                 {L_1_11_value}
C_GND_1_mid               EE_AP_MID                 1_GND                     {1.25e-07}

************************************************** APERTURE 2 ************************************
****** Group 1 ******
V_tap_2_1                 EE_AP_MID                 EE002                     {0}
L_2_1                     EE002                     EE003                     {L_2_1_value}

****** Group 2 ******
V_tap_2_2                 EE003                     EE004                     {0}
L_2_2                     EE004                     EE005                     {L_2_2_value}

****** Group 3 ******
V_tap_2_3                 EE005                     EE006                     {0}
L_2_3                     EE006                     EE007                     {L_2_3_value}

****** Group 4 ******
V_tap_2_4                 EE007                     EE008                     {0}
L_2_4                     EE008                     EE009                     {L_2_4_value}

**************************************************************************************************
* Fake voltage source to easily access the output current
V_ap_2                    EE021                     EE_AP2_OUT                {0}
C_GND_out                 EE_AP2_OUT                1_GND                     {6.25e-08}
```

Figure 3.17: Example of the magnet circuit generated for the MBRD by assigning all the turns of the first aperture to group 11 and by splitting the turns of the second aperture into four different groups.

element parameters of the coupling loops are typically dependent on the geometry of the domain in which these losses are produced or on the cable parameters, it is possible to make the approximation that effects with similar equivalent parameters can be summed together and represented by the same loop [10]. Accordingly, depending on the characteristics of the magnet, the TFM tool generates an accurate number of subcircuits to represent the contribution of each strand in each turn.

For instance, the MBRD cables are constructed from the same conductor, indicating that all strands possess identical geometry. Consequently, if the "turns_to_conductor" key is empty, each coupling effect is divided into a single subcircuit per aperture and is coupled to the corresponding subcircuit of the magnet circuit and the corresponding subcircuits of all the other coupling loops. In the case of the LHC Main Dipole, which is made of two different conductors with different geometries, two subcircuits are created for each effect in each aperture even if the "turns_to_conductor" is empty, in order to account for the different equivalent parameters.

Each conductor loss loop comprises an inductance, a voltage tap, and a resistance to ground, in addition to persistent currents with different types of equivalent parameters. These loops are also characterised by a coupling coefficient, in Figure 3.18 $K_{\mathrm{ISCC},1,1}$, which is calculated as follows:

$$K_{\mathrm{eff}} = \frac{M_{\mathrm{eff}}}{\sqrt{L_{\mathrm{eff}} * L_{\mathrm{mag}}}} \tag{3.5}$$

where L_{eff} [H] is the inductance corresponding to that specific loop, L_{mag} [H] is the inductance of the corresponding loop in the magnet circuit and M_{eff} [H] is the mutual inductance between the two loops. The coupling coefficient, which ranges between -1 and 1, indicates the strength of the magnetic coupling between the two circuits.

The values for resistance, inductance, and mutual inductance are stored in the library file as tabular data. If the flag corresponding to a specific effect is set to True, the TFM tool populates its parameters tables with the appropriate values for each frequency being simulated. Furthermore, each effect is coupled to all other loops of other effects within the same aperture. The first number in the suffix of a parameter name denotes the aperture number, while the second number indicates the section number.

The sole conductor effect which slightly differs from Figure 3.18 is the persistent current. Indeed for this effect, an ideal current source substitutes the voltage source and resistance in the loop.

Coupling loops of metallic elements To represent the eddy current losses in each metallic component, a network circuit similar to the one shown in Figure 3.18 is generated. However, since the power loss and induced currents for these effects are not calculated analytically but are instead simulated in COMSOL Multiphysics®, there is no need to divide the turns based on their cable geometry. The models already account for the materials and geometry of the various components. The time constants for all effects are calculated within the TFM tool using the power loss components and show excellent agreement with the COMSOL Multiphysics® simulations, as demonstrated in Table 3.2.

The library generation is accurate in order to comprehend all the different types of effects that could influence the magnet behaviour, and allows multiple modalities to be employed in order to simulate different parts of the magnet. It is also important to emphasize that the incorporation of a new data class for a new effect is possible without modifying the library generation code, thus enhancing the simplicity and reproducibility of the TFM model. Once

Table 3.2: Time constant comparison between the TFM tool calculation and the COMSOL Multiphysics® simulations for each metallic effect [10].

	TFM calculation	**COMSOL Multiphysics® simulations**
Wedges	0.02982 s	0.02882 s
Cold-Bores	0.112 ms	0.124 ms
Coil Protection Sheets	0.448 ms	0.427 ms
Aluminum Ring (rho = 3.83 E-07)	0.007689 s	0.0098 s
Aluminum Ring (rho = 6.56 E-07)	0.006078 s	0.0057 s

the network has been constructed and is complete, the next step is to read the desired voltage across the sections of the magnet that are to be simulated and calculate the impedance using Equation 2.19

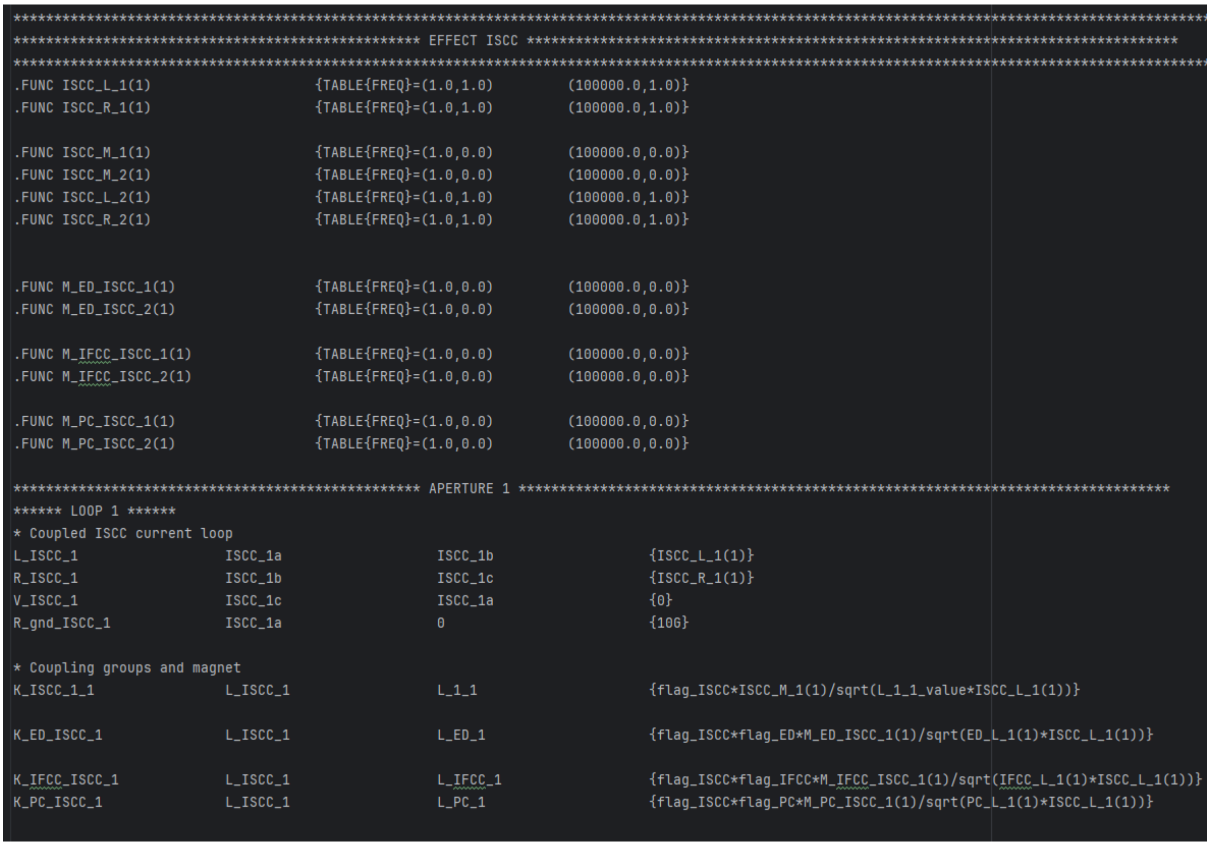

```
*****************************************************************************************************************************************************
*************************************************** EFFECT ISCC *********************************************************************************
*****************************************************************************************************************************************************
.FUNC ISCC_L_1(1)                    {TABLE{FREQ}=(1.0,1.0)         (100000.0,1.0)}
.FUNC ISCC_R_1(1)                    {TABLE{FREQ}=(1.0,1.0)         (100000.0,1.0)}

.FUNC ISCC_M_1(1)                    {TABLE{FREQ}=(1.0,0.0)         (100000.0,0.0)}
.FUNC ISCC_M_2(1)                    {TABLE{FREQ}=(1.0,0.0)         (100000.0,0.0)}
.FUNC ISCC_L_2(1)                    {TABLE{FREQ}=(1.0,1.0)         (100000.0,1.0)}
.FUNC ISCC_R_2(1)                    {TABLE{FREQ}=(1.0,1.0)         (100000.0,1.0)}


.FUNC M_ED_ISCC_1(1)                 {TABLE{FREQ}=(1.0,0.0)         (100000.0,0.0)}
.FUNC M_ED_ISCC_2(1)                 {TABLE{FREQ}=(1.0,0.0)         (100000.0,0.0)}

.FUNC M_IFCC_ISCC_1(1)               {TABLE{FREQ}=(1.0,0.0)         (100000.0,0.0)}
.FUNC M_IFCC_ISCC_2(1)               {TABLE{FREQ}=(1.0,0.0)         (100000.0,0.0)}

.FUNC M_PC_ISCC_1(1)                 {TABLE{FREQ}=(1.0,0.0)         (100000.0,0.0)}
.FUNC M_PC_ISCC_2(1)                 {TABLE{FREQ}=(1.0,0.0)         (100000.0,0.0)}

*************************************************** APERTURE 1 *********************************************************************************
****** LOOP 1 ******
* Coupled ISCC current loop
L_ISCC_1                  ISCC_1a                    ISCC_1b                    {ISCC_L_1(1)}
R_ISCC_1                  ISCC_1b                    ISCC_1c                    {ISCC_R_1(1)}
V_ISCC_1                  ISCC_1c                    ISCC_1a                    {0}
R_gnd_ISCC_1              ISCC_1a                    0                          {10G}

* Coupling groups and magnet
K_ISCC_1_1                L_ISCC_1                   L_1_1                      {flag_ISCC*ISCC_M_1(1)/sqrt(L_1_1_value*ISCC_L_1(1))}

K_ED_ISCC_1               L_ISCC_1                   L_ED_1                     {flag_ISCC*flag_ED*M_ED_ISCC_1(1)/sqrt(ED_L_1(1)*ISCC_L_1(1))}

K_IFCC_ISCC_1             L_ISCC_1                   L_IFCC_1                   {flag_ISCC*flag_IFCC*M_IFCC_ISCC_1(1)/sqrt(IFCC_L_1(1)*ISCC_L_1(1))}
K_PC_ISCC_1               L_ISCC_1                   L_PC_1                     {flag_ISCC*flag_PC*M_PC_ISCC_1(1)/sqrt(PC_L_1(1)*ISCC_L_1(1))}
```

Figure 3.18: Example of the ISCC coupling loop generated for the first aperture in a MBRD impedance simulation.

Validation of the Model with experimental Magnets Data

After developing the COMSOL Multiphysics ® models and the TFM tool, it was essential to validate the simulation model. This was achieved by comparing the simulation results with impedance measurements of both the full magnet and the individual aperture from SM18. The goal of this validation was to ensure that the simulation accurately reflected the actual behavior of the magnet, thereby enabling accurate predictions of the magnet's performance in various scenarios. The validation process began by comparing the simulation results with measured data for the magnet without externally applied short circuits. Once the accuracy was confirmed in this simpler case, the process moved on to validate the simulation under the more complex conditions involving short-circuits.

The following sections will begin by presenting a detailed comparison between the modulus and phase of the MBRD complex impedance, as obtained from simulations using the TFM tool, and the corresponding measurements. Subsequently, the simulation will be broken down to examine the contributions of various coupling effects on the impedance. This analysis will also explore the impact of the value of key parameters of the magnet components and assess the significance of mutual coupling between effects.

4.1 Validation of the Simulated Impedance

Figure 4.1 shows that there is a good agreement between the simulated and measured impedance modulus of the MBRD in its superconducting state under normal conditions. Specifically, the relative error between the measured and simulated impedance modulus remains within 12 % up to a frequency of 10 kHz. The maximum relative error is observed in regions where the impedance slope undergoes significant changes in a low-frequency range, which can be particularly challenging to reproduce using a simplified model. The agreement is particularly precise for the impedance of a single magnet aperture, Z_{Ap1} [Ω], where the average error is 3.39 % up to 10 kHz. For the full magnet, the average error in the impedance modulus Z_{Full} [Ω] is instead 7.89 %. Nevertheless, at frequencies exceeding the resonance peak, a notable divergence emerges between the simulated and measured data, with the relative error exceeding 20 %. This discrepancy arises because the tool struggles to accurately estimate the capacitance contributions. Lumping the capacitances into multiple components in the network model is indeed a challenging task. As a result, in the network model generated by the tool just three capacitances are inserted: one at the beginning, one in the middle between the two apertures, and one at the end of the circuit. This simplification allows to achieve a good agreement up to 10 kHz, which is the frequency range of interest.

Overall, the simulation results successfully match the modulus of the complex impedance measured from the SM18 across a broad frequency range of 1 Hz to 10 kHz. This range includes the frequencies where coupling effects most strongly affect the magnet's behavior,

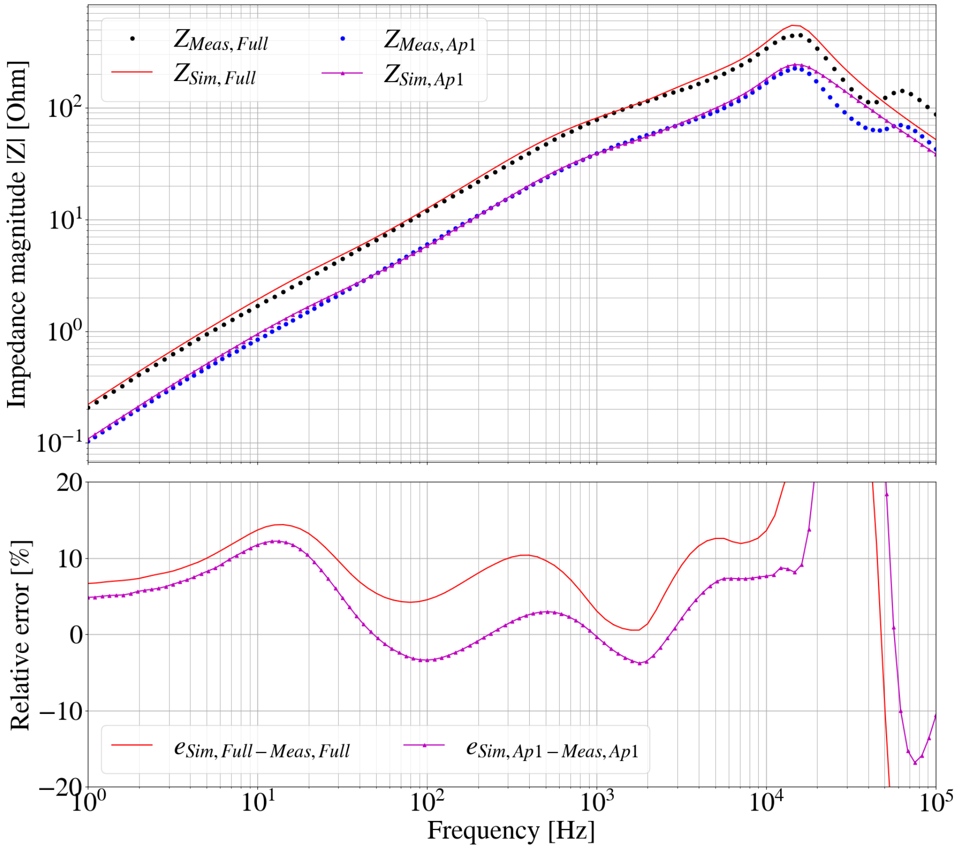

Figure 4.1: Simulation and measurement of the MBRD impedance modulus including all coupling losses for the single aperture and full and full magnet configurations, and their relative error.

giving a clear picture of how different factors influence the magnet's impedance.
To further validate the complex impedance, the phase of the magnet's impedance was simulated and compared with the measured data, as shown in Figure 4.2.
In this context, a phase of 90 ° indicates purely inductive behavior, while a phase close to 0 ° signifies resistive behavior, and a phase near -90 ° represents purely capacitive behavior. The figure shows that the measured phase curves for a single aperture and the full magnet are nearly identical. The simulated phase does not match the measurements as closely as the impedance modulus, exhibiting a significant absolute error, especially between 1 kHz and 10 kHz. Within this frequency range, the simulated phase is closer to 0 ° than the measured phase, suggesting an overestimation of resistive effects in the coupling loops. Additionally, the measured phase undergoes a complete sign reversal within this range, indicating a sharp transition that is likely challenging to model accurately with a simplified model.

4.2 Coupling Current Effects on Impedance

The various coupling currents within the magnet's components generate losses that significantly shape the magnet's overall behavior, which is clearly reflected in the impedance curve. Each type of coupling current has a distinct impact on the curve, with its influence

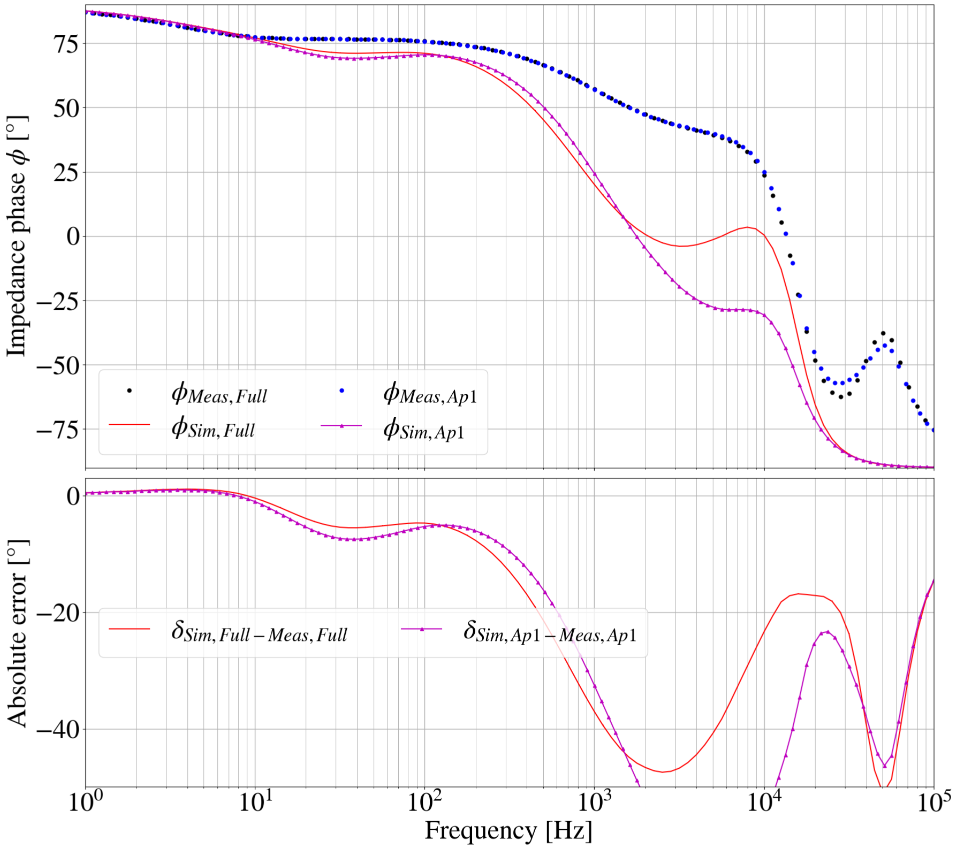

Figure 4.2: Simulation and measurement of the MBRD impedance phase including all coupling losses for the single aperture and full and full magnet configurations, and their absolute error.

varying in intensity across different parts of the frequency spectrum. These losses have their most significant impact near the frequencies corresponding to the inverse of their respective time constants, leading to more pronounced deviations from the magnet's ideal impedance at those points.

In Figure 4.3, the impact of each type of current-induced loss on the impedance curve is depicted. The effects which contribute to the cumulative conductor losses are combined and plotted as Z_{CL} [Ω]. This includes the persistent currents, inter-filament coupling currents, inter-strand coupling currents, and eddy currents in the copper sheaths.

These losses usually are noticeable at lower frequencies, but in the case of the MBRD magnet their impact on the impedance curve is minimal. This outcome aligns with the effect of the conductor losses in the outer cable of the LHC main dipole, which is the same type used for the MBRD [10].

Beyond the conductor losses, other factors also come into play. Eddy currents in the wedges contribute to the impedance at low frequencies, followed then by the aluminum ring, which has a significant impact between 20 Hz and 1 kHz, and the coil protection sheets, which are mainly observable between 500 Hz and 2 kHz. Finally, the cold bores become relevant around the resonance peak.

Although these effects play a significant role in shaping the impedance, the simulated curves including their contribution remain relatively distant from the measurement data. This leads

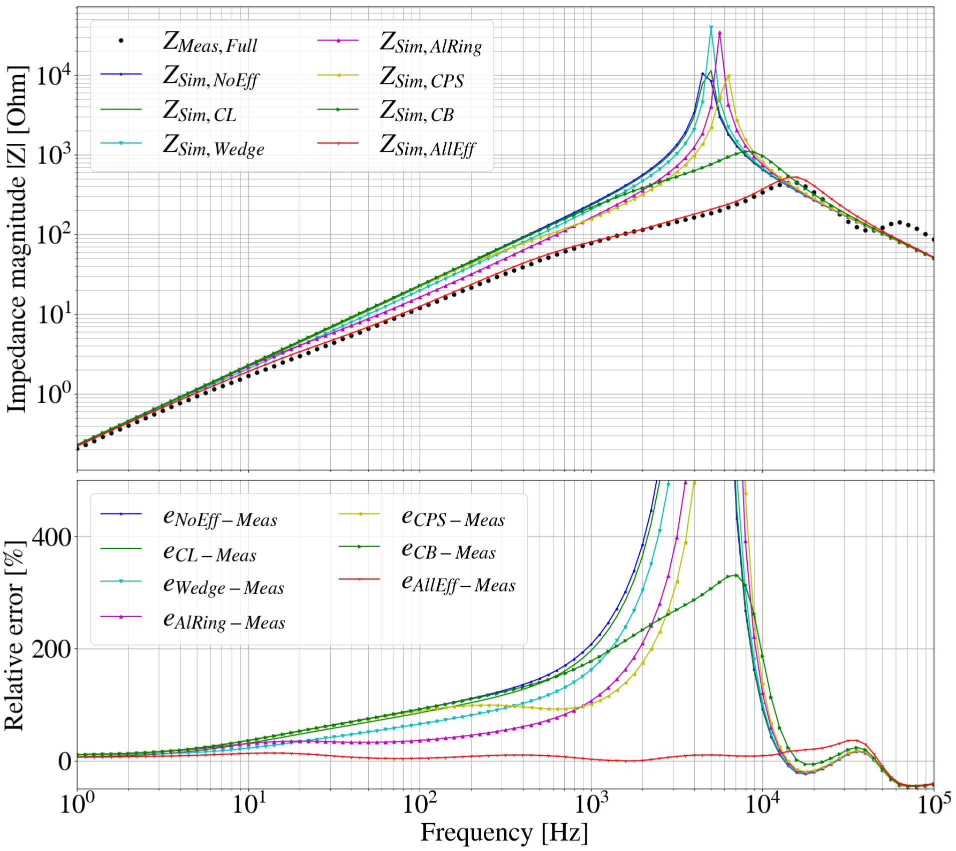

Figure 4.3: Simulation of the MBRD Impedance showcasing the contribution of the different coupling losses. Z_{all} [Ω] is the only simulated impedance that includes the mutual coupling between different effects.

to considerable relative errors, particularly near the resonance peak frequency. The mutual couplings between the various loops, included in the combined impedance Z_{all} [Ω], bring all these effects together and allow to achieve the excellent fit observed in the results.

An alternative method for closely examining the contribution of various effects is to compare their differential inductance, defined as:

$$L_{\mathrm{D}} = \frac{\mathrm{Im(Z)} \times e^{i \cdot \phi}}{\omega} \quad [H] \tag{4.1}$$

where Z [Ω] is the imaginary part of the impedance, ϕ [rad] is the phase of the impedance and ω is the angular frequency. Figure 4.4 shows that the differential inductance due to the persistent currents, which don't have a time constant, deviates immediately from the nominal value. In contrast, all the differential inductances associated with the other effects start to deviate only when the frequency reaches the value corresponding to their respective time constants. As can be observed, the eddy currents in the cold bore and aluminum ring have the most significant impact on the magnet's inductance. Additionally, conductor losses primarily affect the low frequency regime, while eddy currents in the metallic components affect the high frequency regimes. The differential inductance with all the effects is again the only one that includes the mutual couplings between the loops.

The same observation can be done by analyzing the dissipated power due to the various

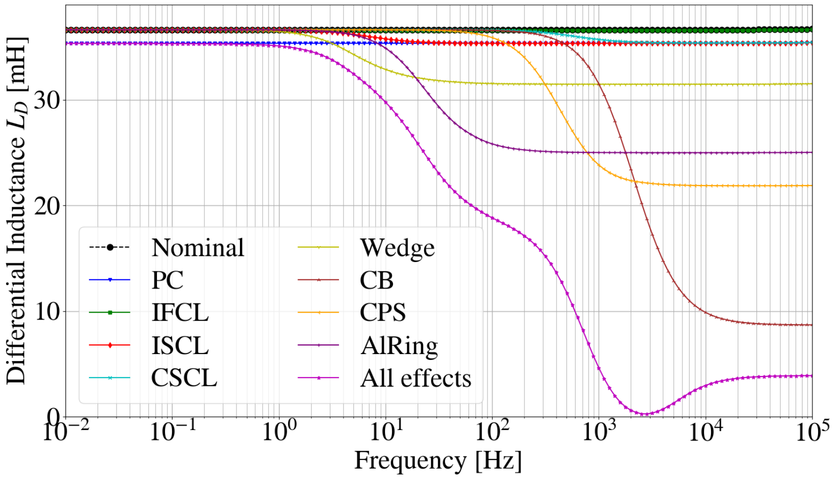

Figure 4.4: Simulation of the Differential Inductance for the MBRD full magnet configuration. The curve marked as "All effects" is the only simulation that accounts for the mutual coupling between different effects

losses, which is depicted in Figure 4.5, and can be found as [10]:

$$P = \frac{1}{2}\Re\{\mathbf{U}_R \bar{\mathbf{I}}_{Loop}\} \quad [W] \tag{4.2}$$

where $\mathbf{U}_R$ [V] is the voltage across the resistance in the corresponding equivalent loop and $\bar{\mathbf{I}}_{Loop}$ [A] is the complex conjugate of the current flowing in the loop.

For frequencies up to 2 kHz, the dominant contributors to the dissipated power are the inter-filament and inter-strand interactions, together with the wedge and aluminum ring. As the frequency increases, the influence of these contributions diminishes, while the effects associated with eddy currents become more pronounced, resulting in greater power dissipation at higher frequencies.

In this plot, all the curves account for coupling with each other, which could explain the abrupt changes in some of the power loss curves, likely due to other coupling effects. This again highlights the importance of an accurate evaluation of the mutual coupling values to obtain a reliable model and accurate results.

4.3 Mutual Coupling contribution

A significant challenge in this validation process was to account for the interactions between the various conductor loss loops. When a coupling current flows through a section of the superconducting magnet, it generates a magnetic field that affects the overall magnetic environment, thereby also influencing the strength of the other coupling effects. It was therefore essential to accurately determine these mutual couplings in the model in order to achieve reliable impedance simulation results.

The correlation between conductor losses and metallic components can be quantified using standard analytical equations and magnetic coefficients derived from the magnetic field data

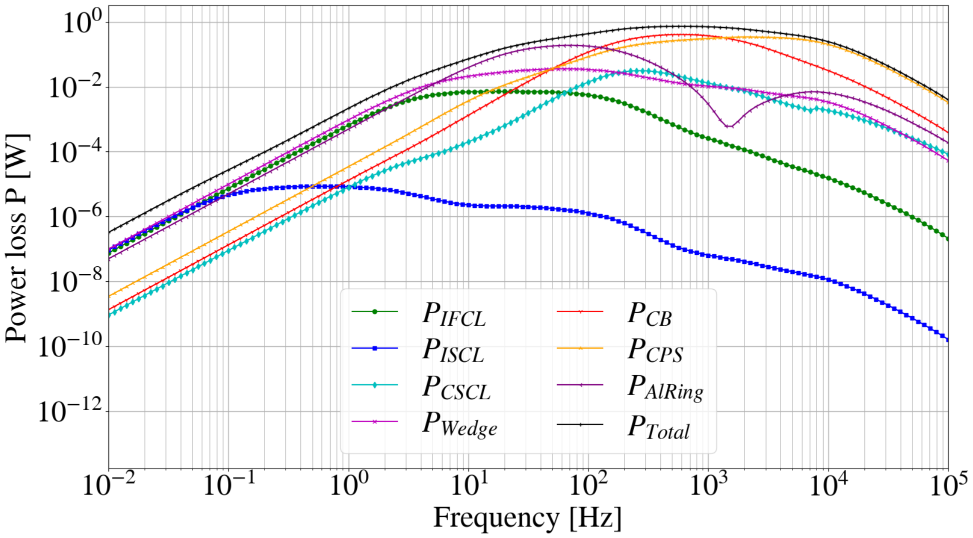

Figure 4.5: Simulation of the MBRD Power Losses for the MBRD full magnet simulation

extracted from each COMSOL Multiphysics ® model. However, an alternative methodology was required to evaluate the coupling between the loops representing eddy currents in the various metallic components. In order to achieve this, new FEM models were developed for each pair of metallic elements. In these models, rather than introducing a current into the coils, a current I_1 [A] was induced into one of the metallic components. Subsequently, a frequency simulation was conducted to determine the induced current I_2 [A] in the other metallic components. This approach provided an initial estimate for the mutual couplings using the formula:

$$M_{1,2} = \frac{j\omega I_2 L_2 + I_2 R_2}{j\omega I_1}\ [H] \tag{4.3}$$

where L_2 [H] is the inductance of the loop representing eddy currents in the second component and R_2 [Ω] is the corresponding resistance.

After obtaining initial estimates for each mutual inductance combination, an optimization script was run to fine-tune these values, ensuring they closely matched the measurements. The final values, as shown in Table 4.1, were then used in the simulations. As can be observed, the main difference between the two configurations lies in the couplings involving

Table 4.1: Mutual coupling between the magnet component loops, found in simulations of both the full magnet configuration and the single-aperture setup.

Mutual Coupling	**Full Magnet**	**1 Aperture**
$M_{CB,Wedge}$	1.713e-08 H	1.713e-08 H
$M_{CPS,Wedge}$	-7.169e-07 H	-7.169e-07 H
$M_{CPS,CB}$	5.080e-06 H	5.080e-06 H
$M_{AlRing,Wedge}$	2.1644e-08 H	4.225e-08 H
$M_{AlRing,CB}$	-2.324e-06 H	-5.515e-07 H
$M_{AlRing,CPS}$	1.367e-05 H	1.479e-05 H

the aluminum ring. The aluminum ring is the only metallic component that covers both apertures, significantly influencing the magnetic interactions. Because the eddy currents circulate throughout the entire ring, the magnetic field generated by these currents is not localized around each aperture, as in other effects. Instead, it has a different distribution, which could lead to an asymmetrical magnetic field due to the mutual interaction between the two apertures. Consequently, it is reasonable to believe that the aluminum ring's influence on other effects also differs between the two configurations.

In Figure 4.6, the modulus of the complex magnetic impedance is simulated for different types of mutual coupling included. In particular, the following definitions apply:

- M_{Metallic}: represents simulations that consider only the mutual coupling between loops of eddy currents in metallic components.
- M_{CL}: includes only the mutual coupling effects between loops related to conductor losses.
- M_{Metallic}: considers only the mutual coupling between loops of eddy currents in metallic components.
- $M_{\text{NoMetallic}}$ and M_{NoCL}: both accounts for the mutual coupling effects between the loops of metallic components and the conductor losses. However, the first one includes also the coupling between the conductor losses, while the second includes also the coupling between the metallic components.
- M_{All}: incorporates all types of mutual coupling.
- M_{None}: does not account for any kind of mutual coupling.

The results demonstrate that the simulation accounting solely for mutual coupling between conductor losses yield results identical to those with no mutual coupling. This suggests that the impact of conductor loss coupling is negligible. This is further supported by the fact that the curve for M_{NoCL} perfectly aligns with M_{all}. Furthermore, simulations that consider only mutual coupling between metallic components also match perfectly with the one including all mutual couplings. This indicates that the coupling between metallic components is the primary effect, with only the coupling between metallic components and conductor losses playing a minor role. This predominance can be attributed to the fact that losses in metallic components are substantially greater than those in conductor losses, resulting in stronger interactions among the metallic components, especially when their current time constants are close. Without the mutual coupling between these effects, the impedance curve results significantly deformed in comparison to its measured value.

4.4 Parametric Sweep Study

To advance the validation of the MBRD model, the values of certain parameters were investigated, as their values significantly impacts measurement accuracy. Specifically, a study was carried out to identify the optimal parameters for the resistivity of the aluminum ring, the RRR of the wedges, and the resistivity of the coil protection sheets. Multiple simulations were performed for each parameter, taking into account all contributing effects and the mutual coupling between the loops, while varying only the parameter in question. The results were

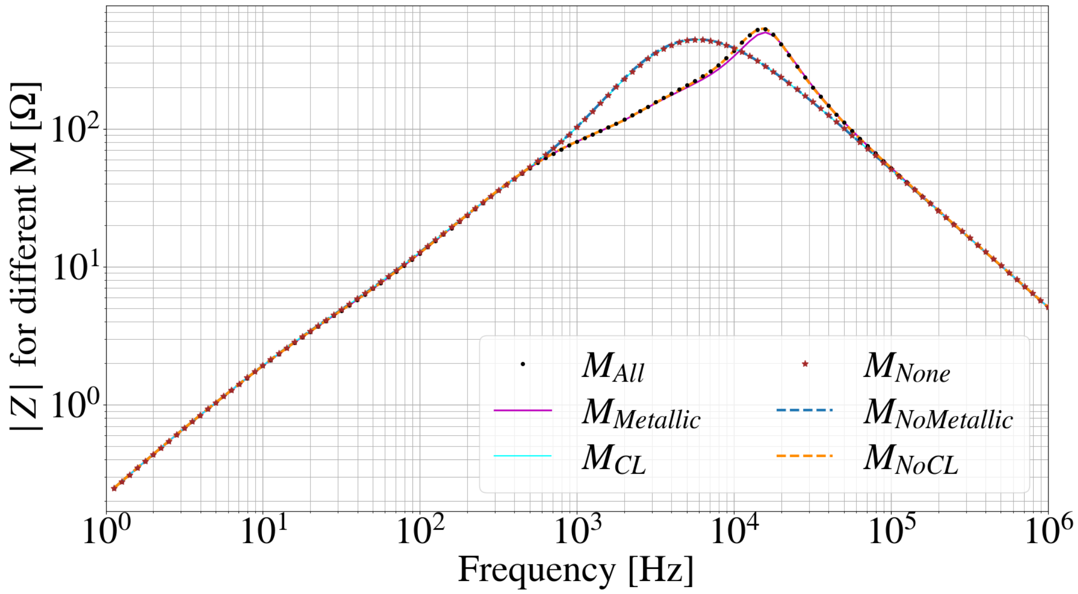

Figure 4.6: MBRD full magnet simulation showing the impedance modulus of the magnet with different mutual coupling included.

then visualised using a colour map to highlight the contribution of each parameter and their trends in the measurement curve based on their values.

4.4.1 RRR of the Wedges

The eddy currents in the wedges have a pronounced effect on the impedance simulation, particularly at lower frequencies up to about 10 Hz. The RRR is a critical parameter in the equivalent parameter simulation, as shown in Figure 3.10. Variations in RRR lead to significant changes in the power loss and induced current curves, which are essential for calculating equivalent parameters.
To investigate this effect, 190 different RRR values ranging from 10 to 200 were simulated, as shown in Figure 4.7. The results show that changes in RRR values primarily affect the shape of the impedance curve around the resonance peak. This variation is likely to be due to changes in the time constant associated with the RRR, which significantly alters the shape of the curve. An incorrect time constant can cause the impedance curve to deviate from the measured data by assuming an inaccurately rounded shape. For very low and too high RRR values the simulation results deviated significantly from the impedance curve. Ultimately, an optimum RRR range of 90 - 150 was determined, with a final value of 140 used in the simulation.

4.4.2 Resistivity of the Aluminum Ring

The aluminum ring proved to have a significant effect on the impedance simulation, because of its higher resistivity and significantly larger dimensions compared to those of the other metallic components studied. Its contribution makes the simulation achieve excellent agreement with measurements over the entire frequency range from 20 Hz to 1 kHz, with its resistivity playing a crucial role in achieving this fit.

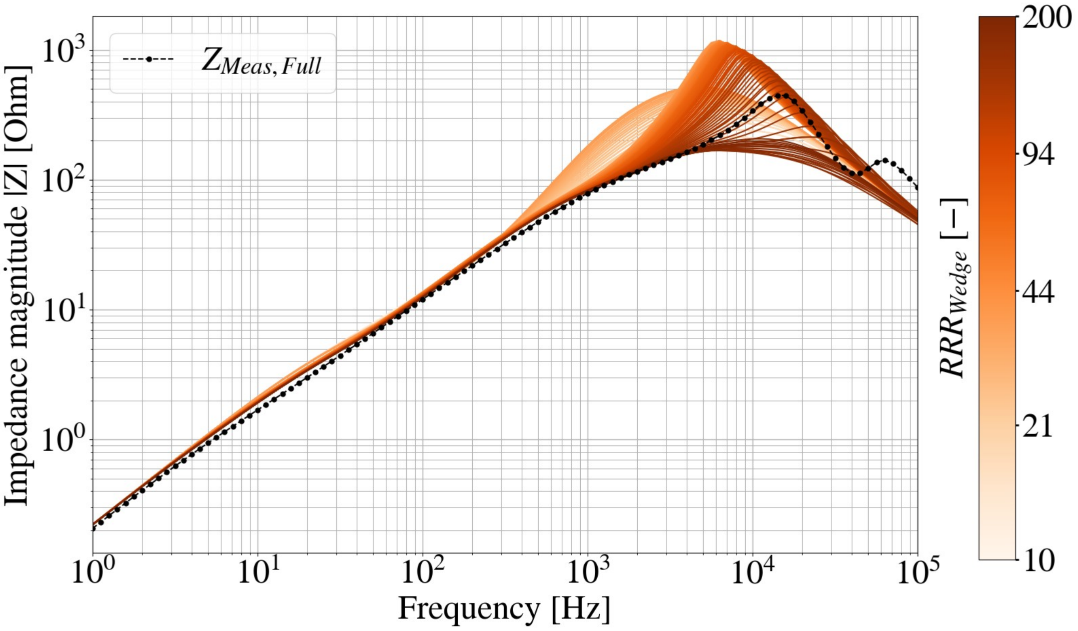

Figure 4.7: MBRD full magnet simulation showing the different impedance for 190 value of RRR of the wedges, in the range 10-200.

To determine the optimal resistivity value, a parametric sweep was performed using 400 logarithmically spaced correction factor values for the aluminum resistivity, making it range from 10^{-9} Ω·m to 10^{-6} Ω·m, in Figure 4.8. This analysis showed that at very low resistivity values, around 10^{-9} Ω·m, the impedance curve has a rounded shape that deviates significantly from the measured curve, indicating a poor fit. For resistivity values between 10^{-8} Ω·m and 10^{-7} Ω·m, while the curves still shows discrepancies, the simulations begin to follow the measurement trend more closely, but in the range from 10 Hz to 100 Hz, they show a bump that makes them deviate from the measurements. Finally, for resistance values between 10^{-7} Ω·m and 10^{-6} Ω·m, the simulated impedance curves began to closely follow the measured curve, maintaining the correct shape of the impedance. This fit suggests that the time constant values were accurately represented. The best fitting parameter was found to be a resistivity of 5.25×10^{-7} Ω·m.

Comparing this value with the power loss and induced current plots shown in Figure 3.13, it is clear that the final resistivity value is associated with a smaller time constant, which increases the effect at higher frequencies. It is also important to note that the initial resistivity estimate derived from Equation 3.4 was 6.084×10^{-9} Ω·m. The final, optimized resistivity value of 5.25×10^{-7} Ω·m shows a significant discrepancy from this initial estimate found with Equation 3.4. Specifically, the absolute error between the initial and final values is 4.94×10^{-7} Ω·m, which indicates a significant deviation from the true resistivity value.

This substantial discrepancy can be attributed to the complex three-dimensional effects inherent to the laminated rings, which are challenging to accurately represent in a two-dimensional model. Beyond the variations in current paths and the resulting differences in conductivity, other factors also contribute to this issue.

Specifically, the aluminum ring, which spans both apertures, introduces deviations in the magnetic field distribution around them. This can result in inconsistencies in how the effect

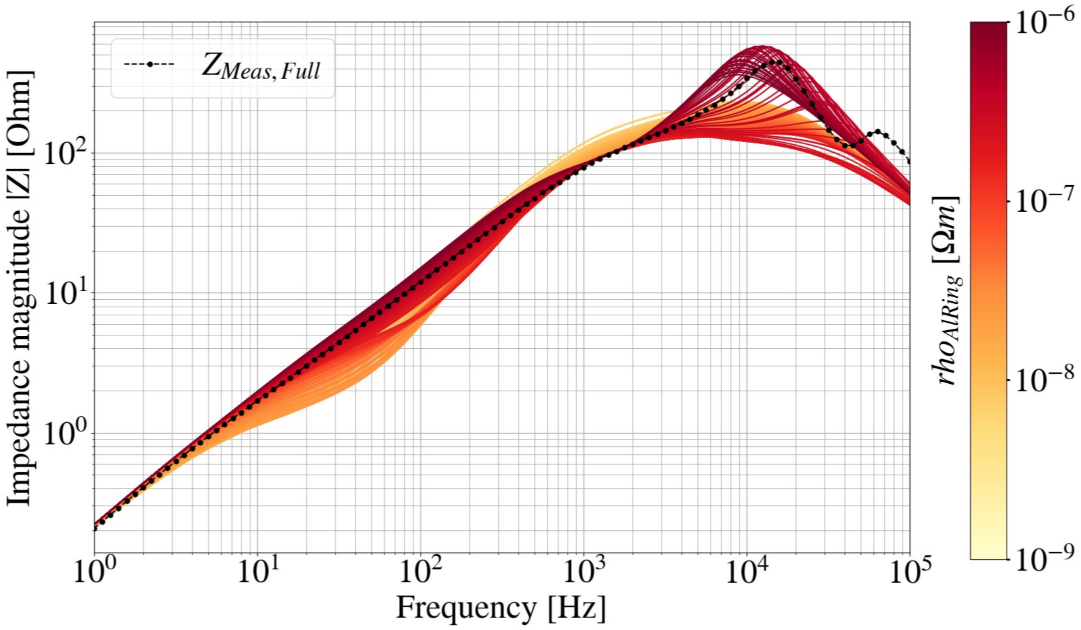

Figure 4.8: MBRD full magnet simulation showing the different impedance for 400 values of the Aluminum ring resistivity, in the range between 10^{-6} Ω·m and 10^{-9} Ω·m

of the eddy currents in the aluminum ring is represented in the network model. Typically, each aperture is represented by its own circuit, with the two circuits interacting through mutual coupling. However, in this case, the interaction between the two circuits may be too strong to be accurately captured by this approach.

Furthermore, an increase in the resistivity of the aluminum ring could assist in the mitigation of the impact of the end effects observed between the structure enclosed by the ring and the surrounding collars or other magnet components. These end effects are frequently associated with fluctuations in the magnetic field in the vicinity of the structure's edges, where the magnetic flux tends to fringe and distort. The surrounding components can create capacitive effects with the ground, modifying the current paths and potentially resulting in anomalies. By modifying the resistivity, these disruptive influences on the magnetic field and current distribution may be taken into account, leading to a more accurate representation of the measured impedance curve of the superconducting magnet.

4.4.3 Resistivity of the Coil Protection Sheets

The eddy currents flowing through the coil protection sheets exert a considerable influence on the impedance curve. This effect arises from the larger loop that is available for the current to flow through. Although the sheets are divided into blocks with small separations around the mid-plane, the sheets remain relatively close to each other. As a result, within each aperture, the eddy currents are able to circulate around the entire circumference, resulting in considerably higher losses in comparison to those observed in the wedges, which are electrically insulated from one another.

It is noteworthy that this influence is particularly pronounced between 2 kHz and 10 kHz, as illustrated in Figure 4.9. Small variations in the resistivity of stainless steel, due to manufacturing defects or material impurities, can lead to significant changes in the time constant

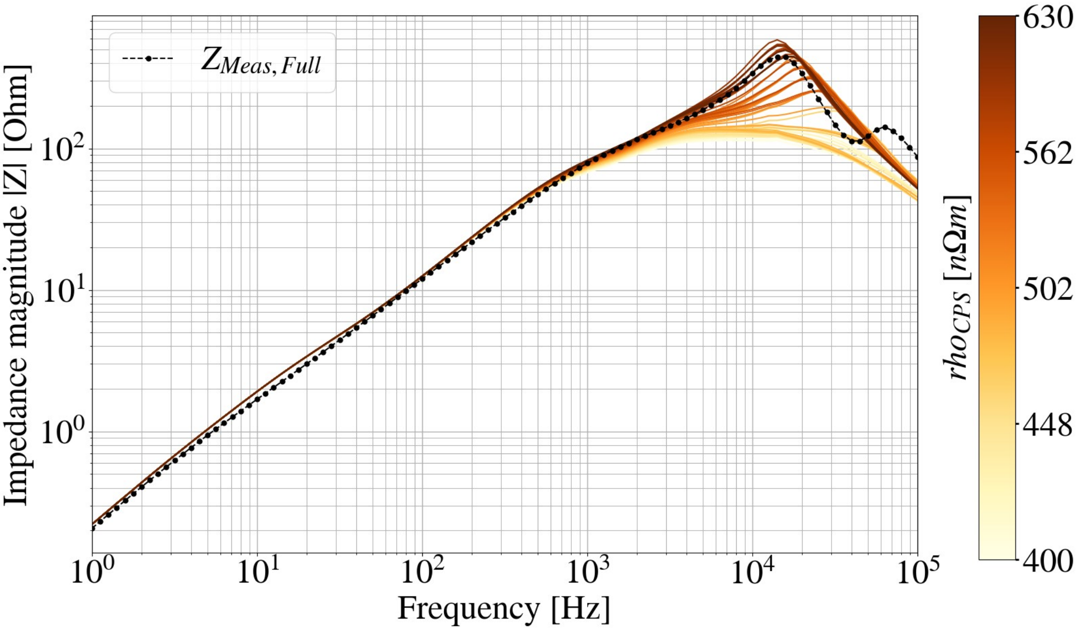

Figure 4.9: MBRD full magnet simulation showing the different impedance for 100 values of the coil protection sheets resistivity, in the range between 400 nΩ·m and 630 nΩ·m

associated with the eddy currents, thereby affecting the impedance curve.

To address this issue, impedance simulations were performed over 100 different resistivity values for stainless steel at 1.9 K, with a reference value of 500 nΩ·m. The aim was to find the resistivity value that best matched the measured impedance. As can be seen in Figure 4.9, for resistivity values between 400 nΩ·m and 500 nΩ·m, the simulated impedance deviates significantly from the measured values. This discrepancy is due to the time constants being too high, resulting in an inaccurate impedance curve. However, when examining the resistivity values between 550 nΩ·m and 630 nΩ·m, the simulated impedance is more in line with the measured data, especially near the resonance peak. The most optimized value for this resistivity was found to be 600 nΩ·m, which yielded the best match between the simulation and the measurement curves.

Simulation of Failures and Analyses

The integrity and safety of the operation of superconducting magnets are crucial for ensuring the accurate reproducibility of physical phenomena in the collider. However, various non-conformities emerge during their operation, posing significant risks.
One of the most significant concerns is the potential for short circuits, particularly within the coil-winding pack [59]. Inter-turn shorts can occur during quenches, due to the generated heat and mechanical stress, which can potentially damage the insulation. Similarly, the fast ramping of the magnet excitation current can result in the generation of significant electromagnetic forces, which may potentially lead to insulation breakdown and subsequent short circuits.
The occurrence of a short circuit creates an alternative path for the current, which in turn gives rise to anomalies in the magnet's electrical behavior. This has the potential to compromise the precision required for the operation of the LHC. Furthermore, the current flowing through this resistive path can also result in localized heating, which may have an additional negative impact on the magnet's performance.
The accurate localization of a short circuit represents a significant challenge, primarily due to the low resistance associated with such faults, rendering conventional resistive methods ineffective. Nevertheless, measuring complex impedance as a function of frequency represents a promising alternative. This approach has been successfully applied in several contexts [59], such as fusion stellarators [60] [61], in CICC model coils [62], and for monitoring and controlling the resin impregnation process in Nb3Sn coils [63].
In light of the proven efficacy of complex impedance measurements in identifying short circuits within superconducting magnets, the TFM tool's functionality has been extended to simulate these faults. Following initial validation for normal conditions, the tool has been developed to include the capability to model short circuits, thereby providing a reference against which the simulations of non-conformities could be compared and evaluated. This functionality will facilitate the diagnosis of potential precursors to failures that could impact LHC operations.
This chapter will firstly present the theoretical basis for the short-circuit application to the network model [59]. It will then provide a brief overview of the methodology used to integrate this feature into the tool. Subsequently, the simulation results involving short circuits will be validated against measurements from SM18. Finally, the chapter will analyze the impact of short circuits on magnet impedance behavior, exploring a variety of scenarios, including shorted turns in different locations within the magnet coils and the effects of varying the value of the applied short resistance.

5.1 Analytical Impact of Short Circuit on the Network Model

In the network model, each turn of the magnet can be represented by an inductance element connected in series with the others. The impact of a short circuit across a turn within

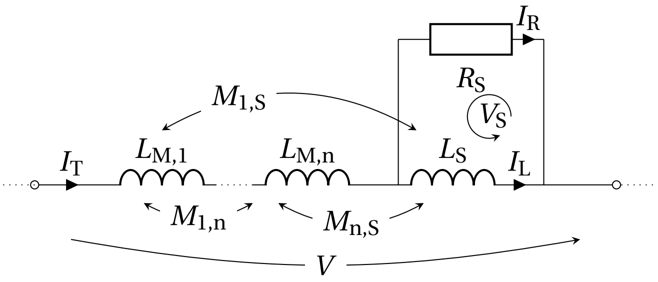

Figure 5.1: Simplified schematic of n inductances in series of which one inductance L_S is shorted by a parallel resistance [59]

this model influences the magnet's behaviour, even in the absence of coupling loops.

As illustrated in Figure 5.1, three inductances, representing distinct magnet turns, are connected in series and coupled by mutual inductances. The same current, I_T [A], flows through all three inductances. Should a short circuit with resistance R_S [Ω] occur across one of these inductances, L_S [H], the current distribution within the circuit will undergo a change. This is due to the fact that the short circuit provides an alternative path for the current, which results in current-sharing. The original current, I_T, is then divided into two components: the first one, I_L [A] continues to flow through the shorted turn, while the remaining current, I_R [A], flows through the short-circuit resistance [59]. By calculating the voltage and current relationships in the circuit, the total impedance can be determined as the ratio of the voltage across the circuit to the current flowing through it [59]:

$$Z(s) = \frac{V}{I_T} = Z_1\left(Z_2 + Z_3 + Z_4\right) \tag{5.1}$$

where the different block can be found as [59]:

$$\begin{aligned}
Z_1 &= \frac{s}{sL_S - R_S} \\
Z_2 &= -sL_S \sum_{i=1}^{n} L_{M,i} + s \sum_{i=1}^{n} M_{i,S}^2 \\
Z_3 &= R_S \left[\sum_{i=1}^{n} L_{M,i} + L_S + 2 \sum_{i=1}^{n} \left(\sum_{j=i}^{n} (M_{i,j}) + M_{i,S} \right) \right] \\
Z_4 &= -2sL_S \sum_{i=1}^{n} \sum_{j=i}^{n} M_{i,j} + 2s \prod_{i=1}^{n} \prod_{j=1}^{i} M_{i,S} M_{j,S}
\end{aligned} \tag{5.2}$$

By combining the equations in Equation 5.1 and Equation 5.2, it is evident that the resulting impedance significantly varies depending on the resistance values.Specifically, when the short resistance is extremely high, the impedance is reduced to only the inductance contribution, as if the short resistance were absent. This allows the final equation to be simplified as follows [59]:

$$\lim_{R_S \to \infty} Z(s) = \frac{s}{R_S} Z_3 = s\left[\sum L + 2\sum M\right] \tag{5.3}$$

Conversely, as the resistance value decreases and approaches zero the equation simplifies to [59]:

$$\lim_{R_S \to 0} Z(s) = \frac{1}{L_S}(Z_2 + Z_4) \tag{5.4}$$

where at very low impedance values, the effect is primarily determined by the mutual coupling of the turns with their neighboring turns.

As a result, the relative error between the reference impedance and the impedance with shorts is predominantly influenced by the mutual coupling between the magnet's turns. The inductance matrix is a useful tool to capture the inductive interactions within the system and therefore the effect of different short on the impedance curve.

The inductance matrix is organized such that the self-inductance of each turn is located along the diagonal, while the off-diagonal elements represent the mutual inductance between different turns. As illustrated in Figure 5.3, the self-inductance values of each turn, which range from 1.0 mH to 1.4 mH, are significantly greater than the mutual inductance values, which span from 0 to 1 mH. The matrix also reveals a systematic decrease in self-inductance values from the top to the bottom. This trend is directly related to the spatial positioning of the turns, whereby those situated near the top are in closer proximity to the magnet's midplane, whereas those at the bottom are in closer proximity to the poles.

Additionally, the matrix features larger green squares surrounding the diagonal entries, which denote regions of elevated mutual inductance. These regions correspond to turns that belong to the same spatial group or block, where the coupling strength is higher. Conversely, the mutual coupling between different groups is observed to diminish as the distance between them increases. This pattern highlights the influence of spatial configuration and proximity on the inductive interactions, offering valuable insights into the collective behaviour of the turns and the overall impedance of the system.

The inductance matrix provides a comprehensive map that allows accurate predictions of impedance behavior in scenarios involving short circuits across different turns, making it a critical tool for understanding and simulating the system's response to such conditions.

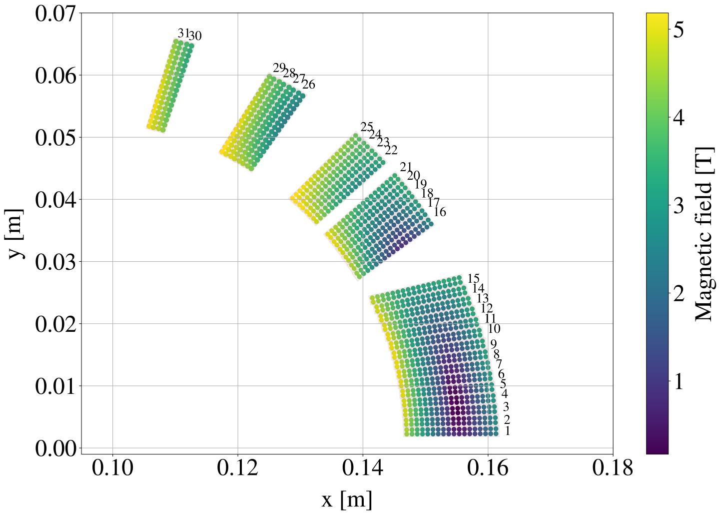

Figure 5.2: The field map shows the magnetic field configuration within the turns of an MBRD magnet coil, calculated using ROXIE [51], and the number of turns in the model.

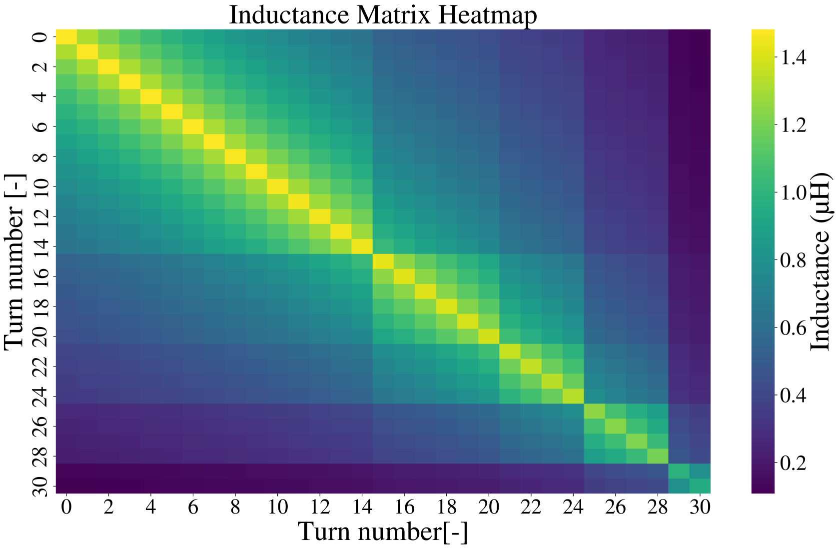

Figure 5.3: Plot of the inductance matrix of the coil turns for one pole. The diagonal represents the self-inductance of the turns, while the off-diagonal represents the mutual inductance between the turns. The numbering of the turns commences with the index 0, corresponding to turn 1, and concludes with index 30, corresponding to turn 31 of the configuration in Figure 5.2

5.1.1 Short circuits implementation in the TFM tool

In the TFM tool, the magnet circuit can be represented as a series of inductances, where each inductance may correspond to either a single turn or a group of turns in the coil. This modeling is achieved by assigning each turn to a specific section using the "turn_to_sections" key in the input YAML file, as illustrated in Figure 3.15. Moreover, the sections to be shorted and the resistance values for these shorts can be specified using the "sections_to_short" and "short_resistances" keys, respectively, in the same input file.

Figure 5.2 depicts a coil from the MBRD magnet, with each turn numbered sequentially from 1 to 31, progressing in a counterclockwise direction from the midplane to the pole. When each of these turns is assigned to a distinct section, the resulting network model consists of 31 inductances in series, each representing the contribution of the corresponding turn to the overall magnet inductance. The other pole can either be treated as a single section, as in the case presented, or it can be divided into multiple sections, depending on the purpose of the simulation.

By applying a resistance to individually short each section, one can analyze the impedance curve of the magnet resulting from these short circuits. This approach allows for the evaluation of the relative error by comparing the impedance with short circuits to the impedance in the reference configuration, where no short circuits are present. In Figure 5.4, the results for a resistance value of 0.01 Ω are presented. At low frequencies, where the short resistance is considerably higher than the inductance of the turn, the impedance with short circuits is observed to closely approximate the reference curve, with relative errors ranging from 0.001 % to 0.01 %. This is due to the fact that the current predominantly flows through the inductance. As the frequency increases, the relative error grows linearly. This increase is due to the linear increase of the inductance magnitude with frequency, resulting in a greater proportion of

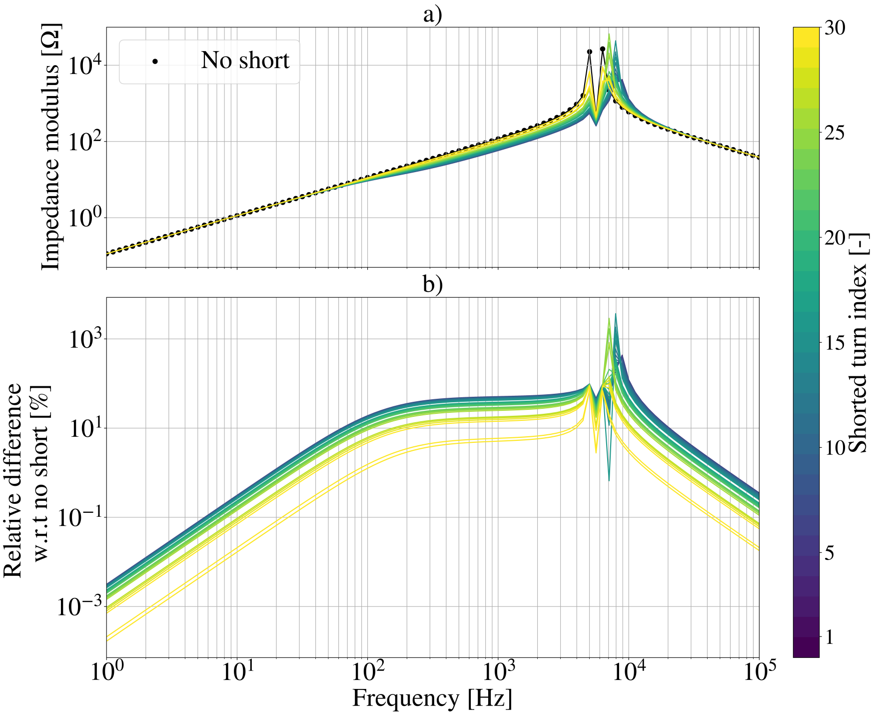

Figure 5.4: a) Impedance modulus for the MBRD magnet with a 1-aperture configuration. The black dotted curve represents the reference impedance without shorts, while the other curves show the impedance with a R_{Short}=0.01 Ω applied across different turns. b) Relative difference between the reference impedance and the impedance with short circuits. The color bar indicates the turn across which the short circuit was applied.

the current passing through the branch with the short resistance. This effect continues to amplify until the frequency reaches a point where the inductance value becomes larger than the resistance. At this stage, the phenomenon intensifies until the inductance exceeds the resistance, resulting in the majority of the current flowing through the short resistance branch and a relative error of approximately 500 %. Consequently, the losses incurred by the current flowing through the resistive branch reach a maximum at high frequencies, resulting in a significant alteration of the impedance.

Furthermore, the turns belonging to the initial sections of the coil results in a more pronounced alteration of the impedance curve when their respective inductance is shorted. This is due to the fact that, as illustrated in Figure 5.2, the turns in the initial section are situated in closer proximity to one another in comparison to those in the remaining sections. This results in a higher degree of mutual coupling between the adjacent turns. This coupling contributes more significantly to the overall inductance and causes greater disturbances when short circuits are applied [59].

5.2 Measurements Comparison

To further validate the TFM's operation and ensure its reliability in simulating non-conformities, an additional measurement validation was conducted. During the SM18 measurement campaign for the MBRD magnet, resistances were externally introduced at various voltage taps of the measurement system. In particular, two short circuits with nominal values of 0.8 Ω and 1.8 Ω were artificially introduced across two pole turns of one aperture. These turns correspond in this configuration of the network model to sections 30 and 31, corresponding to the two turns at the pole as illustrated in Figure 5.2. To reproduce the mentioned measurement, analogous resistances were imposed across the corresponding loops within the network model. The results of the comparison for the MBRD one-aperture magnet is presented in Figure 5.5, which depicts the relative error with and without shorts of the measured impedance, the simulated ideal impedance, and the simulation incorporating all coupling effects, for each resistance value.

In the case R_{Short} = 0.8 Ω, the measured relative error between the conditions with and without shorts, represented by dotted points, remains approximately 0 % up to 200 Hz. Beyond this frequency, the error demonstrates a negative trend, reaching a magnitude of -3 % before returning to zero. The simulated error without coupling effects at low frequencies displays a similar trend; however, instead of stabilizing at -3 %, it undergoes a significant decrease, consistent with the behavior depicted in Figure 5.4. The simulation incorporating coupling effects, represented by the solid black line Figure 5.5, demonstrates alignment with the measured data compared to the simulation without these effects. Nevertheless, the simulation still fails to fully capture the accuracy of the experimental measurements.

This discrepancy is attributed to the limitations of the network model, specifically the approximation of capacitance lumped and the challenge in capturing the reduced losses. Notwithstanding these limitations, the simulation incorporating all effects demonstrates a good alignment with the measured relative error up to 1 kHz. However, it deviates beyond this frequency due to a different peak magnitude. The capacity of the simulation to reproduce the peak in relative error at the same frequency as the measurement indicates that the short-circuit effect is identified correctly within the frequency range. Furthermore, when the

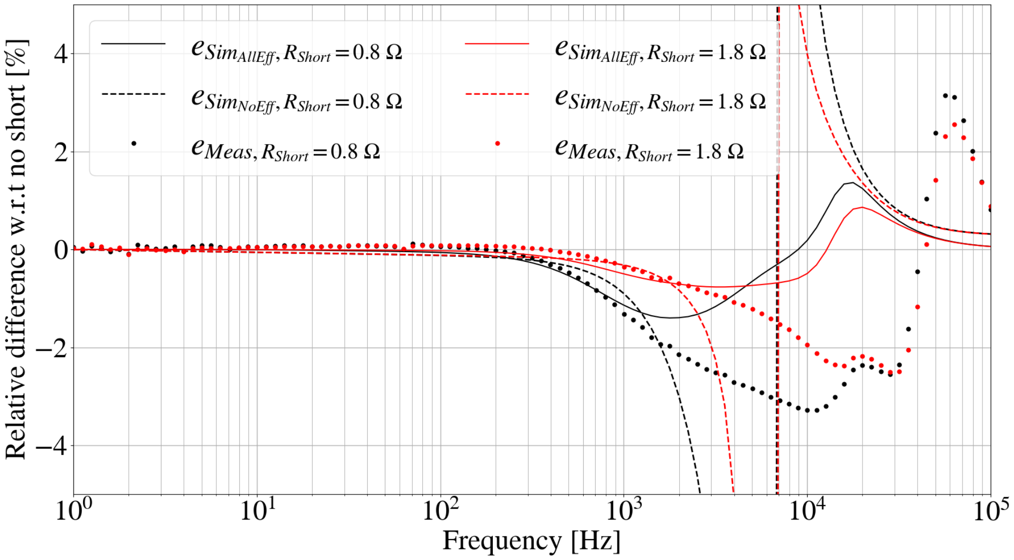

Figure 5.5: Relative difference in the impedance magnitude between measurements and simulations without and with a short circuit resistance across two specific turns of the magnet. The specified short resistances have been connected at warm across the voltage taps EE01-EE02 in Figure 2.7, corresponding to turns 30-31 in Figure 5.2 [64].

applied resistance is increased to 1.8 Ω, both simulated errors align with the response of the measurement data, thereby demonstrating the model's consistency in simulating impedance under varying resistance conditions.

5.3 Analysis of the Short Circuits Impact on the Simulated Impedance

Following the validation of the simulation against measurements from SM18, further analyses were conducted to assess the impact of short circuits under varying conditions on the magnet impedance. This was done with the aim of deepening the understanding of the complex effects associated with such occurrences.

An initial evaluation was conducted with a resistance of $R_{Short} = 0.01\ \Omega$ connected across different turns of the magnet coil, to see the impedance response to the same short-circuit generated in different locations. In Figure 5.6, the impedance deviation relative to the reference simulation depends on the group to which the turn belongs. The turns are divided into five blocks based on their location in the magnet coils, as illustrated in Figure 5.2. Turns 1-15 constitute the first block, 16-21 the second, 22-25 the third, 26-29 the fourth, and 30-31 the fifth. This division is reflected in the relative error in Figure 5.6, whose magnitude is influenced by the number of turns in each block. As the number of turns decreases progressively from block 1 to block 5, the mutual coupling between turns in blocks with more coils becomes stronger in the network model. This amplify the impact on the impedance when a short arises across one of these turns. Consequently, the relative error varies considerably, with an absolute value of 35 % for the initial turn situated in close proximity to the magnet midplane and a mere few percent for those situated in closer proximity to the pole. In comparison to

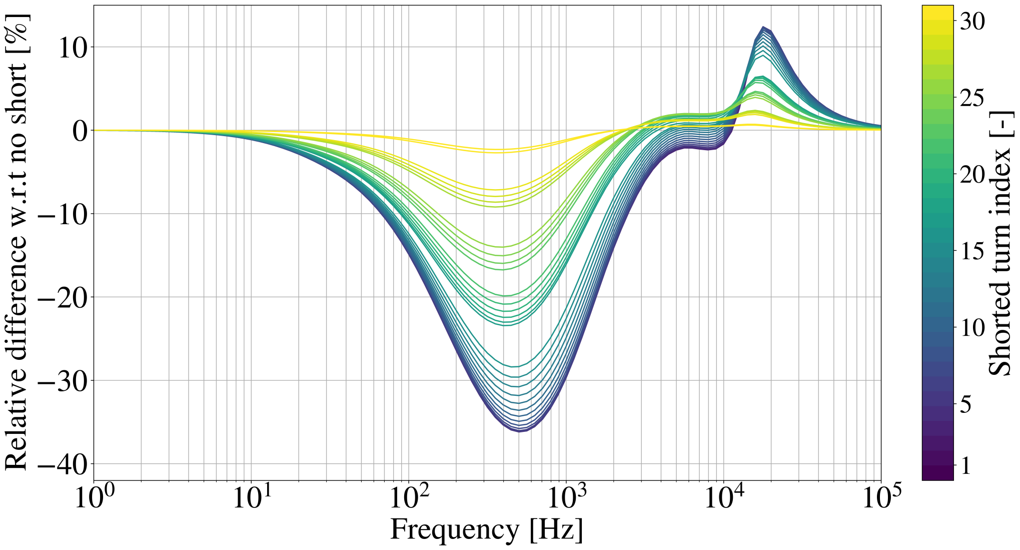

Figure 5.6: Relative error between the impedance simulation with and without the connection of a short circuit resistance of 0.01 Ω across the individual turns of the magnet. The color bar represents the number of the short-circuited turn, following the configuration displayed in Figure 5.2 [64].

the ideal impedance simulation, which excludes coupling losses, in Figure 5.4, the complete simulation provides a clearer distinction between the effects of different turns, thus enabling more precise identification of their respective positions within the magnet coil.

Further simulations were conducted to investigate the impact of varying resistance magnitudes, connected to the same magnet turn, on the impedance characteristics. As illustrated in Figure 5.7, for high resistance values, the relative error between the reference impedance simulation and the faulty simulation initially remains at 0 % for low frequencies. However, as the frequency increases, the relative error rises, reaches a maximum, and subsequently decreases. This behavior can be attributed to the fact that, at low frequencies, if the resistance is sufficiently high, the inductance of the turn is relatively small compared to the resistance, resulting in the majority of the current flowing through the inductance. As the frequency increases and the resistance becomes more significant, the current progressively shifts towards the resistance branch. At the peak frequency, the current flows predominantly through the resistance. Conversely, for low resistance values, the inductance is already greater than the resistance at low frequencies, leading to an immediate current flow through the resistance branch. At higher frequencies, variations in resistance induce a shift in the resonance peak. Additionally, the absolute value of the relative error varies between approximately 5 % and a few percent, inversely proportional to the short circuit resistance value. Specifically, as the short-circuit resistance decreases, the current flows for a greater duration through the resistance branch. This extended current flow results in increased losses, which in turn have a more pronounced effect on the deviation of the magnet's behavior from its ideal performance. Consequently, lower resistance values lead to higher relative errors due to the increased impact of these additional losses on the overall impedance characteristics of the magnet.

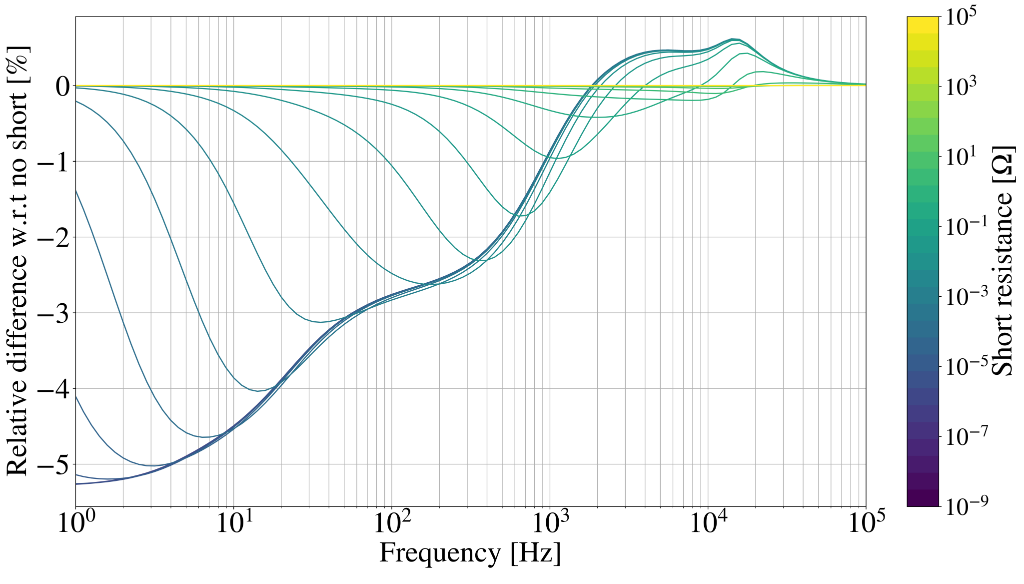

Figure 5.7: Relative error between the impedance simulation with and without the connection of a short circuit resistance across the same turn. The simulations have been performed for several resitance values between R_{Short} = 1 nΩ and R_{Short} = 0.1 MΩ [64].

Conclusions and Future Work

Superconducting magnets are fundamental elements of the Large Hadron Collider, serving to direct and concentrate the particle flux along its circular pathways. However, these magnets are subjected to notable operational risks, including those associated with quenching or rapid changes in the magnet excitation current. These conditions have the potential to cause localised heating and mechanical stress, which could result in damage to the insulation and, subsequently, the formation of short circuits in the coil windings. Such faults have the potential to damage the magnets' electromagnetic behavior, which could ultimately result in their failure. The current methods employed for the detection of faults in superconducting magnets are frequently inadequate, as they often prove unable to accurately identify short circuits or exhibit difficulty in detecting minor resistance fluctuations through resistive measurements. To improve fault detection, it is essential to develop a comprehensive approach that can precisely simulate the behavior of superconducting magnets under a wide range of operating conditions.

Such an approach requires the development of a robust model that takes into account all factors influencing the performance of the magnet. The model must be capable of replicating the magnet's behaviour under normal operating conditions in order to establish a reliable baseline or reference. By comparing the real-time data with the established reference, it becomes possible to identify any deviations that may indicate the early stages of potential failure. The ability to accurately predict and identify these precursors is crucial for maintaining the reliability and safety of the superconducting magnets in the LHC and preventing unexpected failures.

6.1 Summary of findings

This thesis addresses these challenges by developing a method for monitoring the behavior of superconducting magnets through complex impedance simulations in the frequency domain. The continuous measurement of the magnet's impedance provides invaluable insight into any anomalies that may occur during operation. In order to create a model that accurately reflects the true behavior of a superconducting magnet, a tool based on a physics-driven network utilizing lumped element modeling was developed. This tool incorporates fundamental elements such as coupling losses, interactions between coil turns and allows calculation of the impedance across the entire magnet or just specific turns of the coils.

To extend this approach to different magnets comprehensively, the tool was integrated into the STEAM framework, thereby enhancing its capability to include an equivalent lumped element network model. This computationally efficient model effectively reproduces the electrodynamic behaviour of superconducting magnets in both the time and frequency domains. By combining finite element modelling (FEM) using COMSOL Multiphysics® with analytical techniques, the approach successfully accounts for coupling losses and other factors that impact impedance characteristics.

In order to validate the developed tool, this thesis presents a detailed analysis using data from the MBRD magnet, which has been developed as part of the HL-LHC project and has recently undergone testing under a variety of conditions in the magnet test facility, SM18. The initial validation of the tool was conducted by simulating the magnet's behavior under standard operating conditions at 1.9 K. This step was of critical importance for verifying the accuracy of the tool's implementation and establishing a reference simulation against which further results could be compared.

Subsequently, the validation process was further expanded to include scenarios involving short circuits and to enable a comparison with the reference simulations. This extension effectively demonstrated the tool's capacity to accurately capture the intricate behavior of superconducting magnets in the presence of diverse fault conditions. Such comprehensive validation is crucial for confirming that the simulation tool can be relied upon to accurately predict and analyze magnet performance in a range of operational scenarios. Furthermore, the development of the tool has enhanced the comprehension of the complex impedance characteristics of superconducting magnets, through the mapping of the diverse contributions of coupling losses to the impedance curve. It was observed that conductor losses have a negligible effect on the curve, while metallic elements such as wedges, cold bores, the aluminum ring, and coil protection sheets contribute significantly. Notably, the largest contribution arises from domains where eddy currents can form the largest loops, which consequently result in greater losses. As observed with the eddy currents in the aluminium ring, both the size of a lossy element and whether it covers one or two apertures could also significantly impact the results.

In conclusion, the thesis provides an exhaustive examination of the impact of short circuits on the impedance curve of the magnet. This analysis provides valuable insights into the impact of short circuits, specifically how varying resistance values and their locations within the magnet influence its performance. The study thus establishes a foundational reference point for the detection and diagnosis of short circuits, including the identification of their location and magnitude. This comprehensive validation process guarantees that the tool is capable of accurately identifying and analysing potential issues, thereby ensuring the continuous and reliable operation of superconducting magnets in the LHC.

6.2 Model limitations

While the functionality of the tool has been demonstrated under a range of conditions, there are still some limitations that require further investigation. One significant area for further investigation is the capacitance modeling in the network model. Currently, the model simplifies capacitance by using only three discrete capacitance values: one at the beginning, one in the middle, and one at the end of the circuit. This simplification has an impact on the accuracy of the simulation, particularly at high frequencies and in scenarios involving short circuits. In order to achieve complete validation across the entire frequency range, it is necessary to reconsider and refine the capacitance modeling.

Furthermore, the comparison between simulation results and measurements involving externally connected short circuits needs to be more thoroughly explored. This will facilitate a more precise alignment between the simulated and measured data, thereby enhancing the reliability of the tool's predictions. An initial step should involve expanding this validation to include measurements at room temperature, where data on externally applied shorts tend to be more consistent and reliable. Following this, the focus can shift back to validating the model under superconducting conditions, informed by insights gained from the warm temperature results.

6.3 Outlook

A crucial next step in advancing the tool's development involves extending its validation to include comparisons with simulations conducted under warm conditions, such as those carried out at the SM18 facility. This supplementary validation is essential for a comprehensive evaluation of the tool's functionality and accuracy with regard to the MBRD magnet. Additionally, as mentioned above, the validation of the model at warm may facilitate a more precise comprehension of the influence of short circuits on the complex impedance characteristics.

However, the impact of this research extends beyond the MBRD magnet. The successful integration and validation of the TFM tool establishes a robust methodology that can be applied to other superconducting magnets within the LHC. This development significantly enhances the capacity to monitor, evaluate, and address potential performance issues, thereby contributing to the overall reliability and efficiency of the accelerator system.

In the future, the tool will be expanded to include all superconducting magnets with available data in the STEAM-SDK framework. It is, however, important to acknowledge that the current implementation is not fully automated. At present, COMSOL Multiphysics® simulations are necessary for each metallic component of every magnet in order to determine the equivalent parameters for the currents flowing through these components. This process is labour-intensive and could benefit from a more streamlined approach. The automation of these steps would significantly improve the tool's user-friendliness and accessibility. Given the complexity of COMSOL Multiphysics®, especially in the early stages of use, the incorporation of automation would greatly enhance the tool's practicality and efficiency for users, thereby making it a more effective resource for the management of superconducting magnet systems.

In conclusion, this thesis project has represented an advancement in the analysis of superconducting magnet performances by introducing a detailed, physics-based simulation tool that significantly enhances the capabilities of the STEAM framework. The tool, validated and designed to accurately model impedance while incorporating various non-ideal effects, enhances the effectiveness of monitoring and fault detection.

The developments achieved through this research are directly relevant not only to the LHC but also to the wider initiatives that are essential for the successful implementation of the LHC's high-luminosity upgrade. Furthermore, they are of great significance not only for the advancement of prospective projects in magnet technology but also for a multitude of applications across a diverse range of fields. The accurate and reliable performance

analysis of a given system is essential in a number of diverse areas, including sensors and biomedical applications, amongst others. By refining the validation process and enhancing the understanding of impedance characteristics, this approach can be adapted and applied to improve the performance and reliability of a wide array of technologies. The developed methodologies have the potential to significantly impact numerous sectors where precision and dependability in electromagnetic performance are critical.
Further research will concentrate on the refinement of the model and its application to additional magnets. This ongoing work is intended to facilitate a deeper comprehension of superconducting magnet systems and to enhance their management in particle accelerators, thereby supporting the continued progress and innovation in this field.

Bibliography

[1] CERN. *The Large Hadron Collider.* Accessed: 2024-07-08. 2024. URL: `https://home.cern/science/accelerators/large-hadron-collider`.

[2] Luca Bottura, Stephen A. Gourlay, Akira Yamamoto, and Alexander V. Zlobin. "Superconducting Magnets for Particle Accelerators". In: *IEEE Transactions on Nuclear Science* 63.2 (2016), pp. 751–776. DOI: `10.1109/TNS.2015.2485159`.

[3] Zayneb Trabelsi, Essia Hannachi, Sarah A. Alotaibi, Yassine Slimani, Munirah A. Almessiere, and Abdulhadi Baykal. "Superconductivity Phenomenon: Fundamentals and Theories". In: *Superconducting Materials: Fundamentals, Synthesis and Applications.* Ed. by Yassine Slimani and Essia Hannachi. Singapore: Springer Nature Singapore, 2022, pp. 1–27. ISBN: 978-981-19-1211-5. DOI: `10.1007/978-981-19-1211-5_1`. URL: `https://doi.org/10.1007/978-981-19-1211-5_1`.

[4] CERN Courier. *Safeguarding the superconducting magnets.* Accessed: 2024-07-09. 2013. URL: `https://cds.cern.ch/record/567209/files/7-4-as.pdf`.

[5] Herman ten Kate. *Superconducting Magnets Quench Propagation and Protection.* Accessed: 2024-07-09. 2013. URL: `https://indico.cern.ch/event/194284/contributions/1472819/attachments/281522/393603/TenKate_-_CAS_-Handout-Quench-Erice-2103.pdf`.

[6] A. Siemko. *Magnet Quench Process.* Accessed: 2024-06-24. URL: `https://cds.cern.ch/record/567209/files/7-4-as.pdf`.

[7] Emmanuele Ravaioli. "CLIQ. A new quench protection technology for superconducting magnets". presented 19 Jun 2015. PhD thesis. Twente U., Enschede, 2015. URL: `https://cds.cern.ch/record/2031159`.

[8] K.M. Smedley and R.E. Shafer. "Experimental determination of electrical characteristics and circuit models of superconducting dipole magnets". In: *IEEE Transactions on Magnetics* 30.5 (1994), pp. 2708–2712. DOI: `10.1109/20.312510`.

[9] CERN. *Cryogenics: Low temperatures, high performance.* Accessed: 2024-06-24. 2024. URL: `https://home.cern/science/engineering/cryogenics-low-temperatures-high-performance#:~:text=CERN%27s%20cryogenic%20systems%20cool%20over%201000%20magnets%20on,the%20production%20and%20effects%20of%20very%20low%20temperatures.`.

[10] M. Janitschke, M. Bednarek, E. Ravaioli, A.P. Verweij, G. Willering, and U. van Rienen. "Physics-driven lumped-element modelling for impedance simulations of superconducting accelerator magnets". To be published: ASC 2024.

[11] Piotr Artur Komorowski. "Electro-Topological Analysis and Diagnostics of the Superconducting Magnet Systems for the Large Hadron Collider". PhD thesis. Warsaw University of Thechnology, 2000.

[12] P. Komorowski and D. Tommasini. “Localization of electrical insulation failures in superconducting collared coils by analysis of the distortion of a pulsed magnetic field”. In: *IEEE Transactions on Applied Superconductivity* 10.1 (2000), pp. 166–169. DOI: `10.1109/77.828202`.

[13] L. Bortot, B. Auchmann, I. Cortes Garcia, A. M. Fernandez Navarro, M. Maciejewski, M. Mentink, M. Prioli, E. Ravaioli, S. Schps, and A. P. Verweij. “STEAM: A Hierarchical Cosimulation Framework for Superconducting Accelerator Magnet Circuits”. In: *IEEE Transactions on Applied Superconductivity* 28.3 (2018), pp. 1–6. DOI: `10.1109/TASC.2017.2787665`.

[14] Marvin Janitschke. “Framework for automatic superconducting magnet model generation & validation against transients measured in LHC magnets”. Presented 2022. MA thesis. Technische Universität Berlin, 2022. URL: `https://cds.cern.ch/record/2799810`.

[15] J Rosa L. nad Blackledge and A. Boretti. “ano-Magnetic Resonance Imaging (Nano-MRI) Gives Personalized Medicine a New Perspective”. In: *Biomedicines* (Feb. 2017). DOI: `10.3390/biomedicines5010007`.

[16] Santosh Miryala. “Prospects of Superconducting Magnet Technology in the Medical Field: A New Paradigm on the Horizon?” In: *Superconductivity: From Materials Science to Practical Applications.* Ed. by Paolo Mele, Kosmas Prassides, Chiara Tarantini, Anna Palau, Petre Badica, Alok K. Jha, and Tamio Endo. Cham: Springer International Publishing, 2020, pp. 353–360. ISBN: 978-3-030-23303-7. DOI: `10.1007/978-3-030-23303-7_13`. URL: `https://doi.org/10.1007/978-3-030-23303-7_13`.

[17] “Josephson Junctions and Their Properties”. In: *Superconductivity.* John Wiley and Sons, Ltd, 2016. Chap. 6, pp. 321–372. ISBN: 9783527686513. DOI: `https://doi.org/10.1002/9783527686513.ch6`. eprint: `https://onlinelibrary.wiley.com/doi/pdf/10.1002/9783527686513.ch6`. URL: `https://onlinelibrary.wiley.com/doi/abs/10.1002/9783527686513.ch6`.

[18] Anton Frisk Kockum and Franco Nori. “Quantum Bits with Josephson Junctions”. In: *Fundamentals and Frontiers of the Josephson Effect.* Ed. by Francesco Tafuri. Cham: Springer International Publishing, 2019, pp. 703–741. ISBN: 978-3-030-20726-7. DOI: `10.1007/978-3-030-20726-7_17`. URL: `https://doi.org/10.1007/978-3-030-20726-7_17`.

[19] P Ambhorkar, Z Wang, H Ko, S Lee, KI Koo, K Kim, and DD. Cho. “Nanowire-Based Biosensors: From Growth to Applications”. In: *Micromachines (Basel)* (2018). DOI: `10.3390/mi9120679`.

[20] R.G. Sharma. *Superconductivity Basics and Applications to Magnets.* 2nd ed. Vol. 214. Spinger Series in Materials Science, 2021. Chap. 3-8.

[21] Department of Engineering Professor Tomoaki Takao, Applied Sciences Faculty of Science, and Technology Sophia University. *Using zero electrical resistance from superconductivity research to give back to society.* Accessed: 2024-06-30. 2023. URL: `https://www.sophia.ac.jp/eng/article/feature/the-knot/the-knot-0114/#:`

~:text=Superconductivity%20is%20a%20phenomenon%20that,electrical%20resistance%20suddenly%20becomes%20zero..

[22] CryoMagnetics. *Basics of Superconducting Magnets.* Accessed: 2024-07-01. 2023. URL: https://cryomagnetics.com/wp-content/uploads/2022/05/Basics_of_Superconducting_Magnets.pdf.

[23] S Myers. *The engineering needed for particle physics.* Tech. rep. Geneva: CERN, 2011. URL: https://cds.cern.ch/record/1341526.

[24] Stephan Russenschuck. “Electromagnetic design of superconducting accelerator magnets”. In: (2004). DOI: 10.5170/CERN-2004-008.71. URL: https://cds.cern.ch/record/808348.

[25] Oliver Sim Brüning, Paul Collier, P Lebrun, Stephen Myers, Ranko Ostojic, John Poole, and Paul Proudlock. *LHC Design Report.* CERN Yellow Reports: Monographs. Geneva: CERN, 2004. DOI: 10.5170/CERN-2004-003-V-1. URL: https://cds.cern.ch/record/782076.

[26] G. Moritz. *Eddy currents (in acceleartor magnets).* June 2009. URL: https://cas.web.cern.ch/sites/default/files/lectures/bruges-2009/moritz-new.pdf.

[27] A P Verweij. “Electrodynamics of superconducting cables in accelerator magnets”. Presented on 15 Sep 1995. Twente U., Enschede, 1995. URL: https://cds.cern.ch/record/292595.

[28] E. Ravaioli, B. Auchmann, M. Maciejewski, H.H.J. ten Kate, and A.P. Verweij. “Lumped-Element Dynamic Electro-Thermal model of a superconducting magnet”. In: *Cryogenics* 80 (2016). Chats on Applied Superconductivity 2015 University of Bologna, Italy, 14-16 September 2015, pp. 346–356. ISSN: 0011-2275. DOI: https://doi.org/10.1016/j.cryogenics.2016.04.004. URL: https://www.sciencedirect.com/science/article/pii/S0011227516300832.

[29] Jacob Szeftel, Nicolas Sandeau, and Antoine Khater. “Comparative Study of the Meissner and Skin Effects in Superconductors”. In: *Progress In Electromagnetics Research M* 69 (June 2018). DOI: 10.2528/PIERM18012805.

[30] H Felice, S Prestemon, Ferracin P., and Todesco E. *Persistent currents and dynamic effects.* June 2009. URL: https://indico.cern.ch/event/440690/contributions/1089762/attachments/1143446/1638627/U18r.pdf.

[31] Stefania Farinon, Silvano Angius, Alberto Barutti, Andrea Bersani, Michela Bracco, Barbara Caiffi, Pasquale Fabbricatore, Lucio Fiscarelli, Arnaud Foussat, Andrea Gagno, Michael Guinchard, Filippo Levi, Franco Mangiarotti, Daniel Novelli, Alessandra Pampaloni, Nicola Sala, Ezio Todesco, Nicolò Valle, Alessio Verardo, and Gerard Willering. “The Development of MBRD Magnets, the Separation/Recombination Dipoles for the LHC High Luminosity Upgrade”. In: *IEEE Transactions on Applied Superconductivity* PP (Aug. 2024), pp. 1–5. DOI: 10.1109/TASC.2024.3357469.

[32] Daniel Novelli. “La protezione dal quench del dipolo superconduttore MBRD per l’upgrade ad alta luminosit‘a del Large Hadron Collider (HL-LHC)”. MA thesis. University of Genova, 2022.

[33] F. Levi, A. Bersani, B. Caiffi, R. Cereseto, P. Fabbricatore, S. Farinon, A. Foussat, F. Lonardo, A. Pampaloni, and E. Todesco. “The Separation-Recombination Dipole MBRD for the High-Luminosity LHC: From Prototype to Series”. In: *IEEE Transactions on Applied Superconductivity* 32.6 (2022), pp. 1–5. DOI: `10.1109/TASC.2022.3160975`.

[34] CERN. *High-Luminosity LHC FAQs*. Accessed: 2024-06-20. 2024. URL: `https://home.cern/resources/faqs/high-luminosity-lhc`.

[35] Z. Charifoulline. “Residual Resistivity Ratio (RRR) Measurements of LHC Superconducting NbTi Cable Strands”. In: *IEEE Transactions on Applied Superconductivity* 16.2 (2006), pp. 1188–1191. DOI: `10.1109/TASC.2006.873322`.

[36] S. Farinon, P. Fabbricatore, S. Curreli, and E. Todesco. “The Design of Superconducting Separation Dipoles D2 for the High Luminosity Upgrade of LHC”. In: *IEEE Transactions on Applied Superconductivity* 26.4 (2016), pp. 1–4. DOI: `10.1109/TASC.2016.2523060`.

[37] Pasquale Fabbricatore, Andrea Bersani, Barbara Caiffi, Roberto Cereseto, Stefania Farinon, Arnaud Foussat, and Ezio Todesco. “Development of a Short Model of the Superconducting Separation Dipoles D2 for the High Luminosity Upgrade of LHC”. In: *IEEE Transactions on Applied Superconductivity* 28.3 (2018), pp. 1–5. DOI: `10.1109/TASC.2017.2772779`.

[38] Andrea Bersani, Barbara Caiffi, Roberto Cereseto, Pasquale Fabbricatore, Stefania Farinon, Arnaud P. Foussat, Oussama Id Bahmane, Filippo Levi, Thomas Sahner, and Ezio Todesco. “The Superconducting Separation Dipoles MBRD for the High Luminosity Upgrade of LHC: From Short Model to Prototype”. In: *IEEE Transactions on Applied Superconductivity* 29.5 (2019), pp. 1–5. DOI: `10.1109/TASC.2019.2900598`.

[39] *STEAM-pySIGMA website*. `https://steam.docs.cern.ch/tools/sigma/`. Accessed: 2024-07-20.

[40] M. Maciejewski, C. Barbagallo, and B.U Bokhraie. *STEAM-SIGMA*. June 2019. URL: `https://pypi.org/project/steam-pysigma/`.

[41] Marta Bajko, Vladislav Benda, Luca Bottura, Alexandre Joel Broche, Fabio Formenti, Sebastiano Giannelli, Christian Giloux, Antoine Kosmicki, Consuelo Goncalves Perez, E. Perez-Duenas, Volker Mertens, Gijs De Rijk, Lucio Rossi, Nuno Dos Santos, Luigi Serio, Michal Strychalski, Hugues Thiesen, and Arnaud Vande Craen. “Upgrade of the CERN Superconducting Magnet Test Facility”. In: *IEEE Transactions on Applied Superconductivity* 27.4 (2017), pp. 1–7. DOI: `10.1109/TASC.2016.2635119`.

[42] M. Bednarek, R. Mompo, P. Jurkiewicz, A. Kotarba, J. Ludwin, and M. Talach. “Automatic Measurement System for Electrical Verification of the LHC Superconducting Circuits”. In: *Conf. Proc. C* 110904 (2011). Ed. by Christine Petit-Jean-Genaz, pp. 1756–1758.

[43] Michał Maciejewski, Emmanuele Ravaioli, Bernhard Auchmann, Arjan Verweij, and Andrzej Bartoszewicz. “Automated lumped-element simulation framework for modelling of transient effects in superconducting magnets”. In: *2015 20th International Conference on Methods and Models in Automation and Robotics (MMAR)*. 2015, pp. 840–845. DOI: `10.1109/MMAR.2015.7283986`.

[44] Anders Frem Wolstrup, Emmanuele Ravaioli, Tiberiu Gabriel Zsurzsan, and Zhe Zhang. “Automatic Frequency-Domain Modelling of Superconducting Magnets and its Usability to Model General Inductors”. In: *2021 IEEE 12th Energy Conversion Congress & Exposition - Asia (ECCE-Asia)*. 2021, pp. 1312–1318. DOI: `10.1109/ECCE-Asia49820.2021.9478990`.

[45] Michele Martino. “Low-Frequency Analytical Model of Superconducting Magnet Impedance”. In: *Modelling and Simulation in Engineering* 2022.1 (2022), p. 2105847. DOI: `https://doi.org/10.1155/2022/2105847`. eprint: `https://onlinelibrary.wiley.com/doi/pdf/10.1155/2022/2105847`. URL: `https://onlinelibrary.wiley.com/doi/abs/10.1155/2022/2105847`.

[46] R. Shafer. “Eddy currents, dispersion relations, and transient effects in superconducting magnets”. In: *IEEE Transactions on Magnetics* 17.1 (1981), pp. 722–725. DOI: `10.1109/TMAG.1981.1061171`.

[47] Sandia National Laboratories. *Xyce-Sandia website*. Accessed: 2024-08-27. URL: `https://xyce.sandia.gov/`.

[48] Alessandro Ilic Mezza, Riccardo Giampiccolo, and Alberto Bernardini. “Data-Driven Parameter Estimation of Lumped-Element Models via Automatic Differentiation”. In: *IEEE Access* 11 (2023), pp. 143601–143615. DOI: `10.1109/ACCESS.2023.3339890`.

[49] M. Janitschke, M. Bednarek, E. Ravaioli, A. Verweij, M. Wozniak, and U Van Rienen. *Local Transfer Function Measurements (TFM) in the LHC*. July 2024. URL: `https://indico.cern.ch/event/1414963/contributions/5946119/attachments/2890803/5067219/TE-MPE_GroupMeeting_Janitschke_04072024.pdf`.

[50] E. Ravaioli and M. Wozniak. *STEAM Simulation of Transient Effects in Accelerator superconducting Magnet circuits*. Sept. 2022. URL: `https://indico.cern.ch/event/1161448/attachments/2518602/4330455/2022.09.29%20-%20ER,MW%20-%20STEAM%20project.pdf`.

[51] Stephan Russenschuck. “ROXIE: A Computer Code for the Integrated Design of Accelerator Magnets”. In: (1998). URL: `https://cds.cern.ch/record/382851`.

[52] M. Janitschke, M. Bednarek, E. Ravaioli, A.P. Verweij, G. Willering, M. Wozniak, and U. van Rienen. “Validating the Physics-Driven Lumped-Element Model of the LHC Main Dipole Magnet”. In: *IEEE Transactions on Applied Superconductivity* 34.5 (2024), pp. 1–5. DOI: `10.1109/TASC.2024.3366876`.

[53] *STEAM-SDK website*. `https://steam.docs.cern.ch/tools/sdk/`. Accessed: 2024-07-20.

[54] *STEAM Materials library website*. `https://steam-material-library.docs.cern.ch/`. Accessed: 2024-07-20.

[55] M. Maciejewski, C. Barbagallo, and B.U Bokhraie. *STEAM-SIGMA*. June 2019. URL: `https://indico.cern.ch/event/817839/contributions/3414304/attachments/1856874/3057316/190605_STEAM-SIGMA.pdf`.

[56] National Institute of Nuclear Physics in Genova (INFN). *Detail Design of the Aluminum Sleeves for MBRD*. Tech. rep. 04. CERN, 2019. URL: `https://edms.cern.ch/ui/file/2137027/AC/lhcmbrdp0004-vAC.pdf`.

[57] National Institute of Nuclear Physics in Genova (INFN). *Design report of one aperture of the MBRD magnet*. Tech. rep. 04. CERN, 2019. URL: `https://edms.cern.ch/ui/file/2137021/0/lhcmbrdc0002-v0.pdf`.

[58] J. E. Kiwitt, A. Huber, and K Rei β. "Modellierung geblechter Eisenkerne durch homogene anisotrope Kerne fiJr dynamische Magnetfeldberechnungen". In: *Springer-Verlag Electrical Engineering* 81 (1999).

[59] M. Janitschke, E. Ravaioli, A.P. Verweij, G. Willering, and U. van Rienen. "Complex impedance of the LHC main dipole magnet in the presence of artificial short circuits". To be published: ASC 2024.

[60] H. Ehmler, H. Fillunger, Juergen Baldzuhn, R. Maix, A. Jeckle, S. Parodi, T. Rummel, K. Risse, and H. Scheller. "Comparative Analysis of Impulse and Impedance Tests to Detect Short Circuits Within the W7-X Magnets". In: *Applied Superconductivity, IEEE Transactions on* 16 (July 2006), pp. 767–770. DOI: `10.1109/TASC.2006.870539`.

[61] Konrad Riße, Th. Rummel, G. Ehrke, and M. Koppen. "Design, Tests, and Repair Procedures for the Electrical Insulation of the Superconducting W7-X Magnets". In: *IEEE Transactions on Applied Superconductivity* 20.3 (2010), pp. 447–450. DOI: `10.1109/TASC.2010.2044030`.

[62] H. Ehmler, I. R. Dixon, T. A. Painter, and J. A. Powell. "Electrical AC Tests on CICC Coil for Series-Connected Hybrid Magnet". In: *IEEE Transactions on Applied Superconductivity* 22.3 (2012), pp. 9002204–9002204. DOI: `10.1109/TASC.2011.2174955`.

[63] Arnaud Foussat, Ludovic Grand-Clement, David Smekens, Francois Olivier Pincot, Lorenzo Bortot, and Frederic Savary. "Frequency-Domain Diagnosis Methods for Quality Assessment of Nb3Sn Coil Insulation Systems and Impedance Measurement". In: *IEEE Transactions on Applied Superconductivity* 28.3 (2018), pp. 1–5. DOI: `10.1109/TASC.2017.2787748`.

[64] V. Reynaud, S. Farinon, M. Janitschke, E. Ravaioli, A.P. Verweij, G. Willering, and U. van Rienen. "Evaluating the electro-magnetic effects of electrical short-circuits in a Nb-Ti accelerator magnet". To be published: ASC 2024.